Phase Sensitive Interrogation of a RF Nanostrain Resonator for Structural Health Monitoring Sensing Applications

by

Rui Meng

A Thesis submitted to the Faculty of Graduate Studies of
The University of Manitoba
in partial fulfillment of the requirements for the degree of

Master of Science

Department of Electrical and Computer Engineering
University of Manitoba
Winnipeg, Manitoba
Canada

Author's Declaration

I hereby declare that I am the sole author of this thesis. This is not a finalized copy of my thesis. This is a nearly finalized draft of my thesis submitted to my examining committee for their consideration.

I understand that an electronic copy of the finalized draft of my thesis may be made electronically available to the public.

Abstract

The purpose of this study was to design a passive nanostrain Radio Frequency strain sensor that helps to monitor the strain changes caused by traffic in motion on bridges. The phase sensitive interrogation method was applied meaning that the strain changes will be measured by the cavity sensor phase shift. The results revealed that the RF strain sensor could achieve a resolution of a few nanostrain. The principle conclusion was that the designed RF strain sensor has nanostrain sensitivity. Coaxial-Cylinder sensor sensitivity was 8 nanostrain. Cylinder volume resonant cavity sensor sensitivity was 8 nanostrain for high Q and 4 nanostrain for low W. (BW = 160Hz) These sensitivities were somewhat larger than theoretical estimates due to noise from sauces other than the thermal noise used in the theoretical estimation. Therefore sensors will be useful for Structural Health Monitoring applications.

Acknowledgement

The author of this thesis would like to give his thanks to all those who altruistically devoted their time and subject expertise to aiding in the development of this thesis. I would like to extend my special thanks to my thesis supervisor, Dr. Douglas Thomson. His advice and patience was sensational through the entire thesis process and invaluable in my learning experience. I would also like to thank the University of Manitoba ECE technicians, Mr. Ken Biegun, Mr. Gordon Toole, Mr. Mount First and Mechanists Mr. Allen Symmons and Cory Smit and Civil structure lab technician Chad Klowak for their assistance and patience during the progression of this thesis. Mr. Dan Card, Dr. Greg Bridges, Mr. Allan McKay, also provided guidance in this thesis on numerous occasions which I greatly appreciated.

Table of Contents

List of Symbols

SHM – Structural Health Monitoring
LVDT – Linear Variable Differential Transducer
VW – Vibrating Wire
FOG – Fiber Optic Gyroscope
FBG – Fiber Bragg Grating
EMI – Electromagnetic Interference
POD – Optical Path Difference
PZT – Piezoelectric Tube
MZI – Mach Zehnder Interferometer
LIA – Lock-in Amplifier
RF – Radio Frequency
FFP – Fiber Fabry-Perot
LO – Local Oscillation
IF – Intermediate Frequency
PLL – Phase Lock Loop
PSD – Phase Sensitive Detector
VNA – Vector Network Analyzer
PPM – Part per Million i.e. microstrain
PPB – Part per Billion i.e. nanostrain
V_{out} – Mixer Output Voltage
P_{out} – Mixer Output Power
Z_{system} – System Impedance
V_{noise} – Thermal Noise Voltage
k – Boltzmann's Constant
T – Temperature
R – System Impedance
BW – System Bandwidth
TC – Time Constant
ε – Strain
f – Frequency
ϕ – Phase
C – Speed of Light
f_r – Resonant Frequency
ε_r – Relative Permittivity
L – Length of Cavity Sensor
Q – Quality Factor
V_{max} – Maximum Voltage

List of Figures

List of Tables

1. Chapter I Introduction

1.1 Structure Health Monitoring

"The process of implementing a damage identification strategy for aerospace, civil and mechanical engineering infrastructure is referred to as structural health monitoring (SHM)". [1] Damage is referred to as changes to the material and/or geometric properties of these systems. [1] For example, damage may include changes to the materials, changes to the boundary conditions and changes to system connectivity. In both cases, changes will adversely affect the system's performance. [1] SHM also includes the evaluation on infrastructure performance.

Almost all industries either private business or government owned agents need SHM. They need to detect damage in their products as well as in their manufacturing infrastructure at an early stage. Such detection requires these industries to perform some form of SHM. [1] This thesis has been motivated by the increased interest in SHM and its associated potential for significant safety and economic benefits.

"Most current structural and mechanical system maintenance is done in a time based mode." [1] This means a structure will be shut down during a set amount of time. SHM is the technology that applies the condition-based maintenance philosophies which are potentially more cost effective. "The concept of condition-based maintenance is that a sensing system on the structure will monitor the system response and notify the operator that damage has been

detected.” [1] However, this philosophy requires a more complicated monitoring hardware to be deployed on the system and it requires a sophisticated data analysis procedure to interrogate the measured data. [1] This is the trade off between SHM and the original maintenance methods.

1.2 Sensors for SHM

1.2.1 Sensor Types

Knowing that in-service structural health monitoring (SHM) of engineering structures plays a significant role in assessing their safety and integrity, we now take a look at some kinds of sensors used in the SHM sensing system.

Based on the measurands, sensors can be classified as acoustic; biological; chemical; electric; magnetic; mechanical; optical; radiation; thermal and other specified sensors. [2] Based on the application, sensors can be classified into automotive; civil construction; energy power; health, medicine; military, etc. [2] Here, we only focus on the civil construction application, especially for SHM.

The most common civil SHM sensors can be divided into four categories. Strain sensors, linear variable differential transducers (LVDT), accelerometers and temperature sensors. Here we only focus on the strain gauge. Foil gauge, vibrating wire gauges and fiber optic gauges are commonly used to measure strains in civil structural health monitoring applications. For measuring small strain values less than 100 microstrains, semiconductor strain gauges using piezoelectric devices are preferred. [3]

1.2.2 Strain Gauge Operation Principle

(a) Foil Strain Gauges

Among these types of strain sensors, the foil strain gauges are the most commonly used and typically the least expensive one. [3] The limitation of this type of sensor is that typically it can only achieve a resolution in a few micro-strains. Foil strain gauges measure the amount of strain applied to an object by monitoring the electrical resistance of the gauges. As shown in Figure 1.1, a foil strain gauge has a long and thin conductive strip in a zigzag pattern of parallel lines. The loops are made so that a small amount of strain in the direction of the orientation of the parallel lines results in a larger strain along the conductor's effective length, and hence a larger effect on resistance change. For most of the cases, foil strain gauges are attached to the surface of structural components such as girders or reinforcing bars. Gauges are wired to readout units for conversion to digital outputs. [3] When force has been applied that results in a strain to the components, the length at component surface changes and this will be transmitted to the strain gauge through the connecting materials. The strain causes the gauge to change in length and therefore change its resistance. If the gauge is lengthened its resistance will increase. After that, the corresponding signal is transmitted to the readout unit through the lead wires. [3]

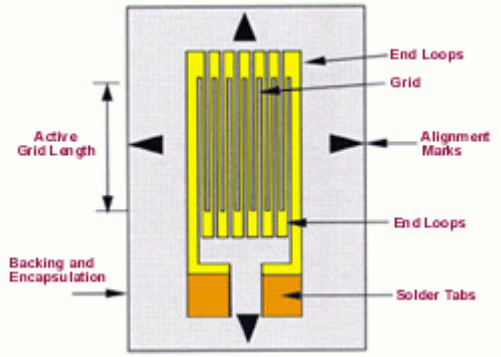

Figure 1.1 Foil Strain Gauge [4]

(b) Vibrating Wire Gauges

Vibrating wire (VW) strain sensors are usually bulky in size with a length of 100mm or larger. The resolution can be less than 1 micro-strains without using elaborate methods of gauge testing and selection. This type of strain sensor is also inexpensive and can be stable for a period more than 15 years. [17] VW sensors are produced for embedment in concrete or attaching to the surface of components. [3] Embeddable sensors can be placed into the concrete directly. Surface mounted sensors can be welded, bolted or bonded to the surface material. [3] As shown in Figure 1.2, the VW sensors are encased inside sealed steel tubes. The tensioned wire vibrates at a frequency that is proportional to the strain in the wire when it has been “plucked”. The sensor is installed so that a wire is held in tension between two ends of rebar. Applying load to the concrete structure will change the distance between the two rebar and result in a change in the tension of the wire. The wire can be plucked by an electromagnet which also measures the vibration frequency. Strain is then calculated by applying calibration factors to the frequency measurement.

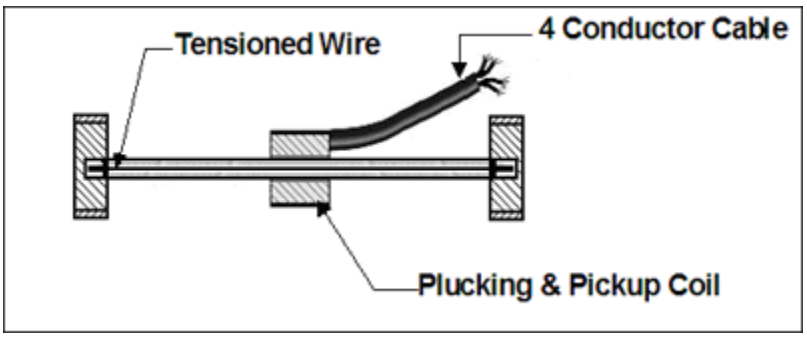

Figure 1.2 Vibrating Wire Strain Sensor [5]

(c) Fiber Optic Strain Gauges

It has been more than thirty years since researchers started to study fiber optic strain sensors. The most commonly used sensors in this field for strain measurement are fiber grating sensors and fiber optic interferometer. [6]

i. Fiber Bragg Gratings (FBG)

Among different types of fiber gratings, Fiber Bragg gratings (FBG) are most widely used as sensor heads. [6] FBGs are immune to electromagnetic interference (EMI) and ground loops. They have the advantage of being lightweight and small in physical size. They are suitable for being embedded into a new civil structure during the construction phase without any serious effect on the structural integrity. These sensors can also be attached onto existing structures. [7]

FBGs are produced by creating periodic variations in the refractive index of the core of an optical fiber. [7] Figure.1.3 shows the internal structure of an optical fiber with an FBG and the transmission and reflection spectra. When light is being passed through the grating, at the Bragg wavelength λ_B, the light reflected by the varying zones of refractive indices will be in phase and amplified.

[7] As shown in the “Transmitted spectrum”, under phase matching conditions, a FBG couples the forward propagating core mode to the backward propagating core mode. [6]

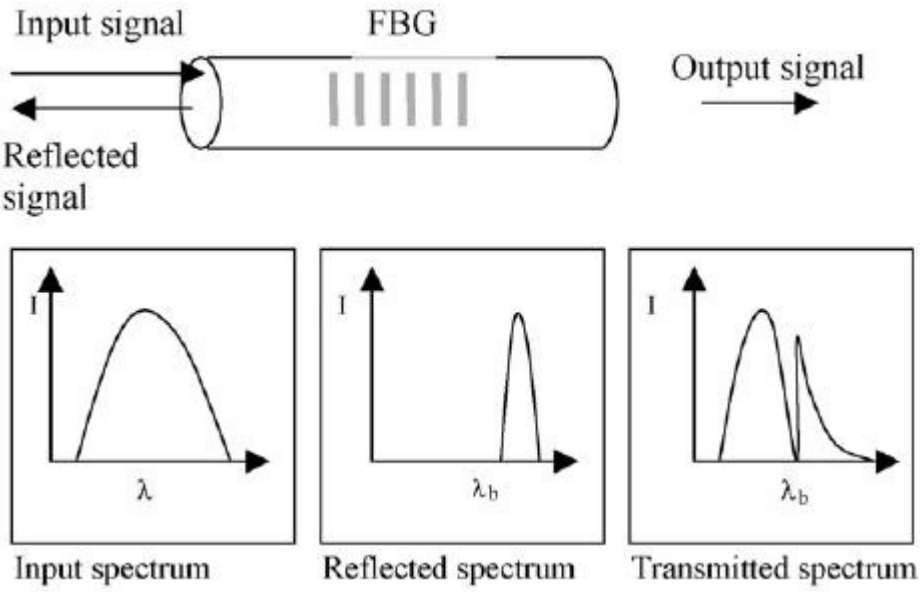

Figure 1.3 Transmission and Reflection Spectra for FBGs [7]

Strain applied longitudinally to the FBG is proportional to the relative change of Bragg Wavelength. [7] The strain can thus be obtained by measuring the wavelength of the reflected light.

To read the Bragg wavelength shift induced by strain changes, interrogators and demodulators are required. Optical spectrum analyzers are not used for this case because of the high cost and slow wavelength scanning speed. Several interrogation techniques have been proposed in the literature. [8] FBG interrogations can be generally classified as an active detection scheme and passive detection scheme. Table 1.1 shows examples of these two categories.

Table 1.1 FBG Interrogation Schemes [7]

Interrogation Type	Technologies
Passive Detection Scheme	Linearly wavelength-dependent device
	CCD spectrometer
	Power detection
	Identical chirped-grating pair
Active Detection Scheme	Fabry-perot filter
	Unbalanced Mach-Zehnder interferometer
	Fibre Fourier transform spectrometer
	Acoustic-optic tunable filter
	Matched FBG pair
	Michelson interferometer
	LPG pair interferometer

ii. Unbalanced Mach-Zehnder Interferometer Interrogation

Among all the interrogation schemes, it is the Unbalanced Mach-Zehnder interferometer technique that is similar to our design architecture. Figure1.4 shows the schematic of this method. The Pseudo-Hyterodyne method is used to analyze the phase variation. This method involves the application of optical path length modulation to one of the interferometer arms. In the figure, OPD stands for optical path difference. A piece of optical fiber is wound around the PZT, which stands for piezoelectric tube. The function generator generates a ramp signal. This signal is applied to the PZT and it expands the length of the tube and fiber

around the tube. Eventually, the optical path length of one interferometer arm can be altered by the ramp signal periodically. The amplitude of the ramp signal should be chosen properly to make the signals at photo detector P1 and P2 sinusoidal. The period of the detector signals are the same as the ramp signal period. The detector output goes through the band-pass filter at the modulation frequency. This will eliminate other frequency components such as the spikes caused by the discontinuities of the ramp signal.

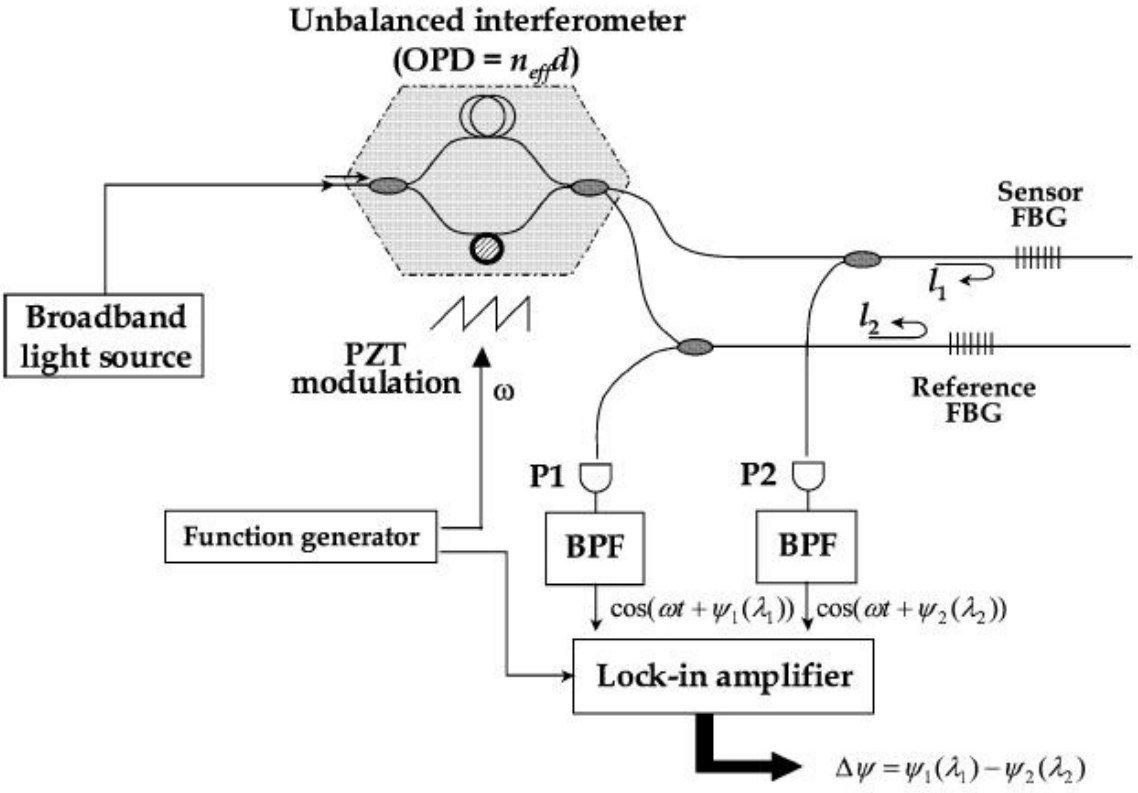

Figure 1.4 Unbalanced Mach Zehnder Interferometer Technique [6]

The unbalanced MZI interrogator also has a reference FBG as the other arm. The environmental factor such as temperature has an impact on the optical path difference. The interference signal is very sensitive to these changes. By adding in a reference FBG, the gratings in the sensor arm and the reference arm are experiencing the same amount of thermal drift. Therefore, the temperature effect can be cancelled by subtracting the reference signal out of the sensor grating signal.

The lock-in amplifier is used as a phase analyzer. The band-pass filtered signal and the ramp signal are used as the input and reference signal of the lock-in amplifier. The LIA can measure the change in wavelength in phase form.

By the small angle approximation, for a small phase θ, sin (θ) is approximately equal to θ. Therefore, the LIA input output relationship is approximately linear. The simplest way to implement the unbalanced MZI interrogator is to limit the input wavelength range to the linear portion of the sinusoidal output signal. The phase shift can be analyzed by observing the output signal. However, there is a tradeoff between the input wavelength range and the measurement resolution. Decreasing input wavelength will decrease the resolution.

iii. Fabry-Perot interrogation

The unbalanced MZI interrogation technique can result in a static resolution of several micro strains and a dynamic resolution of several nanostrains / √Hz. A good example is shown in [9]. High-resolution FBG strain sensors are commonly based on Fabry-Perot configuration. [10]

Figure1.5 shows the experimental setup of a Pound Drever Hall fiber Fabry–Pérot interrogation. The Laser generates the carrier which is passed through the optical isolator. Laser light is polarized vertically by the half wavelength plate. The Laser is then phase modulated by a modulator, which is driven by a Radio Frequency (RF) generator. The modulated laser light is coupled with an aspheric lens into a polarization independant optical circulator. The transmitted laser signal is then passed through the fiber Fabry-Perot (FFP). Next the light is passed through the isolator to eliminate parasitic etalon effect of the residual back reflections from the lens. The light is focused by the length and picked up by a photo detector Tx.

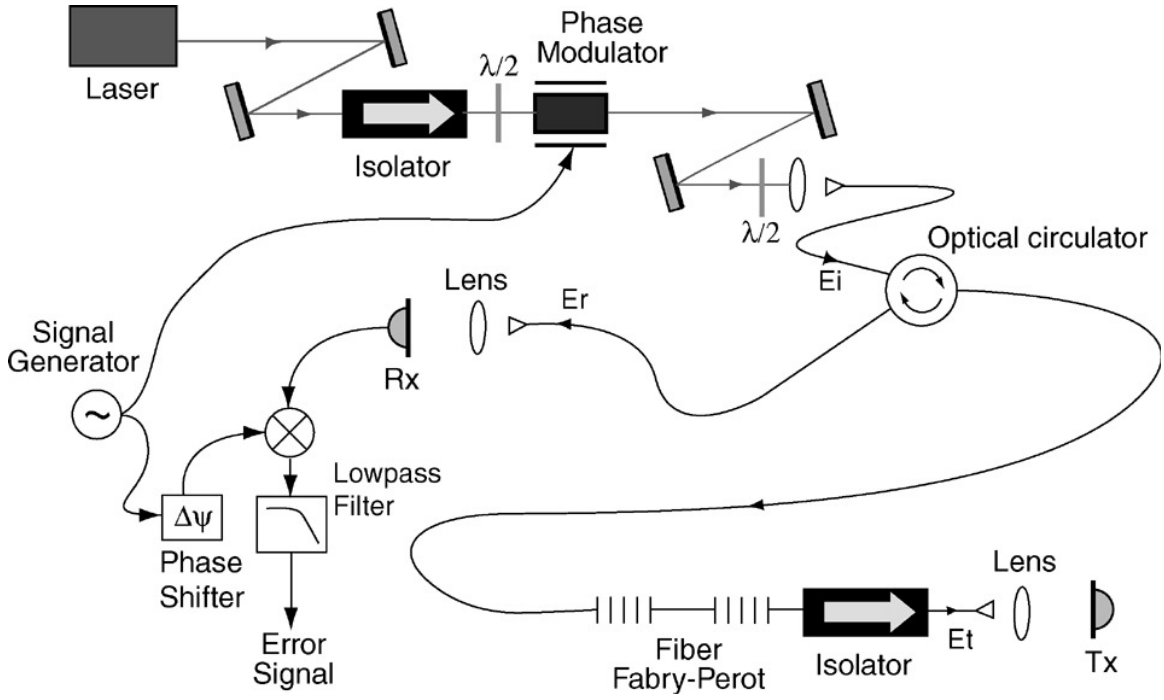

Figure 1.5 Experimental Setup of a Pound Drever Hall Fiber Fabry–Pérot Interrogation [11]

The optical circulator is a three port component. Besides the transmitted light, there is a second light signal which is reflected to a lens and picked up by a photo detector Rx. This light signal goes through a demodulation process. The RF signal generator is used as a local oscillator. The generated RF signal passes through a phase shifter to get the same phase as the signal detected by Rx. The two signals are passed to a mixer then a lowpass filter to generate the error signal. This error signal is then sent back to the laser source creating a feedback loop to lock the laser frequency to the FFP cavity resonance.

The FFP cavity is controlled by a PZT. If strain is applied to the FFP, the FFP cavity will change its length and hence changing the Bragg wavelength and the resonant frequency. 1 pm wavelength shift is equal to a strain change of 0.8 microstrains. [11] Since 1 pm is equal to 125 MHz at the Bragg wavelength of 1550 nm, the FFP sensor has a strain sensitivity that can be calculated to be approximately 2 picostrain / √Hz. [11] [12]

iv. Comments

Fiber Optical sensors have the advantages of being lightweight, small in physical dimension, immune to EMI and ground loop, high sensitivity and dynamic range, etc. However, they still have some drawbacks in real world application of SHM. One explanation of Fiber optical sensors not reaching their maximum market potential is that there have been no standards associated with these sensors so far. Standards for sensor packaging and usage in SHM have not yet been arrived by any organizations and institutions. [7] Another disadvantage of fiber optical sensors is the fact that these sensors required

complicated interrogation systems which are very expensive at present. [7] In addition, some remaining issues associated with fiber optical sensors need to be considered. Temperature changes will cause a wavelength shift which has to be compensated, comprising the sensors resolution. The fiber optical sensors are brittle, for all practical situations, it is better to encapsulate the bare FBG sensors before mounting them on any structure. However, the protective layer and the adhesive layer absorb a part of the strain and the indication given by the FBG is not the true strain on the structure. [7] One study concludes that for better strain transfer from the host material to the FBG sensors, a thin layer of adhesive, a high modulus coating material and a sufficient embedding length of the sensor is necessary. [13] This further complicates the use of fiber optic sensor.

(d) Piezoelectric Strain Sensors

The way that piezoresistive strain sensors work is that by applying strain to the sensors, there will be a electrical resistance change on the device and the corresponding strain can be measured. Carbon nantotubes can be used to form piezoresitive strain sensors for SHM applications. In [14], Inpil Kang et al show that a carbon nanotube piezoresistive strain sensor can achieve a sensitivity of several hundred microstrains.

Semiconductors such as ZnO can be used to make piezoelectric fine wires which can form a piezoelectric strain sensor. [15]

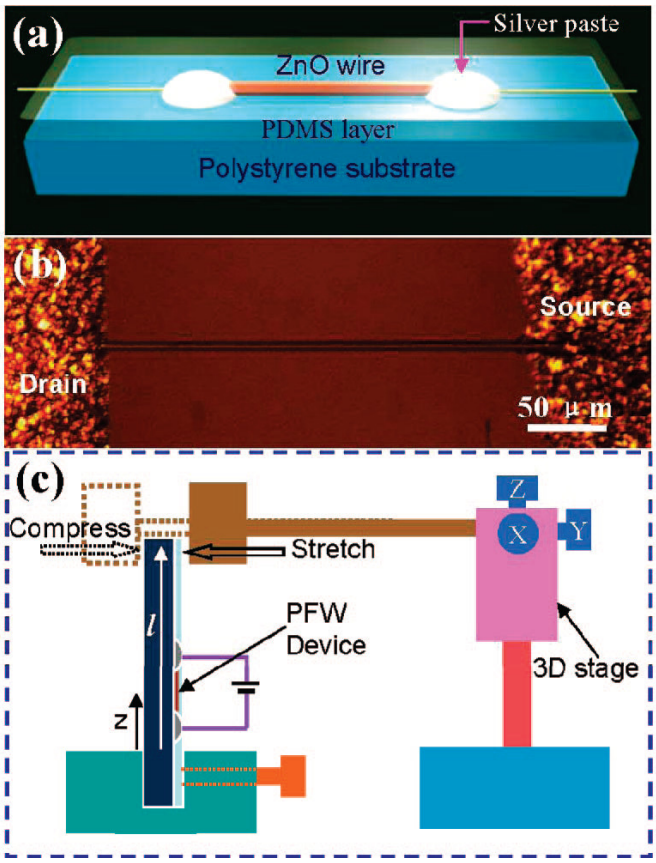

Figure 1.6 (a) Schematic of a single ZnO PFW based strain sensor device (b) Optical image of a strain sensor device (c) Schematic of the measurement system to characterize the performance of the sensor device [15]

1.3 Radio Frequency Strain Sensors

In this thesis, I will focus on designing a resonant radio frequency (RF) strain sensors for use in SHM applications. The motivation is to design a strain sensor that has nanostrain resolution and easy interrogation system. The nanostrain resolution is necessary so that the sensor can be used to measure dynamic strain changes by small vehicles. It may also be used to identify the vehicle type as well. The sensor I designed is a wired passive device that can be attached to

or embedded into a civil structure component. An electronic interrogation system is also presented. The sensor I used is a conducting coaxial electromagnetic cavity with resonant frequency of approximately 2.4 GHz. The sensor is attached to or embedded to a structure where the strain is applied and measured.

When strain is applied, the length of the cavity will change which results in a shift of the resonant frequency. The frequency change can be seen as the phase variation which can be monitored using the interrogation technique. The detailed explanation of the interrogation system will be discussed in the next chapter. The RF strain sensor has a resolution in the nanostrain range which should prove useful for measuring strains for SHM applications. The detailed explanation of how to achieve the nanostrain resolution is also discussed in the next chapter.

1.4 Comparison to State of the Art

a) Summary

The RF strain sensor is unique compared with all the sensors we overviewed above. The metal foil strain gauge and the vibrating wire strain gauge are commonly used for SHM applications because of the low cost and easy installation. However, their resolution is only a micro-strain, much poorer compared with nanostrain sensitivity of our RF strain sensor. The piezoelectric sensors have better signal to noise ratio when measuring strains less than 150 microstrain. They have a resolution as low as several microstrain which is poorer than the RF strain sensor.

Fiber optical strain sensors are comparable with our RF strain sensors in that they have a resolution in sub-picostrain range. They are also widely used for

SHM applications. The drawback of these sensors is that they require a complicated interrogation system which is very expensive. Moreover, these sensors use lasers as the signal source which will result in some noise in measurement such as the free running frequency noise. These sensors are affected by the ambient temperature variation. A temperature change will have an impact on the strain measurement. Fiber optic sensors undergo fiber fatigue which is another factor limiting their application.

b) Summary Table

Table 1.2 Summary Table for various Strain Sensor Technologies

Sensor Type	Achievements	Limitation
Foil Strain Gauge	inexpensive, widely used in SHM, easy installation	resolution of a few microstrain
Vibrating Wire	inexpensive, easy installation, excellent durability, stable for more than 15 years	resolution of a few microstrain
Piezoelectric	less signal conditioning required, good for applications with low strain level and high noise level	resolution of a few microstrain, no good for strain level more than 150 microstrain since nonlinearity and changes in material property [18]

Fiber Optic	resolution of subpico/nanostrain, high signal to noise ratio	complicated interrogation system, fiber fatigue, expensive
RF Strain Sensor	resolution of a few nanostrain, high signal to noise ratio, easy interrogation system,	thermal noise from the electronic parts

2. Chapter II Apparatus

2.1 Block Diagram

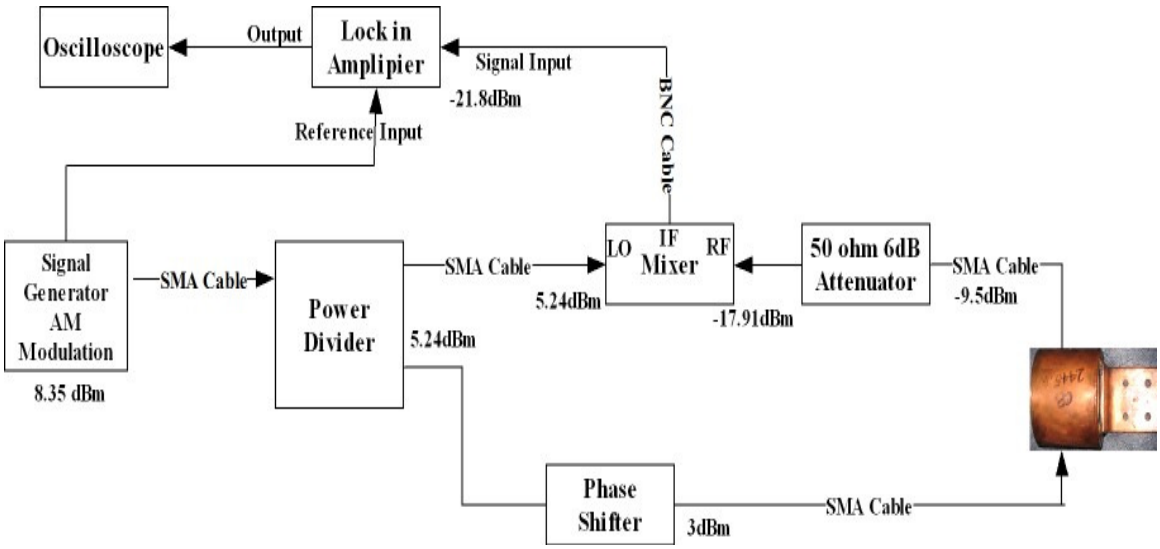

Figure 2.1 Block Diagram of the Phase Sensitive RF Nanostrain Resonator System

The system block diagram is shown in figure 2.1. In the system, I use a signal generator to produce RF signals. The Power level of the signal generator is typically set to be 9dBm. The RF signal goes into power divider that splits the signal evenly into two signal paths. One signal is the reference path that goes into the Local Oscillation (LO) port of the mixer. The other signal goes into an adjustable phase shifter and then to a cavity resonator and a 50 ohm 6dB attenuator and finally goes into the Radio Frequency (RF) port of the mixer. The Intermediate Frequency (IF) port of the mixer outputs a signal and the signal goes through a BNC cable to the Lock-in Amplifier. The signal coming out of the

LIA is monitored by a sampling oscilloscope. The individual parts mentioned here will be discussed in more detail in the following sections.

2.2 Function Generator

Figure 2.2 Block Diagram of the Phase Sensitive RF Nanostrain Resonator System

Figure 2.2 shows the picture of the function generator I used in our system. The signal generator shown here is the Rohde & Schwarz SMT 03 that has a frequency range from 5 KHz to 3 GHz.

I used the AM modulation to reduce the effect of electronic noise and chose the carrier frequency from 15 KHz to 50 KHz. The signal was sinusoidal.

The signal generator can supply power from -144dBm to 16dBm. In this design, I chose 9dBm as the power output to match the requirements of the mixer. This is to obtain the maximum signal without distortion. The signal supplied by the signal generator goes into a power divider via SMA cable.

2.3 Power Divider

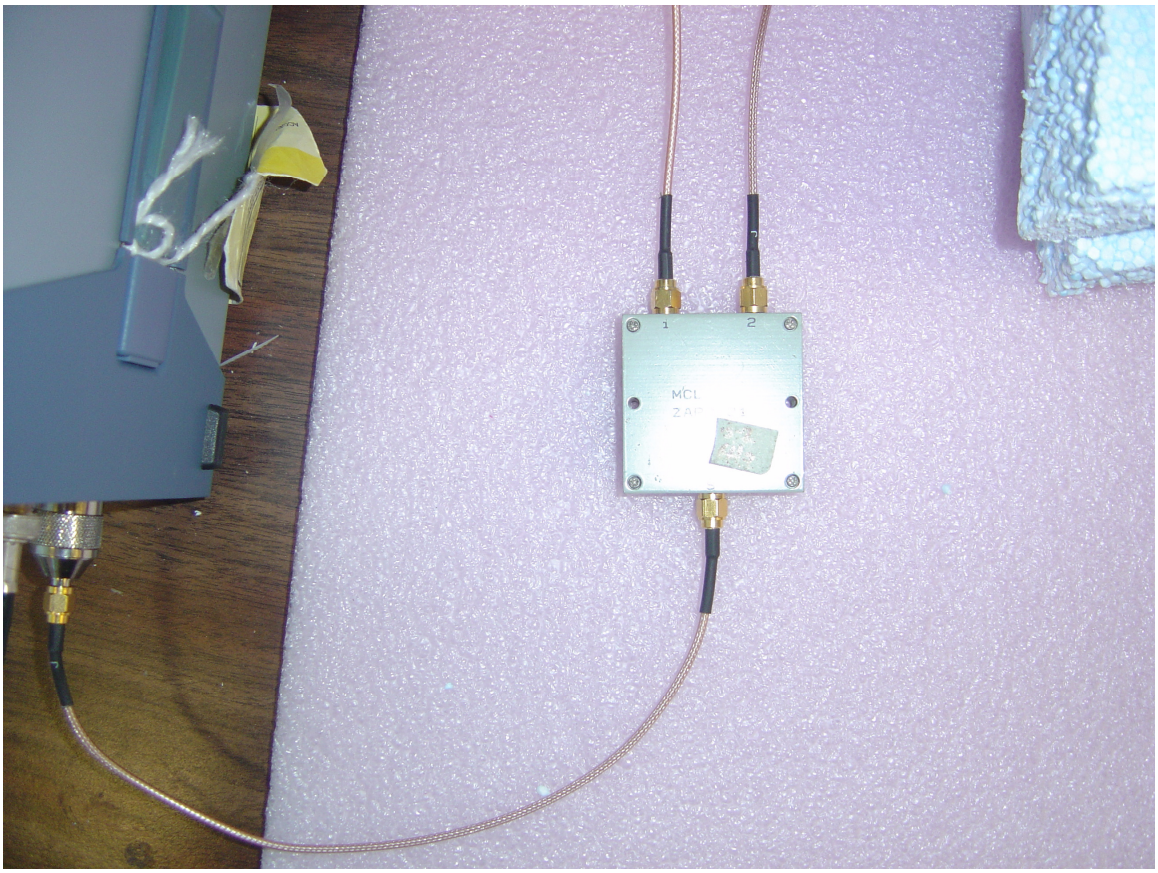

Figure 2.3 Power Divider

The power divider shown here is the MCL ZAPD-21. It is a power divider that splits the RF signal power evenly into to two paths. I have already mentioned that the RF signal has a power level of 9dBm, so the matched power rating of the power divider has to be greater than 9dBm. The divider has an insertion loss of approximately 1dB. Therefore, the signals coming out of the divider will be around 5dBm each.

2.4 Phase Shifter

Figure 2.4 Phase Shifter

The phase shifter shown here is P1213 from the Advanced Technical Material (ATM) Inc. It has the maximum insertion loss of 0.6 dB. The minimum phase adjust is 180˚ / GHz.

The purpose of inserting this phase shifter is to allow the phase in the path to be adjusted to produce a null output from the mixer. The sensing path will include a cavity resonator, an attenuator and of course the phase shifter. All these elements will cause a phase shift relative to the reference path even though there is no strain applied to the cavity sensor. I can compensate for this by inserting a phase shifter which is shown above. I can adjust the phase shift of the path to zero the output from the mixer, in other words, to null it out. The signal coming out of the phase shifter will go into a cavity resonator via an SMA Cable.

2.5 Attenuator

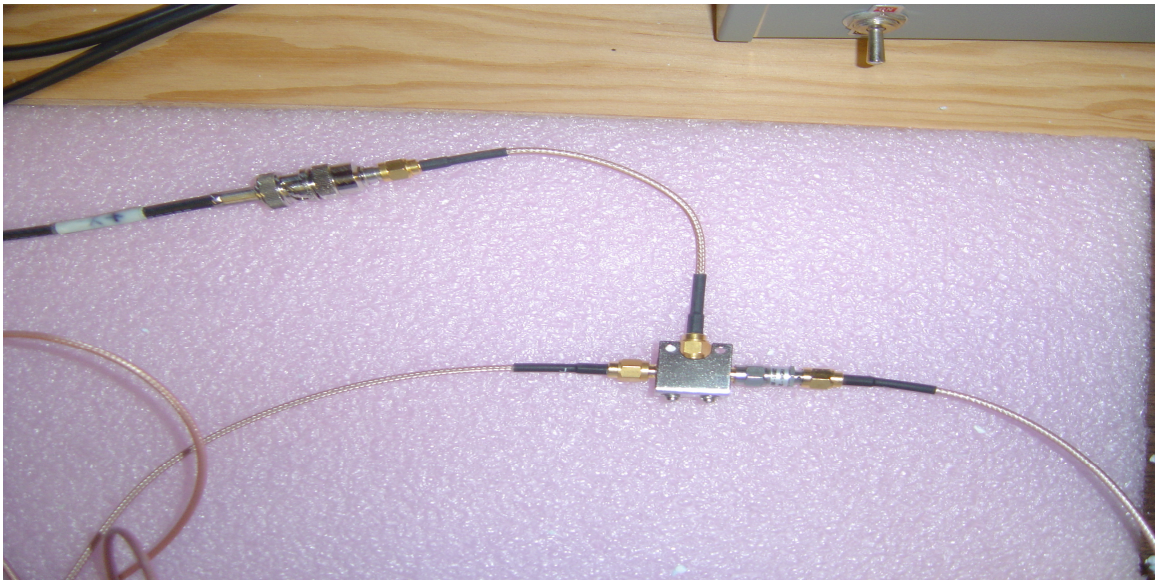

Figure 2.5 Mixer and Attenuator

Figure 2.5 shows the mixer and the attenuator in the design system. The attenuator used here is Mini Circuit precision fixed attenuator of model BW-S6W2. It has attenuation of 6dB and impedance of 50 ohms. It can output a maximum power of 2W. The data sheet is attached in the Appendix.

As mentioned in the previous section, to obtain maximum signal without distortion, I chose the RF supply from the signal generator to be 9dBm. This signal goes through a path with some losses and finally goes into the RF port of the mixer. The mixer has a maximum power input level. To maintain the signal input well below the 1dB compression point, an attenuator is inserted to adjust the power level.

2.6 Frequency Mixer

The frequency mixer used in the design system is shown in Figure 2.5 along with the attenuator. It is Mini Circuit model number ZX05-C24. The mixer is specified as Level 7, i.e. LO port requires a drive power of 7dBm. It has frequency range from 300MHz to 2.4GHz. The 1dB compression point is 1dBm. The conversion loss is 7dB. The detailed specifications can be found in the datasheet attached to the Appendix.

It has already been mentioned in the previous section that the power divider splits the RF signal into two paths. One of the two is the reference path that goes directly to the LO port of the mixer. The other path includes a phase shifter, a

cavity sensor and a 50 ohm 6dB attenuator and the signal goes into the RF port of the mixer. The frequency mixer will mix the signals coming from the two paths. The IF port of the frequency mixer generates an output that gives the difference between the two signals coming from the LO and RF ports. It is shown in the diagram below. The signal coming out of the mixer will go to a Lock-in Amplifier.

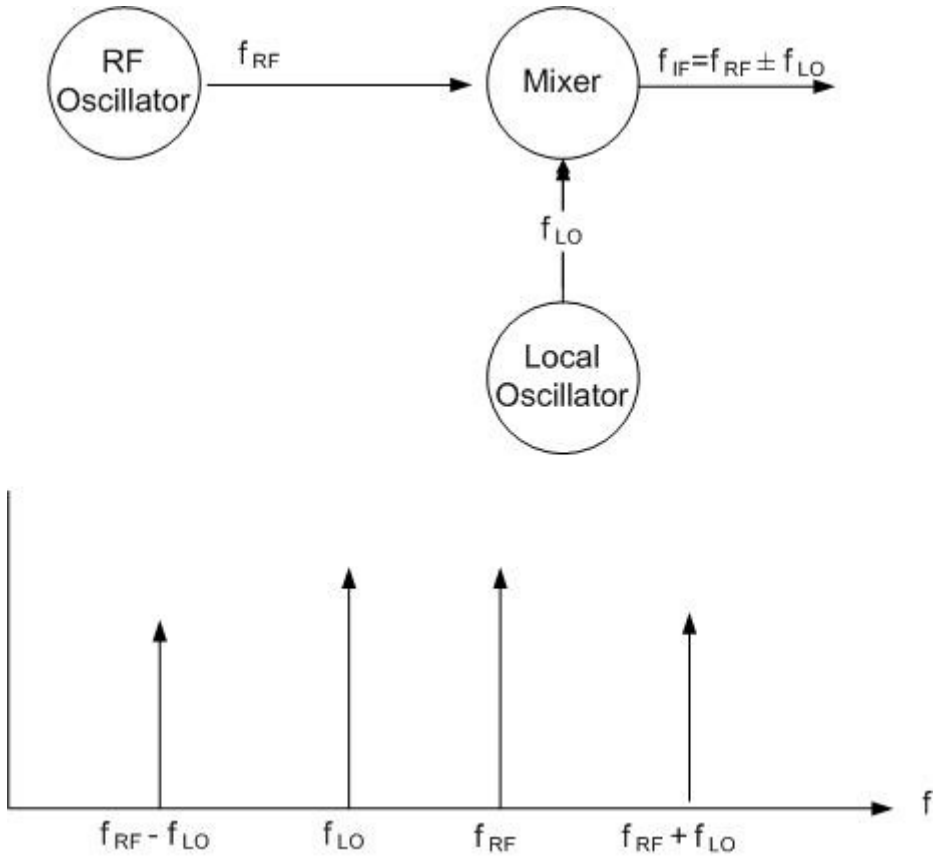

Figure 2.6 Frequency Mixer Down Conversion Diagram

2.7 Lock-in Amplifier

SR510 Lock-In Amplifier

Figure 2.7 Lock-in Amplifier [20]

Figure 2.7 shows the picture of the lock-in amplifier. The lock-in amplifier used here in the system is SR510 analog LIA from Stanford Research System.

In the design, I adjusted two parameters of the lock-in amplifier, i.e. the sensitivity and the time constant. The time constant defines the bandwidth of the system. For example, when I set the time constant to be 1ms, then the bandwidth will be $1/(2\pi \bullet \text{Time constant}) = 1/(2\pi x 1 x 10^{-3}) \approx 160$ Hz.

The lock-in amplifier requires a frequency reference. It uses a Phase Locked Loop (PLL) to generate the reference signal. The signal generator provides an external reference signal to the lock-in amplifier. The PLL in the lock-in amplifier locks its internal oscillator to the external reference signal.

The signal coming out of the frequency mixer goes into the lock-in amplifier as its input signal. The lock-in amplifier amplifies the input signal and then multiplies it by the reference signal performing a phase-sensitive detector. The output of the PSD is simply the product of two sinusoidal waves. The results are

two AC signals. One is the sum of the two frequencies, and one is the difference of the two frequencies. The two AC signals go through a low pass filter and only the signal showing the frequency difference will pass through the filter and become the output of the lock-in amplifier. The output signal is then going to a digital storage oscilloscope.

2.8 Oscilloscope

Figure 2.8 shows the digital storage oscilloscope from Agilent Technologies. The model number is DS05012A. It has two channels and a USB port to store digital data. Its bandwidth is 100MHz and the data sample rate is 2GSa / S. The detailed datasheet is attached to the Appendix.

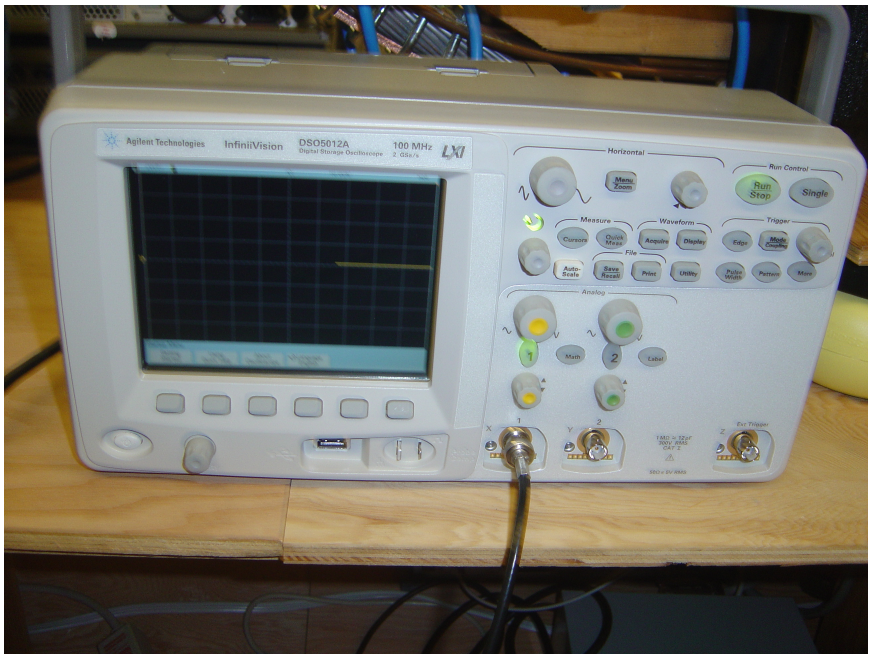

Figure 2.8 Digital Storage Oscilloscope

I chose 1M Ohm as the input impedance to avoid input the current signal becoming saturated. I chose the roll mode in the scope to observe the signal

coming out of the lock-in amplifier. In this mode the oscilloscope behaves like a strip chart recorder. I set up the system to be 50 seconds per division and I observe the signal for 8 divisions 400 seconds. By simply hitting the stop button, the signal showing on the scope screen will freeze and I can store these data to a USB stick. The scope data can be later on opened by Microsoft Excel.

2.9 Sensor

I used two types of sensors in our design, i.e. the diaphragm sensor and the cylindrical cavity sensor. The diagrams, pictures and drawings of the two types of sensors are shown in the following sections.

a) Diaphragm Sensor

Figure 2.9 Diaphragm Sensor Picture

Figure 2.9 shows the diaphragm sensor picture. The sensor is made of copper and is conductive. It has two SMA connectors soldered on each side of its body. It is hollow inside which makes it a cavity. One end of the cavity has a

diaphragm as the cover. The diaphragm has a knob in the middle to connect one end of a rod to measure strain. The other end of the cavity is made of solid copper and has been attached with a copper bracket for mounting purposes. The detailed dimensions and inside cross sections are shown in the following diagrams and drawings.

Figure 2.10 shows the diaphragm sensor diagram. It shows all the details about the sensor cavity including the dimension.

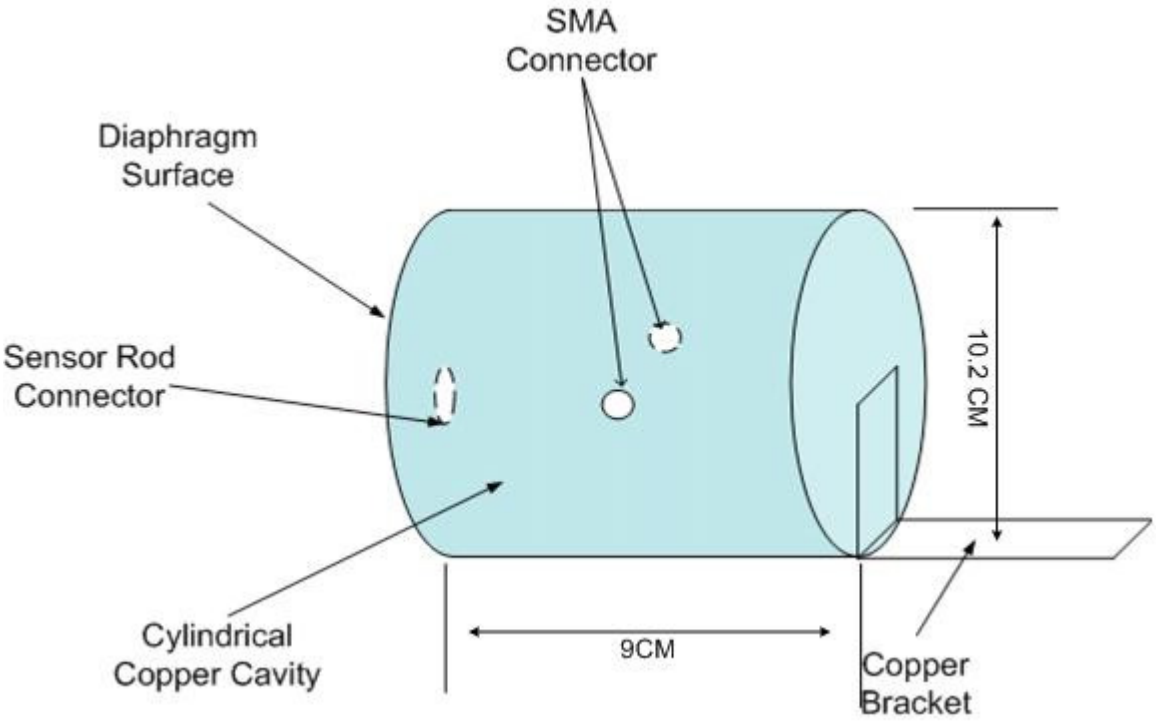

Figure 2.10 Diaphragm Sensor Diagram

b) Cylinder Sensor

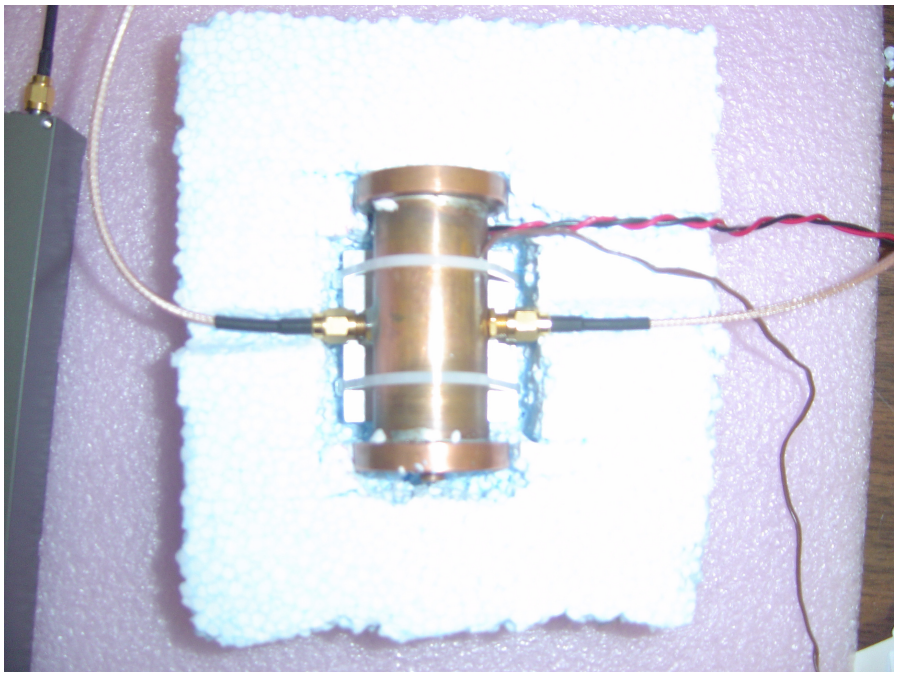

Figure 2.11 Cylinder Sensor Picture

Figure 2.11 shows the picture of the cylinder sensor. This sensor is also made of copper and it is conductive. The body of the sensor is a cylindrical cavity. Two SMA connectors are soldered onto each side of the cavity. The detailed dimension and cross section drawings are shown below.

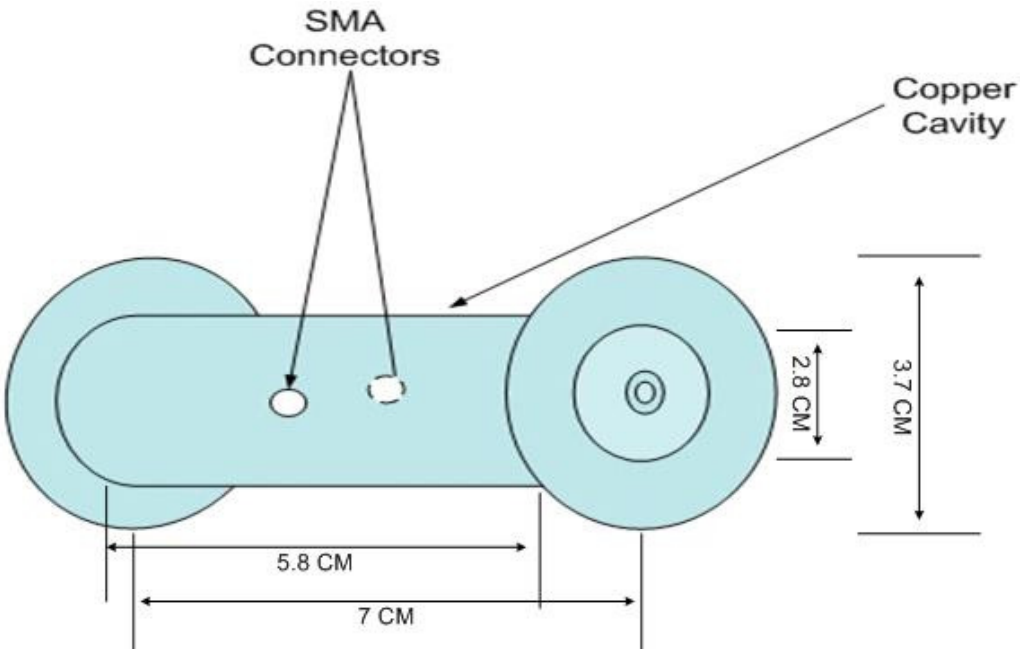

Figure 2.12 Cylinder Sensor Diagram

Figure 2.12 is the cylinder sensor diagram which shows the all the details about the sensor.

2.10 Signals at Various Points

Table 2.1 Summary of Signals at various points (Circuit Diagram refer to Figure 2.1)

	RF supply	Signal going into Mixer LO	Signal going into Mixer RF
Cylinder Sensor	8.33dBm	4.77dBm	-7.18dBm
Diaphragm Sensor Low Q	8.33dBm	5.05dBm	-9.52dBm
Diaphragm sensor High Q	8.35dBm	5.24dBm	-17.91dBm

Shown in Table 2.1 are the signal power levels at various points. These data were recorded by a Broadband RF power meter that can measure power level ranging from -70dBm to +44dBm. Signal power levels will be discussed into details in the next chapter.

3. Chapter III Theoretical Calculation of Noise

In this chapter, I will estimate the theoretical noise limit of the system strain measurement. These calculations are based on simple thermal noise estimates. The theoretical estimation will be later on compared to the measurements to see if our designed system is working at or close to theoretical limits.

This chapter includes the following sections, Power Losses in the various components, System Power Budget, Output power and Theoretical Calculation of Output Voltage Vs Strain

3.1 Power Losses in the Various Components

The power input from the signal generator is 9dBm. The signal goes through the system and has some losses here and there in reference path and signal path. The reference path connects the signal generator and the Local Oscillation port of the mixer. The signal path includes a phase shifter, a cavity sensor a 50 ohm attenuator and connects to the RF port of the mixer. In this section, all the losses in the paths will be discussed. This is important in estimating the theoretical noise limits.

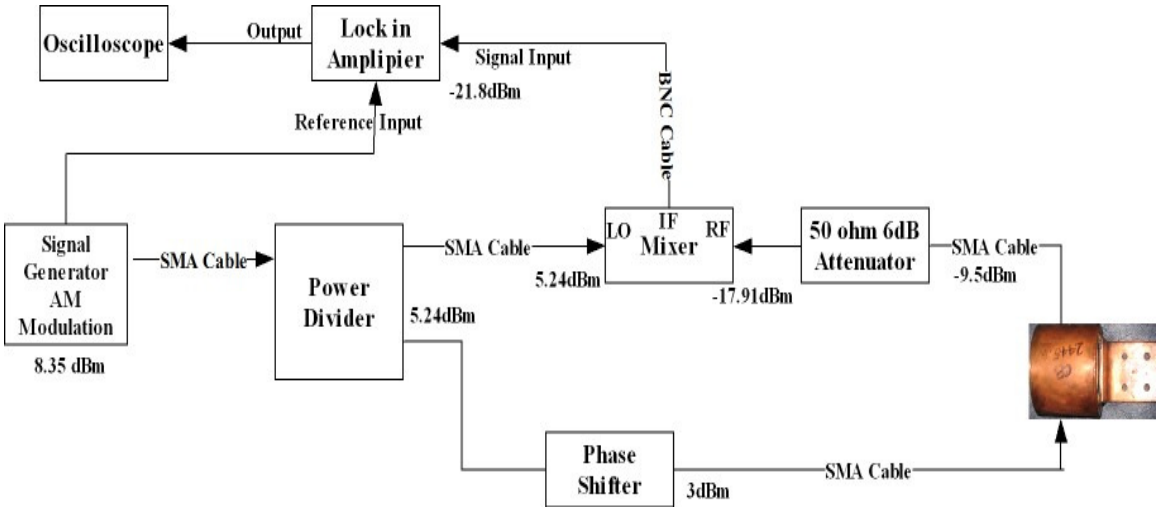

Figure 3.1 System Block Diagram

The power divider datasheet shows that the maximum insertion loss of the MCL ZAPD-21 divider is -1dB. Therefore, the power loss for the power divider is considered to be -1 dB.

The power divider splits the 9dBm input evenly into two signal paths. There is a -3dB loss for each branch as the power in each branch becomes half of the input power. Take the -1dB divider loss into account, the power goes into each branch is 9 – 3 – 1 = 5dBm. I ignore the cable loss, and there is no other elements in the reference path, the signal going into the LO port of the mixer is therefore 5dBm.

The other path contains a phase shifter, a resonator, and a 6dB attenuator. The power losses for these elements will be considered seperately. The 6dB attenuator simply reduces the power level by 6dB. The power loss of the phase shifter is obtained by measuring its insertion loss using a Vector Network Analyzer (VNA).

The insertion loss of the phase shifter is the same as S21 in this case. It is observed that the insertion loss around the resonant frequency is approximately -0.55 dB. In our calculation, I assume a worst case scenario where the insertion loss is 1 dB. This result can be verified by the phase shifter datasheet. It shows the insertion loss of the ATM P1213 phase shifter is 0.6 dB.

The insertion losses of the two types of sensors are obtained by measuring the scattering parameter S21 versus frequency using VNA. The results are shown below.

Figure 3. shows the insertion loss of the diaphragm sensor. This resonator resonates at two frequencies. Two resonant frequencies correspond to two Q factors. In our design, I used both of the two resonant frequencies and Q factors. The insertion loss of the low Q condition is around – 1.4dB, and I consider it to be -2dB in the noise calculation. The insertion loss for the high Q condition is around - 6.8dB, and I consider it to be -7dB in the noise calculation.

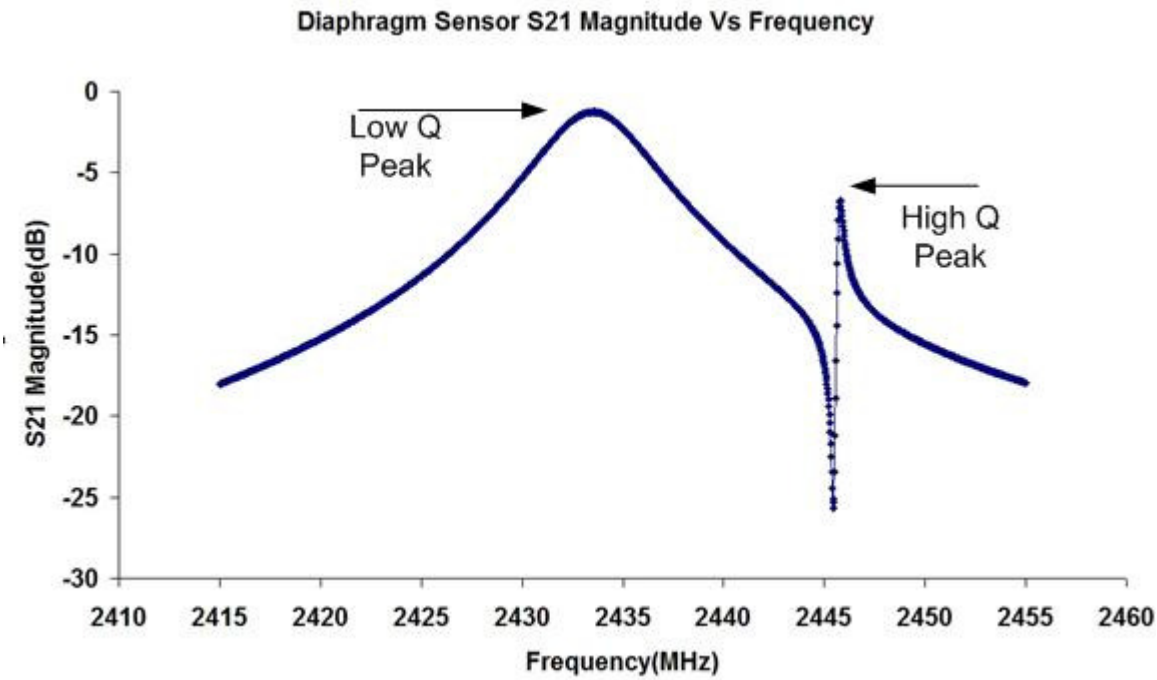

Figure 3.2 Diaphragm Sensor Scattering Parameter S21 Mag vs Frequency

Figure 3.3 shows the Diaphragm sensor scattering parameter S21 phase vs Frequency. The phase changes by 360. The VNA has its limitation in plotting the phase that is why I added 360^{o} to the curve to compensate for the error.

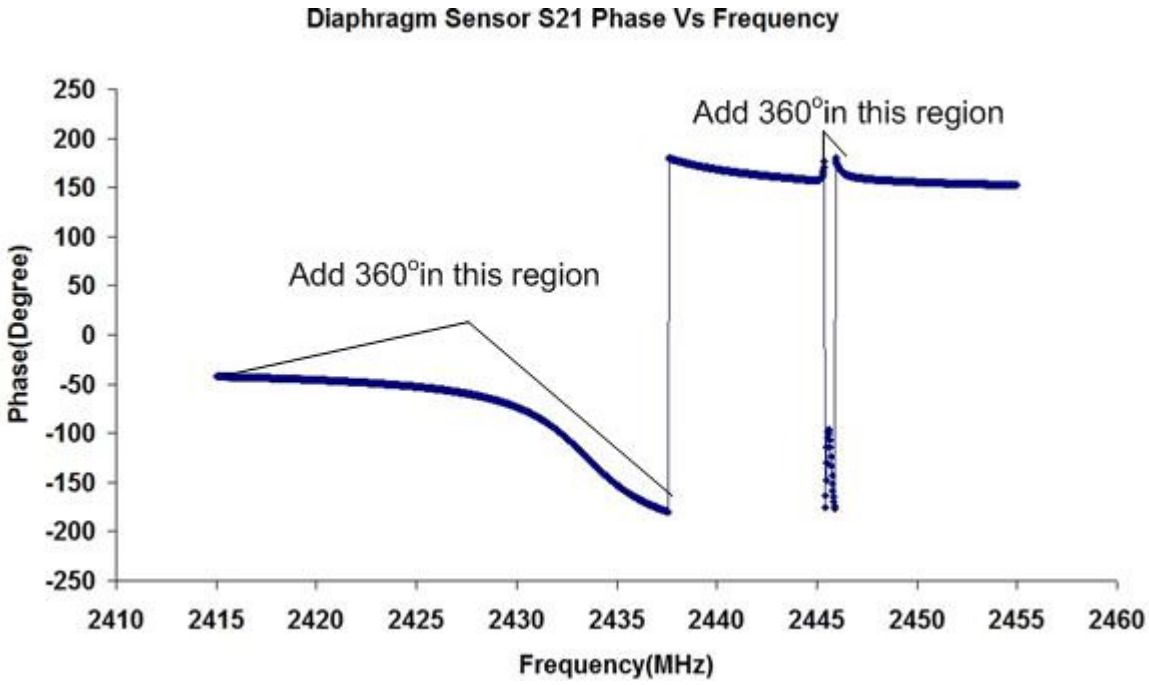

Figure 3.3 Diaphragm Sensor S21 Phase vs Frequency

Figure 3.4 shows the magnitude of scattering parameter S21 of the cylinder sensor versus phase. This sensor has only one resonant frequency and thereby has only one Q factor. The insertion loss of this sensor is around -3.7 dB and in the noise calculation, I consider it to be -4dB for simplicity.

Figure 3.5 shows the phase of scattering parameter S21 of the cylinder sensor. From the plot I can see a roughly 180 degree phase shift which is as expected since there is only one resonant frequency.

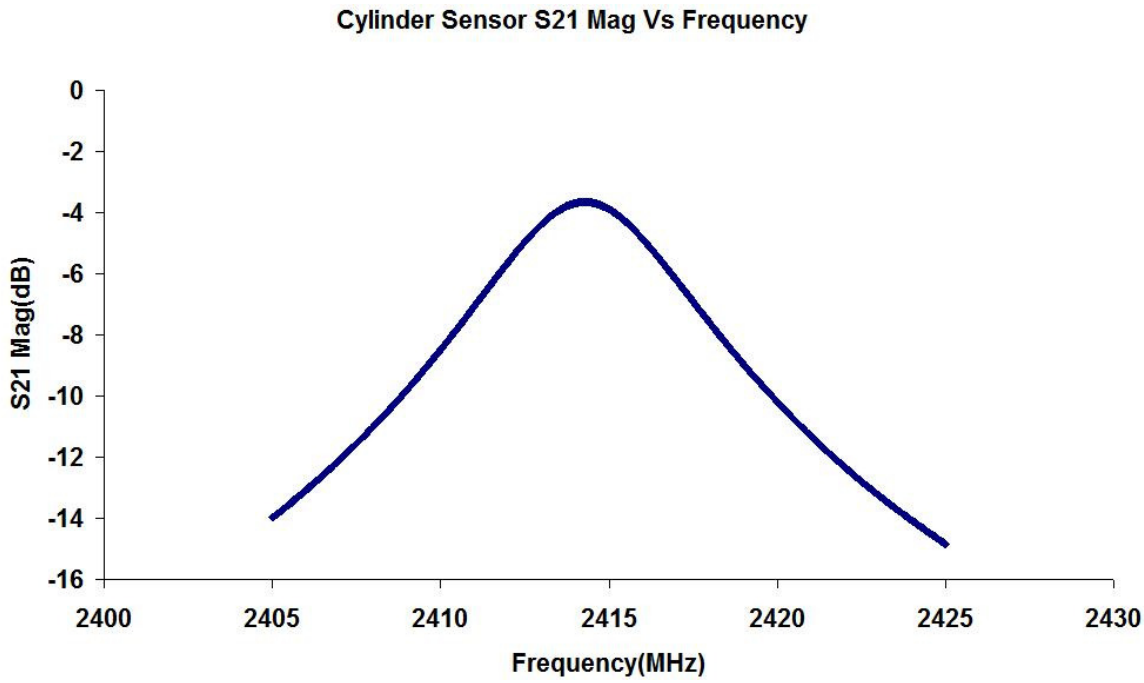

Figure 3.4 Cylinder Sensor Scattering Parameter S21 Mag vs Frequency

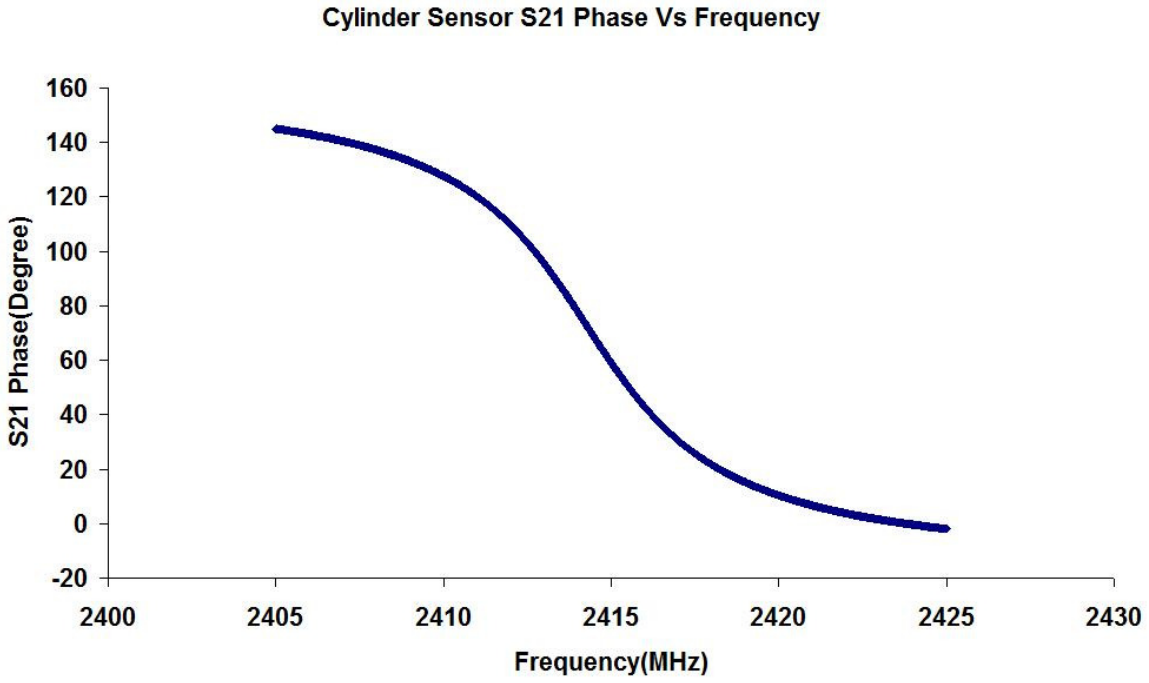

Figure 3.5 Cylinder Sensor S21 Phase vs Frequency

3.2 Power Budget

The mixer has three ports, i.e. Local Oscillation port, Radio Frequency port and Intermediate Frequency port. The power that goes into the LO port of the mixer is calculated as 5dBm. The power going into the second path is also 5dBm. The power loss of the phase shifter is -1dB. There is also a -6dB power loss due to the attenuator in the path. If I use the diaphragm sensor in the system, I would have a -2dB power loss for the low Q condition and -7dB power loss for the high Q condition. If I use the cylinder sensor in the system, I would have a power loss of -4dB. Therefore, the power that goes into the RF port of the mixer is -4dBm for diaphragm sensor low Q condition, -9dBm for diaphragm sensor high Q condition and -6dBm for cylinder sensor.

Now I will take a look at the frequency mixer. As discussed in chapter 2, the frequency mixer I used in the system is a Mini Circuit Level 7 mixer. It requires a LO drive power of 7dBm. In the design, I have 5dBm power going into the LO port of the mixer that will meet the driving power requirement. The 1dB compression point of the mixer is 1dBm. As mentioned above, in our design, the power that go into the RF port of the mixer is well below this point.

The actual values of the power level at various points as a comparison to the estimated ones are shown in table 3.1.

Table 3.1 Summary of Measured and Estimated Power level at Various Points

	RF supply	Signal going into Mixer LO	Signal going into Mixer RF
Cylinder Sensor Estimated	9dBm	5dBm	-6dBm
Cylinder Sensor Measured	8.33dBm	4.77dBm	-7.18dBm
Diaphragm Sensor Low Q Estimated	9dBm	5dBm	-4dBm
Diaphragm Sensor Low Q Measured	8.33dBm	5.05dBm	-9.52dBm
Diaphragm sensor High Q Estimated	9dBm	5dBm	-9dBm
Diaphragm Sensor High Q Measured	8.35dBm	5.24dBm	-17.91dBm

3.3 Output Power

The system output power depends on a variety of factors such as the input power supply, losses in the cable and connections, losses in the resonator cavity, etc. If I assume the RF supply is fixed at 9dBm and the losses in other elements are also fixed, then the output power is solely determined by the loss in the resonator cavity. The plot of output power versus different power loss in the resonator cavity is shown in figure 3.6.

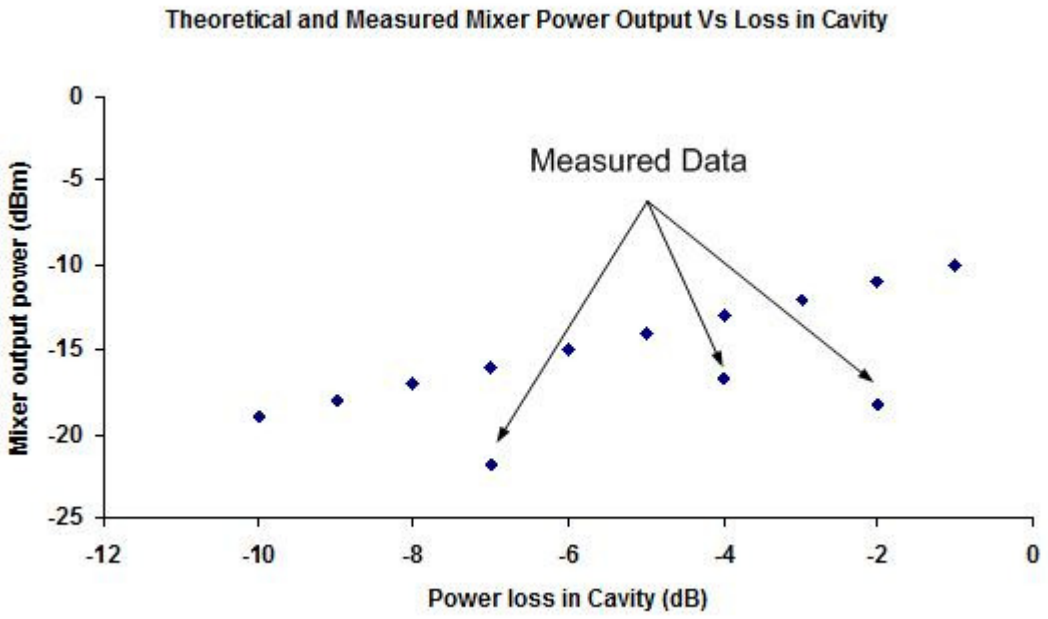

Figure 3.6 Theoretical Calculation of Mixer Power Output vs Loss in Cavity

3.4 Theoretical Calculation of Output Voltage versus Strain

To make a theoretical calculation of output voltage versus strain, I choose the cylinder sensor as an example. The power at the output of this sensor is estimated to be -13dBm, and the measurements show that the actual power output is around -17dBm. In the theoretical calculation, I use the estimated value.

The sensor output power is -13dBm which is approximately equal to 50 microwatts. I can find the output voltage using the formula

$$V_{out} = \sqrt{P_{out} \bullet Z_{system}} = \sqrt{50 \times 10^{-6} \times 50} = 50mV$$

The measured signal output peak-to-peak voltage from the oscilloscope is 40 mV. This value is in consistence with the measured power output, which is -17dBm.

The noise of the system operating at the thermal noise limit is mainly coming from the thermal noise, thus

$$V_{noise} = \sqrt{4K \bullet T \bullet R \bullet BW} \tag{3.1}$$

where K is the Boltzmann's constant, T is the room temperature, R is the system impedance, and BW is the system bandwidth.

The temperature T is assumed to be 300K, the system impedance is 50 ohms, and the bandwidth BW is determined by the Lock-in amplifier time constant or integration time. In our design, I tested 3 different time constants, which are 1ms, 10ms and 100ms respectively. In this calculation, I choose a 1ms time constant, thus,

$$BW = \frac{1}{2\pi \bullet TC} = \frac{1}{2 \times \pi \times 1 \times 10^{-3}} = 160Hz$$

Therefore,

$$V_{noise} = \sqrt{4K \bullet T \bullet R \bullet BW} = \sqrt{4 \times 1.38 \times 10^{-23} \times 300 \times 50 \times 160} = 12nV$$

Now, I will calculate the output voltage versus strain $\frac{dV}{d\varepsilon}$. I know that

$$\frac{dV}{d\varepsilon} = \frac{df}{d\varepsilon} \bullet \frac{d\phi}{df} \bullet \frac{dV}{d\phi} \tag{3.2}$$

The sensor resonant frequency can be expressed as

$$f_r = \frac{c}{2L \times \sqrt{\varepsilon_r}} \tag{3.3}$$

where c is the speed of light, L is the length of the cavity sensor, and ε_r is the relative permittivity of the medium (in our case $\varepsilon_r \approx 1$).[21] Therefore, the resonant frequency can be simplified as

$$f_r = \frac{c}{2L} \tag{3.4}$$

This is the resonant frequency without strain. As discussed in Chapter 1, when the structure material which the sensor is embedded or mounted is under stress or compression, the sensor's physical length will be forced to change. This will result in a resonant frequency shift. The resonant frequency with strain applied is expressed as

$$f_{strained} = \frac{c}{2(L + \Delta L)} = \frac{c}{2L \bullet (1 + \varepsilon)^{-1}} \approx \frac{c}{2L \bullet (1 - \varepsilon)} = f_r \bullet (1 - \varepsilon) \text{[21]} \tag{3.5}$$

where c and L are the same as above, and $\varepsilon = L / \Delta L$ is a small number called strain.

Therefore, I have obtained the first term in equation 3.2 as

$$\frac{df}{d\varepsilon} = -f_r \tag{3.6}$$

The second term in equation 3.2 $\frac{df}{d\phi}$ can be defined using the diagram below.

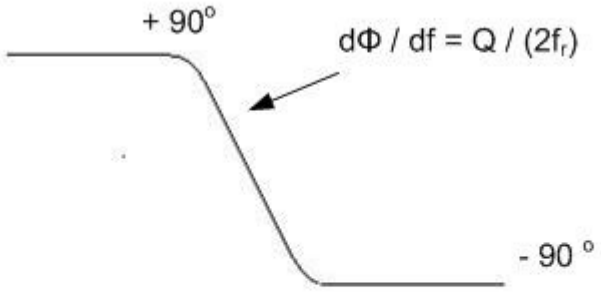

Figure 3.7 Change of Phase versus change of frequency

The change of phase over change of frequency is determined by the formula

$$\frac{d\phi}{df} = \frac{Q}{2f_r} \quad [21] \tag{3.7}$$

The output voltage can be expressed as a function of phase ϕ, which is,

$$V(\phi) = V_{\max} \bullet Sin\phi \tag{3.8}$$

Therefore,

$$\frac{dV}{d\phi} = V_{\max} \bullet Cos\phi \tag{3.9}$$

In the design, I use the phase shifter to null out the phase. This means the phase ϕ is close to zero all the times. From basic trigonometry, $Cos\phi$ is approximately 1 when ϕ is close to zero.

Therefore, equation 3.9 can be simplified as follows.

$$\frac{dV}{d\phi} = V_{\max} \tag{3.10}$$

Based on equation 3.6, 3.7, and 3.10, I can rewrite equation 3.2 as follows.

$$\frac{dV}{d\varepsilon} = -f_r \bullet \left(\frac{Q}{2f_r} \right) \bullet V_{\max} = -\frac{Q}{2} \bullet V_{\max} \tag{3.11}$$

In other words, $\frac{\Delta V}{\Delta \varepsilon} = -\frac{Q}{2} \bullet V_{\max}$, and thus,

$$\Delta\varepsilon = \frac{\Delta V}{V_{\max}} \bullet \frac{2}{Q} = \frac{\sqrt{4K \bullet T \bullet R \bullet BW}}{\sqrt{P_{out} \bullet Z_{system}}} \bullet \frac{2}{Q} \approx 1.2n\varepsilon \tag{3.12}$$

for Q = 400, T = 300K, R = 50Ω, BW = 160Hz, P_{out} = 50uW, Z_{system} = 50Ω.

By implementing the same procedures, I can calculate the output voltage and strain for the diaphragm sensor low Q and high Q conditions. The only difference from the cylinder sensor calculation is that I used

$$\frac{df}{d\varepsilon} = 5MHz/mm \times 9cm = 450MHz \ .$$

This is based on the existing research paper except in the paper, the authors conclude a 7MHz/mm and I use the 5MHz/mm to the specific sensor I used in the design. [21] The 9cm is the sensor cavity length. In reality the length should include the rod as well, but here I assume rod has no length. Table 3.2 shows the results for different sensors and conditions. All the data values used are from the theoretical estimates.

Table 3.2 Summary of Strain Variations and Output Voltage of Different Sensors

	P_{out} (dBm)	V_{out} (mV)	$\Delta\varepsilon$ (nε)
Cylinder Sensor	-13	50	1.2
Diaphragm Sensor High Q	-16	35	0.59
Diaphragm Sensor Low Q	-11	63	5.0

The actual resolutions for diaphragm sensor is smaller than what shown in the table because I assume the sensor rod has zero length.

3.5 Various Q Factors versus Sensor Strain Change

The strain change $\Delta\varepsilon$ is proportional to voltage variation ΔV and inversely proportional to V_{max} and Q. The voltage variation noise ΔV is fixed at 12nV for our system. The output voltage and Q factors can be varied and result in different strain values.

Table 3.3 shows the summary of Q factor and resonant frequency for different sensors. These data were measured using a Vector Network Analyzer (VNA). To make a theoretical estimation, I also assume the output voltage V_{max} is fixed. Therefore, the only factor that can change is Q, and hence I can make a plot of strain changes versus Q.

Table 3.3 Q Factors and Resonant Frequency Summary for Different Sensors

	Resonant Frequency (MHz)	Q factor
Cylinder Sensor	2414.00	401.0
Diaphragm Low Q	2433.90	419.6
Diaphragm High Q	2445.90	6310.4

Figure 3.8 is the plot of minimum detectable strain versus Q for two different output power levels. I have plotted two cases together in one plot, i.e. when V_{max} is equal to the output power for Low Q condition, which is 63 mV and when V_{max} is equal to the output power for High Q condition, which is 35 mV. With the V_{max} being fixed, the quality factor Q is inversely proportional to strain variation. This figure also shows the two measured data points as a comparison to the estimated data points. The difference may be due to the extra cable and connection loss in the branch which results in a lower power output than the estimated values. There may also be some additional sources of noise such as electronic noise and noise due to vibration

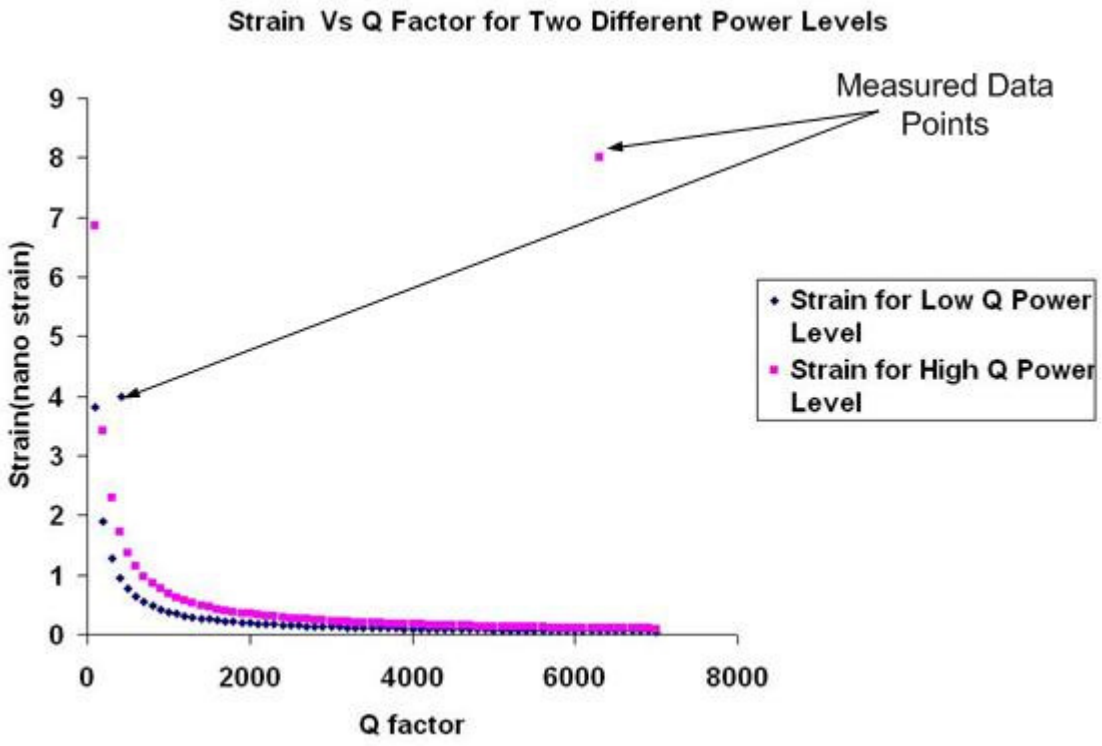

Figure 3.8 Strain vs Q factors for Low Q and High Q Power Level

4. Chapter IV Results

In this chapter, results will be shown for measurements of sensor properties and of the minimum detectable strain. Some of the results were collected under carefully controlled laboratory conditions, and some during application on model structures. These results are then compared with the theoretical calculation.

This chapter includes the following sections, Mixer Output Voltage, Cylinder Sensor Thermal Scaling, Cylinder Sensor Noise vs Time Constant, Structure Lab Diaphragm Sensor Strain Testing, Diaphragm Sensor High Q Noise, and Diaphragm Sensor Low Q Noise.

4.1 Mixer Output Voltage

In chapter 3, I have already shown the theoretical calculation of mixer output voltage for different sensors and conditions. Now, I will show the lab test results for these output voltages and compare these to the theoretical calculation.

The following figures show the lab test results of the mixer output voltage for the cylinder sensor as an example. From figure 4.1, I can clearly see that the mixer output voltage and the RF generator voltage is in phase.

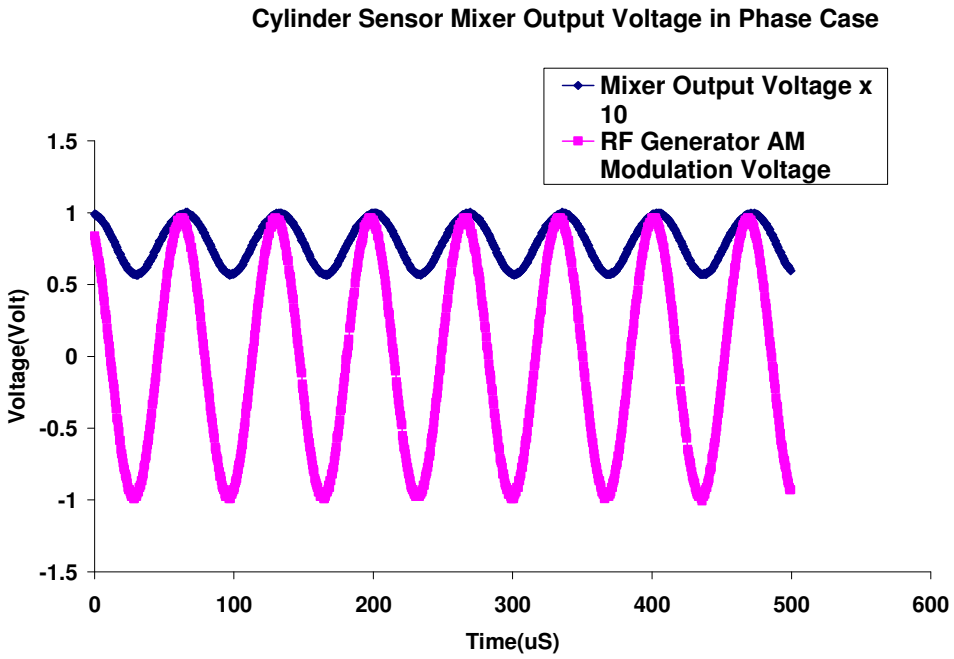

Figure 4.1 Cylinder Sensor Mixer Output Voltage vs RF Generator Voltage Modulation Signal

. The voltage is approximately 40 mV peak-to-peak and the RMS value is 14.2mV. The estimated value is 50 mV. As mentioned in Chapter 3, the system output power has a uncertainty of 4dB. If I take this into consideration, I will get a worst scenario power output of -17dBm which is consistent with the power meter measurement. This will result in a 31.6mV output voltage following the calculation in chapter 3 assuming 100% AM modulation index. The actual modulation depth is 60% in lieu of 100%. Therefore, the estimated output voltage should be $31.6 \times 60\% = 18.96mV$. This is in good agreement with the measured value.

Figure 4.2 shows the cylinder sensor mixer output voltage compared with the RF generator voltage for the phase shifter adjusted to midway between maximum signal and minimum signal. From this figure, I can see that when the

phase is in half way, the mixer output voltage almost goes to zero, which is as expected.

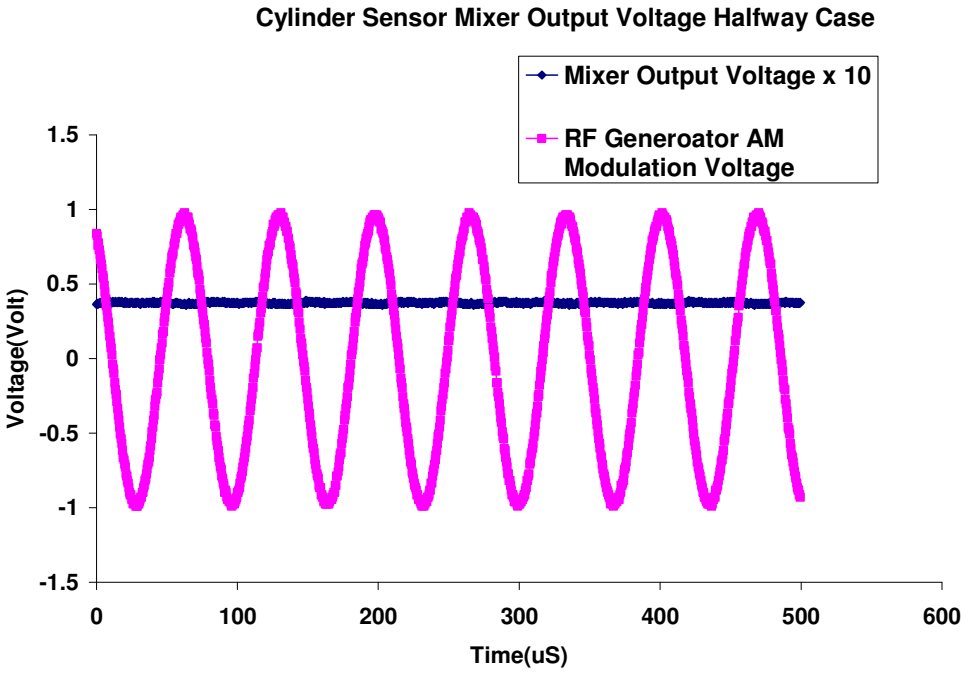

Figure 4.2 Cylinder Sensor Mixer Output Voltage versus RF Generator Voltage Modulation Signal Midway

Figure 4.3 shows the out-of-phase case of the mixer output voltage and the RF generator voltage. From this figure, I can see that the two voltages are 180 degree out-of-phase, which is the result of adjusting the phase shifter. The magnitude of the mixer output voltage is magnified by 10 times to make the curve more visible.

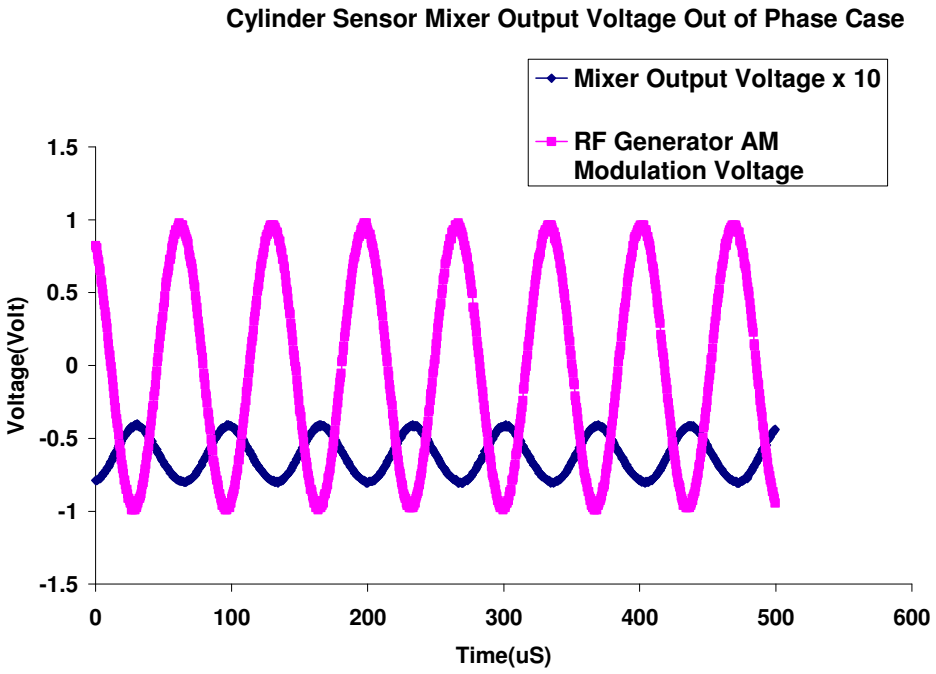

Figure 4.3 Cylinder Sensor Mixer Output Voltage versus RF Generator AM Modulation Voltage Signal Out-of-Phase

The magnitude of the output voltage is approximately 40 mV peak to peak. This is in agreement with the measured output power from the RF power meter. It also matches the estimated signal power if I take the uncertainty of output power into consideration.

Similar measurements were made of the output voltage for the diaphragm sensor. This sensor case is quite similar to the cylinder sensor case. The Magnitude of the mixer output voltage for the high Q condition in phase case is around 20mV peak to peak and 14.1mV RMS. The estimated output voltage is 35 mV and the output voltage calculated using the RF power meter result is 18mV. The difference between the estimated value and the measured value is

due to the loss in the cable and connection and it is also due to the uncertainty in power output. The magnitude of the mixer output voltage for the out-of-phase case is around 15mV peak-to-peak. The magnitude of the mixer output voltage is close to zero when the phase shifter is adjusted to the midway phase which is as expected.

From the discussion in Chapter 3, I know that the mixer output voltage is a sinusoidal function of ϕ. I measured the mixer output voltage pattern when adjusting the phase shifter through 360 degrees. The AM modulation was turned off in the RF function generator. I only measure the DC mixer output voltage here. I used the 20dB attenuator in the test. I did this for the cylinder sensor, the diaphragm sensor and one without connecting any sensor.

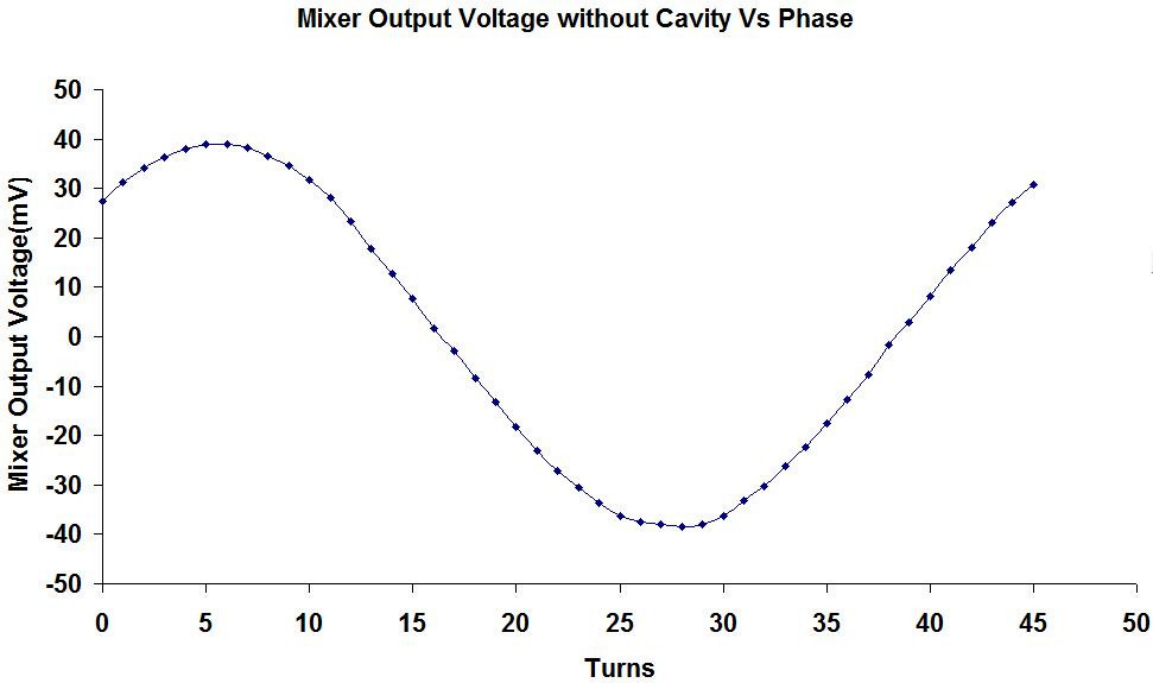

Figure 4.4 Mixer Output Voltage vs Phase with 20dB Attenuator instead of Cavity sensor

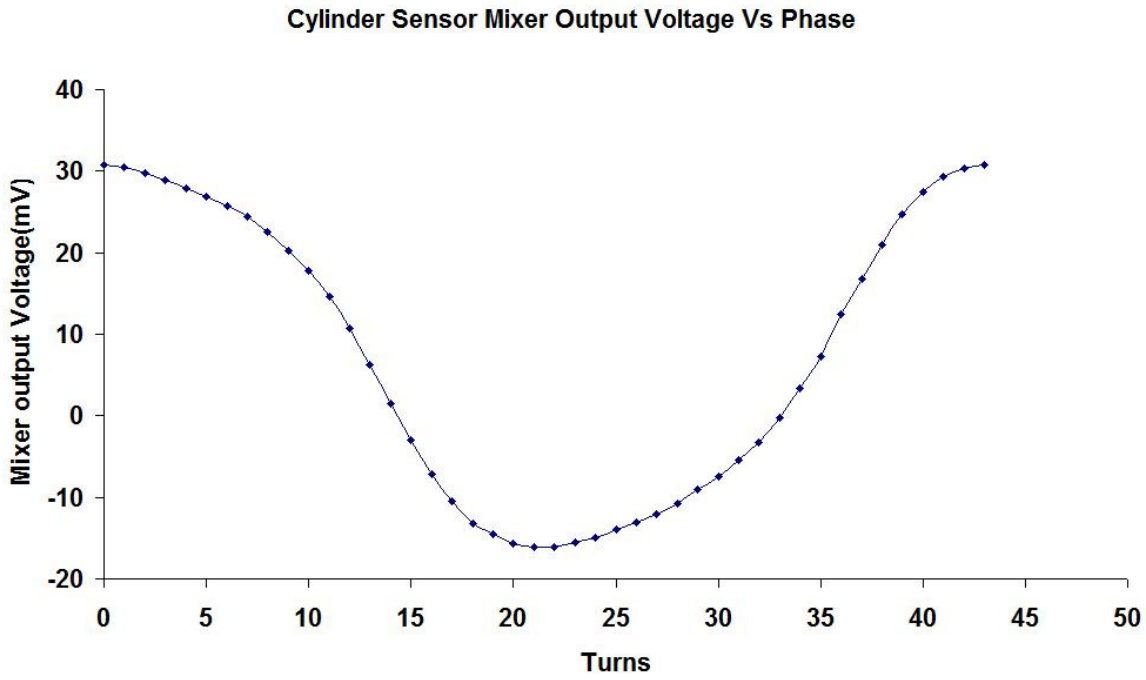

Figure 4.5 Cylinder Sensor Mixer Output Voltage vs Phase

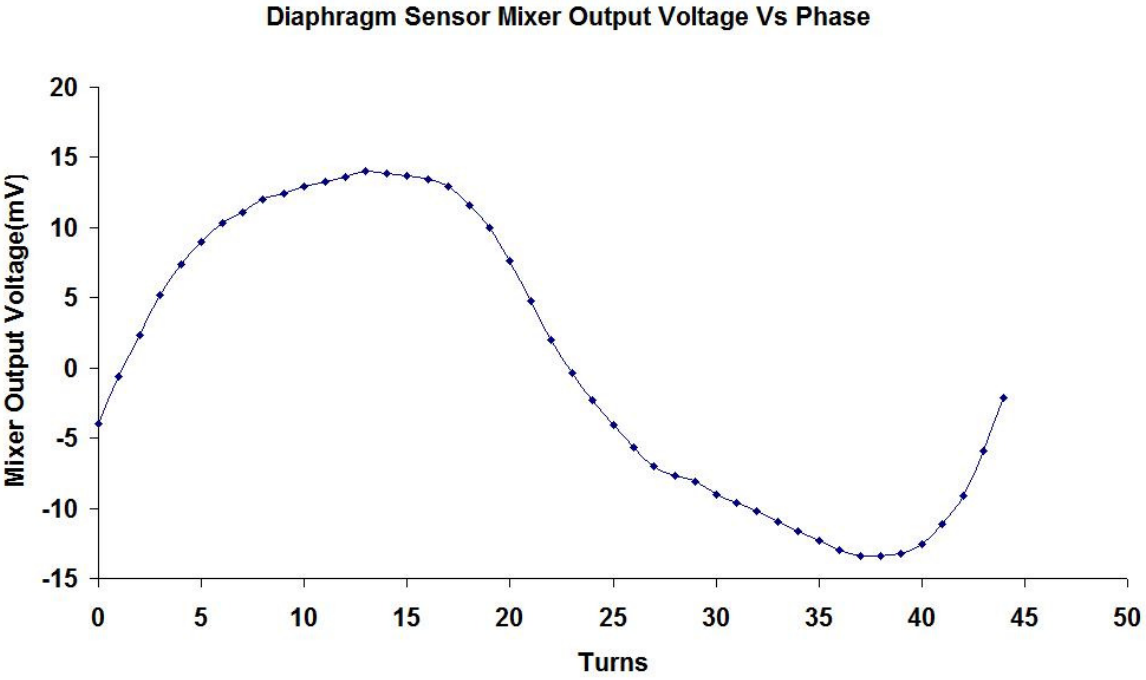

Figure 4.6 Diaphragm Sensor Mixer Output Voltage vs Phase

These figures above show that the mixer output voltage is indeed a sinusoidal function of the phase. For the no cavity case, it is pure sinusoidal. For the two cavity cases, there are some harmonics involved in the measurements, so they are not pure sinusoidal. The harmonics are probably from the signal generator and goes to the mixer through the reference path. However, our system only uses the slope where the signal is close to zero, so the harmonics will not matter that much. If I change the resonant frequency in the function generator the average DC voltage also changes. The reason is that the DC level is also dependant on the phase. When I change the resonant frequency, the phase will also change, and this will cause the DC level to change.

Using the results from these three figures, I can calculate how many degrees in phase for each turn. For the no-cavity case, from maximum to minimum voltage, there are 23 turns. Therefore, each turn accounts for 180^o / 23 = 7.8^o or 0.137 rads. For the cylinder sensor case, each turn accounts for 360^o / 43 = 8.3^o or 0.146 rads. For the diaphragm sensor case, each turn is for 360^o / 43 = 8.3^o or 0.146 rads. The following three figures are the plots of mixer output voltage vs phase using the calculation above.

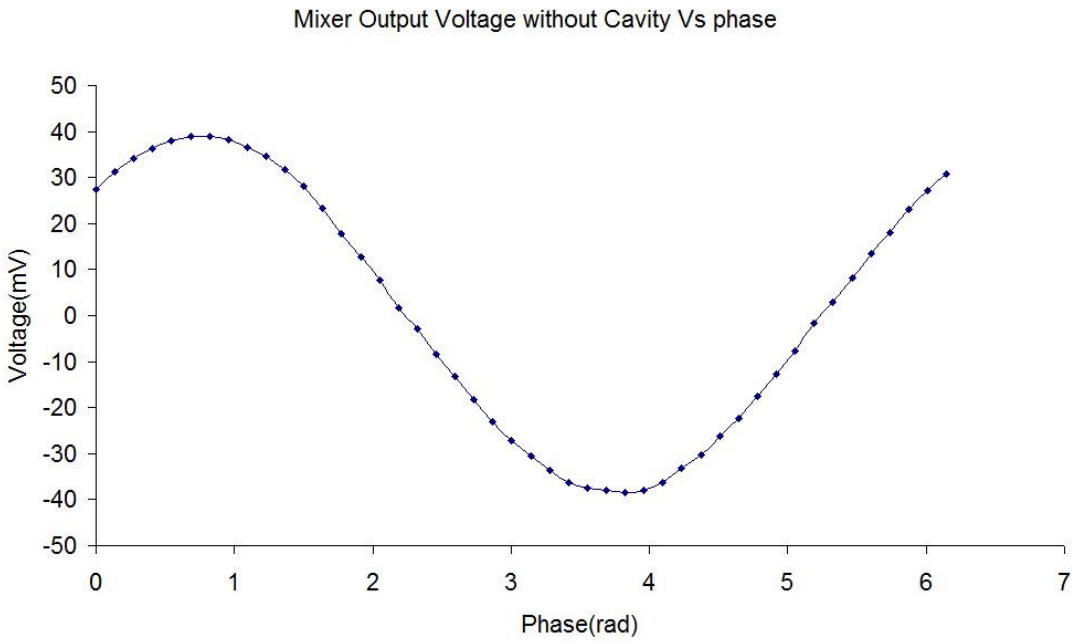

Figure 4.7 Mixer Output Voltage without Cavity vs Phase

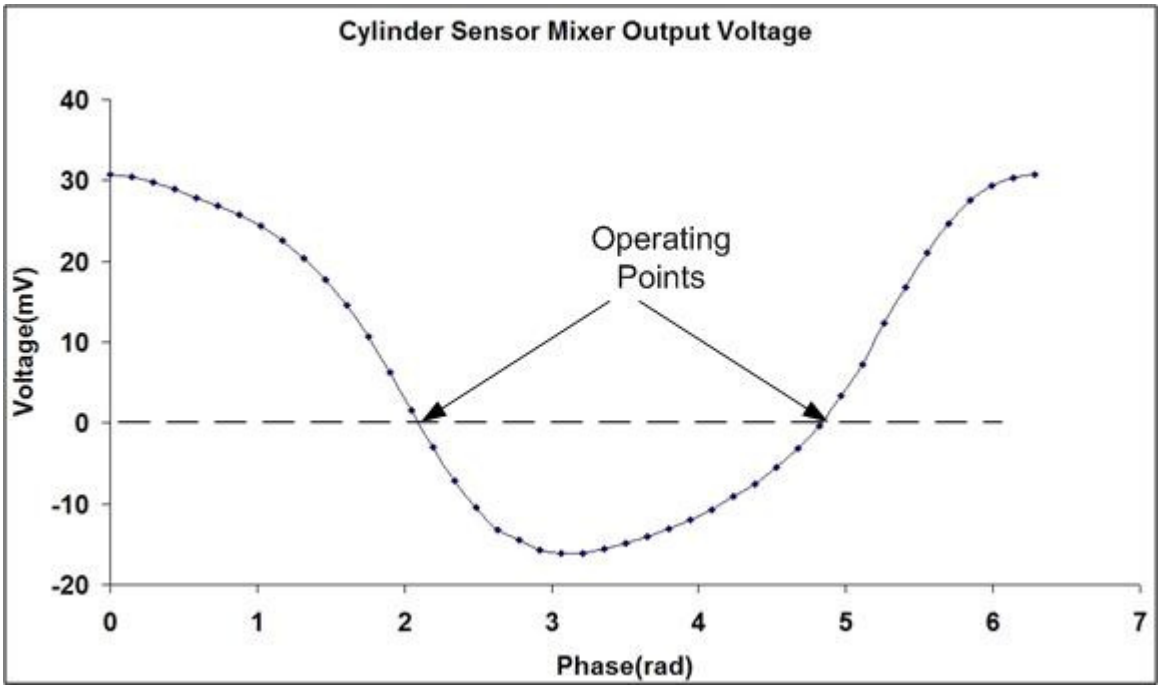

Figure 4.8 Cylinder Sensor Mixer Output Voltage vs Phase

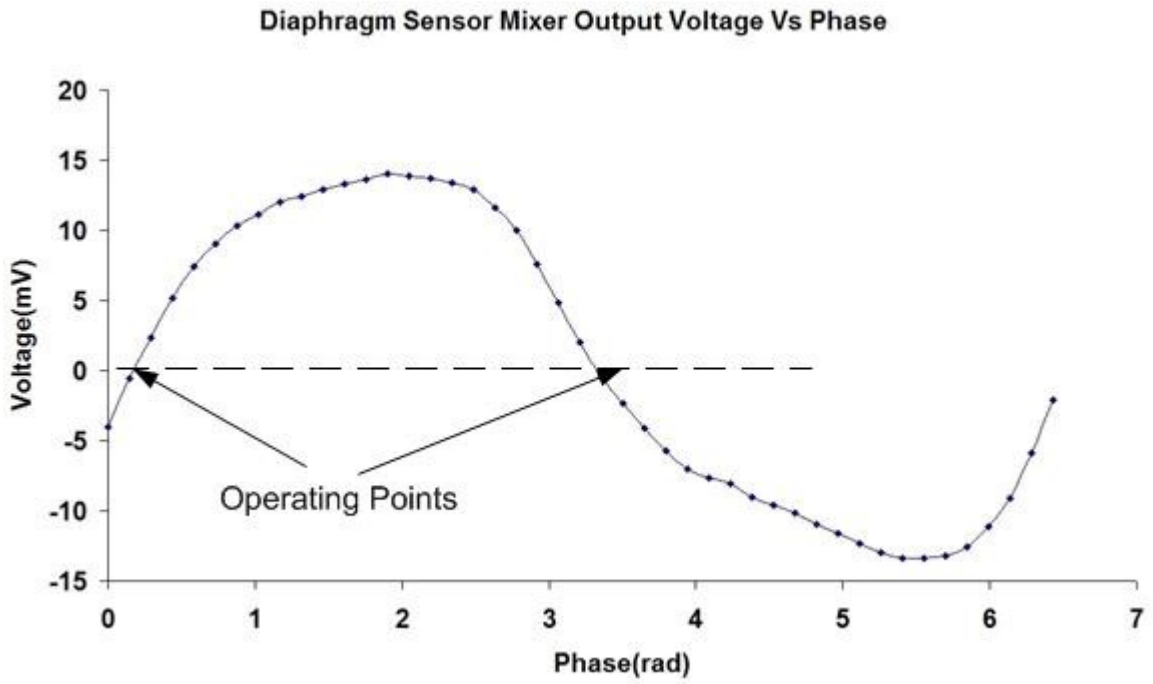

Figure 4.9 Diaphragm Sensor Mixer Output Voltage vs Phase

Using the results from these three figures, I can calculate the slope when the signal is near zero. For the no-cavity case, the slope downwards near zero is 35mV/rad and the slope upwards near zero is 33.5mV/rad. For the cylinder sensor case, the slope downwards near zero is 27.4mV/rad and the slope upwards near zero is 25.3mV/rad. For the diaphragm sensor case, the slope downwards near zero is 16.4mV/rad and the slope upwards near zero is 19.9mV/rad.

The estimated value for the 20dB attenuator case is 7mV. I used the 50 ohm load impendence in the calculation. The oscilloscope I used to measure voltage is set to have a 1M ohm input impedance. Therefore, the voltage I measured from the scope is doubled compared with the estimated value.

4.2 Calibration of Cylinder Sensor Using Thermally Induced Strains

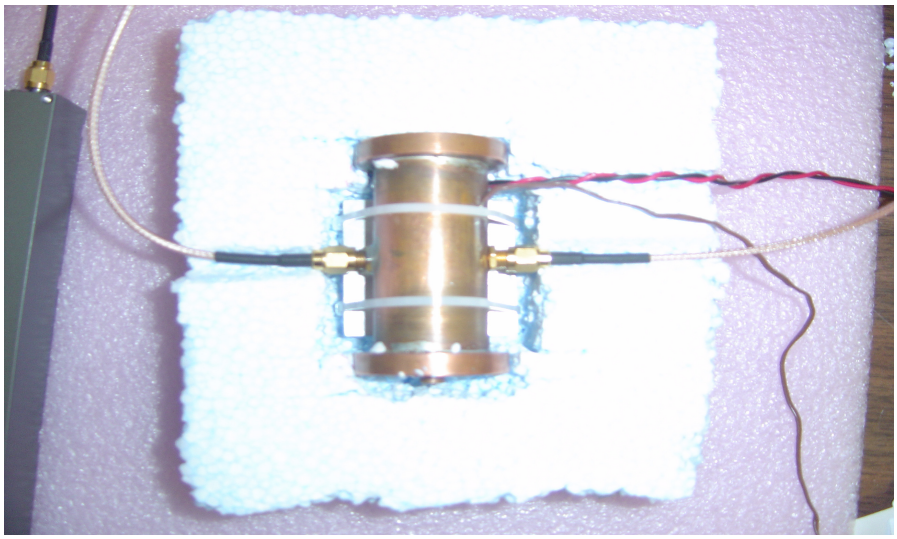

Figure 4.10 Cylinder Sensor Thermal Scaling Setup

In order to calibrate the interrogation system for the cylinder sensor case, I will induce thermal strains in the design. The reason for using this method is that I find it hard to apply known strain to the cylinder sensor. Therefore, I decide to use the thermal method to do the calibration. I attached a 50-ohm resistor onto the cylinder sensor. The 50-ohm resistor is wired to a 5V DC voltage power supply. When I turn on the power supply switch, the resistor will heat up. Since the resistor is in contact with the cylinder sensor, the resistor will raise the temperature of the sensor. The sensor is made of copper, which has a thermal expansion coefficient of 17 microstrain per degree Celsius (ε/C^{o}). [22]

In the lab, I used a multi-meter with thermocouple to measure the temperature change. The entire assembly was encased in a Styrofoam housing so the heat was very slow to diffuse. Essentially, heat was put in, but did not leave. I put the sensor and the resistor together into the insulation box to keep

the sensor temperature unaffected by the ambient temperature and to hold in the applied heat. I then turned on the power supply for about 300 seconds to heat the resistor and sensor and turn off the power switch after 300 seconds. I measured the temperature change for a period of 400 seconds. I also recorded the Lock-in amplifier output voltage signal for the same period of time using the digital oscilloscope.

Figure 4.11 shows the thermal scaling signal output voltage vs time. The thermal meter read that the temperature changed from 26.5 C^o to 27.4 C^o over the 400 seconds period. The temperature change is therefore 0.9 C^o. The power switch is off for the first 50 seconds and then turned on from 50s to 300s. The switch is turned off again at 300s and keeps off till the end of the 400s time period. The voltage curve shows the same pattern. From 0 to 50s and from 300s to 400s, the output voltage is relatively flat. They are not straight flat lines because there is some noise embedded in the signal which I will discuss later.

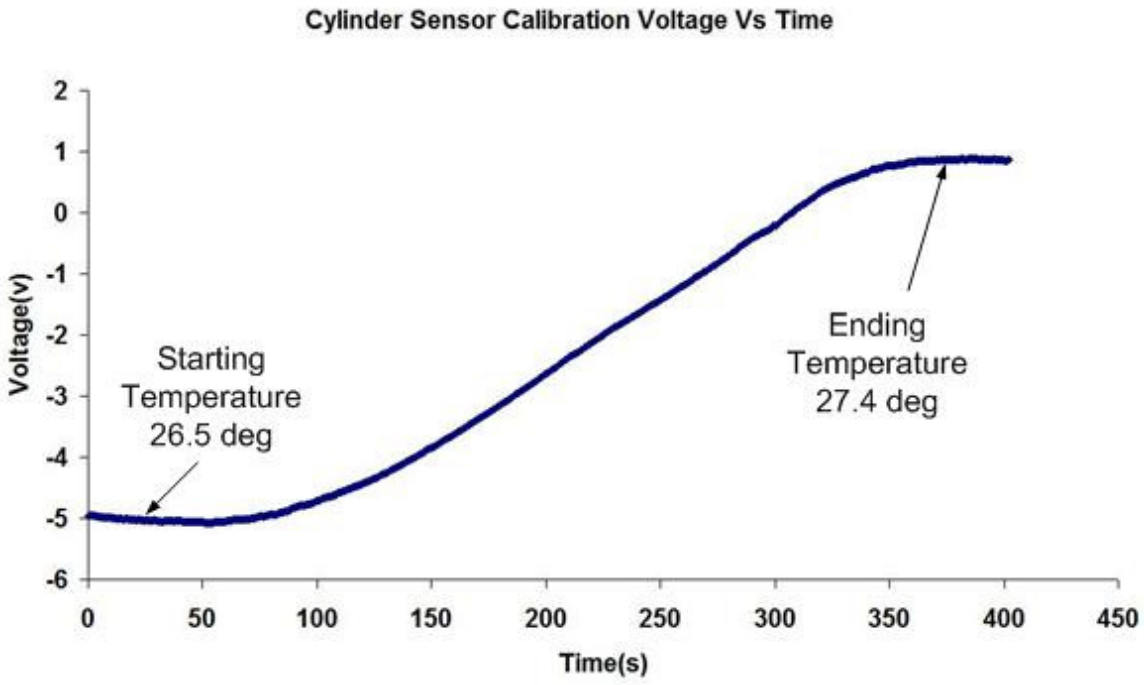

Figure 4.11 Cylinder Sensor Thermal Scaling Voltage vs Time

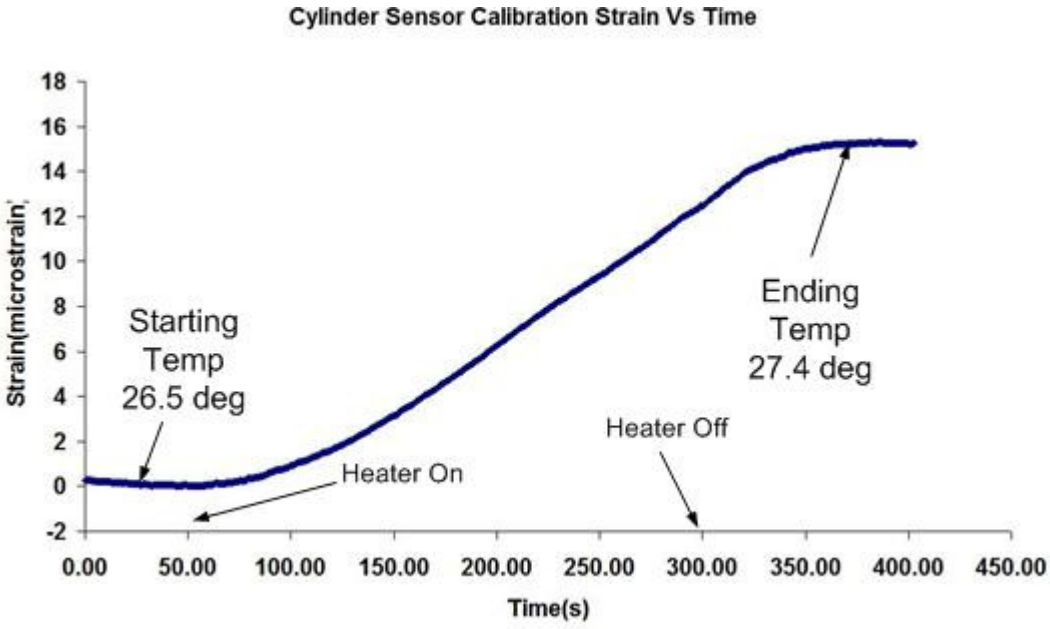

Figure 4.12 Cylinder Sensor Thermal Scaling Strain vs Time

From 50s to 300s, the output voltage keeps increasing and this forms a slope. The reason for this is that when the sensor temperature increases, the sensor will expand according to the thermal expansion coefficient. The expansion causes the sensor cavity length change and thereby resulting in a resonant frequency change. The frequency change will cause a phase shift that will be picked up by the lock-in amplifier as a change in output voltage. The two relative flat lines represent the stable state in thermal equilibrium. The difference between low and high is due to the thermal expansion and hence resonant frequency change. From figure 4.11 I can see that the voltage changes from -5.07V to 0.88V, which is a 5.95V difference.

I know the temperature change is 0.9 ^{o}C and the voltage change is 5.95V, I can calculate the relationship between strain and voltage using the thermal expansion coefficient of copper. Since copper has a thermal expansion coefficient of 17 ppm / ^{o}C, this then gives us a means of scaling voltage to strain.

$$\frac{\varepsilon}{V} = 0.9°C \times 17 \,\varepsilon/_{°C} \div 5.954V = 2.57 \,\varepsilon/_{V} \tag{4.1}$$

Figure 4.12 shows the thermal scaling strain change vs time using the strain and voltage relationship. The strain changes from 0 to 15.3 microstrain. Using this relationship, I can calculate the noise embedded in the signal.

4.3 Cylinder Sensor Noise versus Bandwidth

It is well known that total measured noise will depend on bandwidth. Based upon the calculations in chapter 3, I know that the bandwidth of the system is

limited by the Lock-in Amplifier time constant. As mentioned in the previous chapter, I chose three different time constants in our design, which are 1ms, 10ms and 100ms respectively. A larger time constant will result a smaller bandwidth and a smaller thermal noise voltage. Since the strain variation is at least partially dependant on the thermal noise, a larger time constant will tend to decrease strain variation. More precisely, referring to equation 3.1, I can see that theoretically increasing the time constant by a factor of 100 will result in a decrease in the strain variation by a factor of 10.

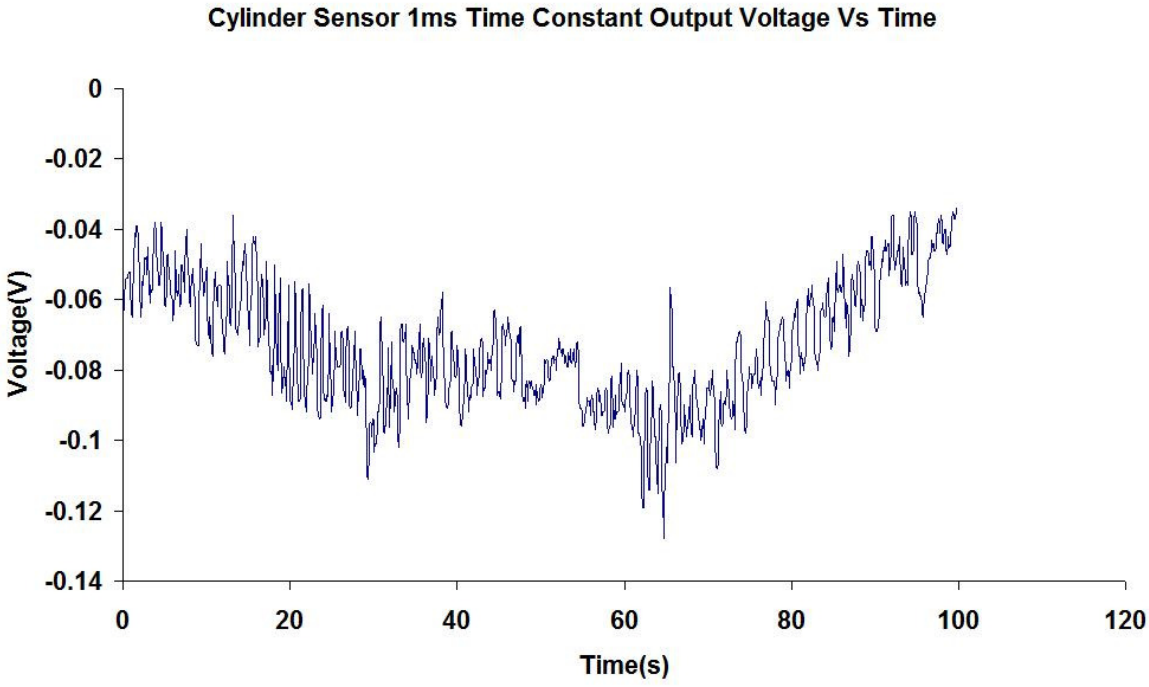

Figure 4.13 Cylinder sensor 160Hz Bandwidth Noise Voltage vs Time

Figure 4.13 shows the cylinder sensor output voltage for 160Hz bandwidth. The noise is simply random Gaussian noise with a combination of the thermal and other types of drift. I recorded the noise voltage for a period of 100 seconds.

From the plot, I can see the noise is stable with only a slight thermal drift over time. I used the voltage and strain relationship obtained from the thermal scaling technique and I plotted the noise strain vs time in figure 4.14

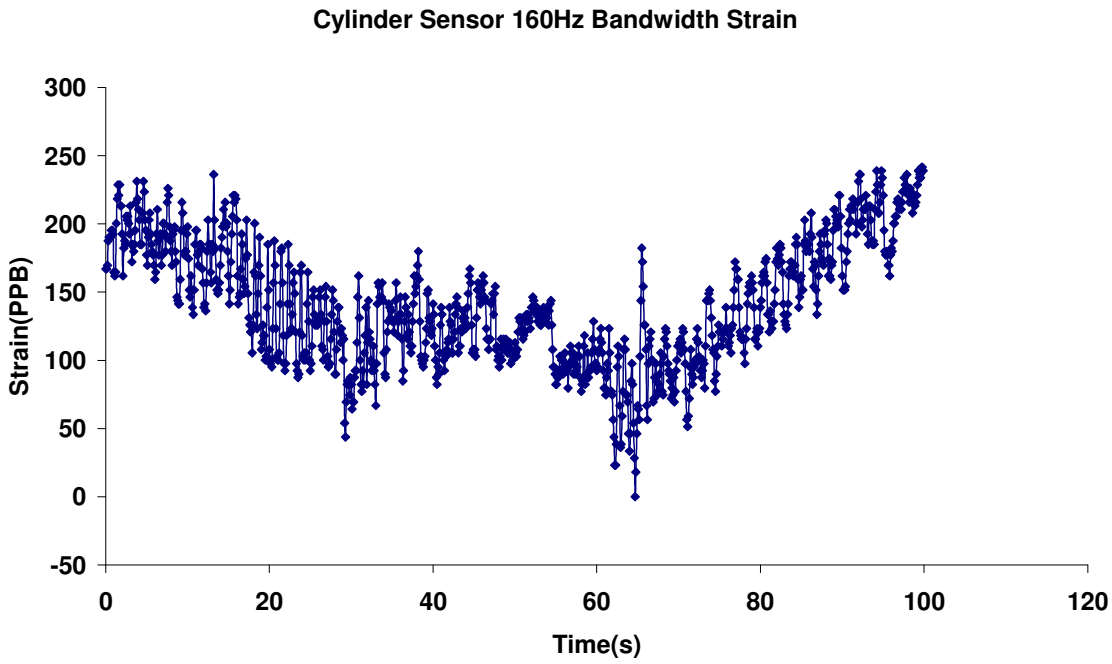

Figure 4.14 Cylinder Sensor 160Hz Bandwidth Noise Strain vs Time

Based on the noise strain, I also calculated the RMS noise of the output signal from the lock-in amplifier. I measured the noise in a 100 seconds period of time and I divided the time period evenly into ten sections where each section lasts for 10 seconds. I then calculated the RMS strain noise for each section or sample. Figure 4.15 shows the cylinder sensor 1ms RMS noise. The maximum sample noise is around 30 nanostrain and the minimum sample noise is around

20 nanostrain. The average RMS noise for the 100 second period of time is 24.5 nanostrain.

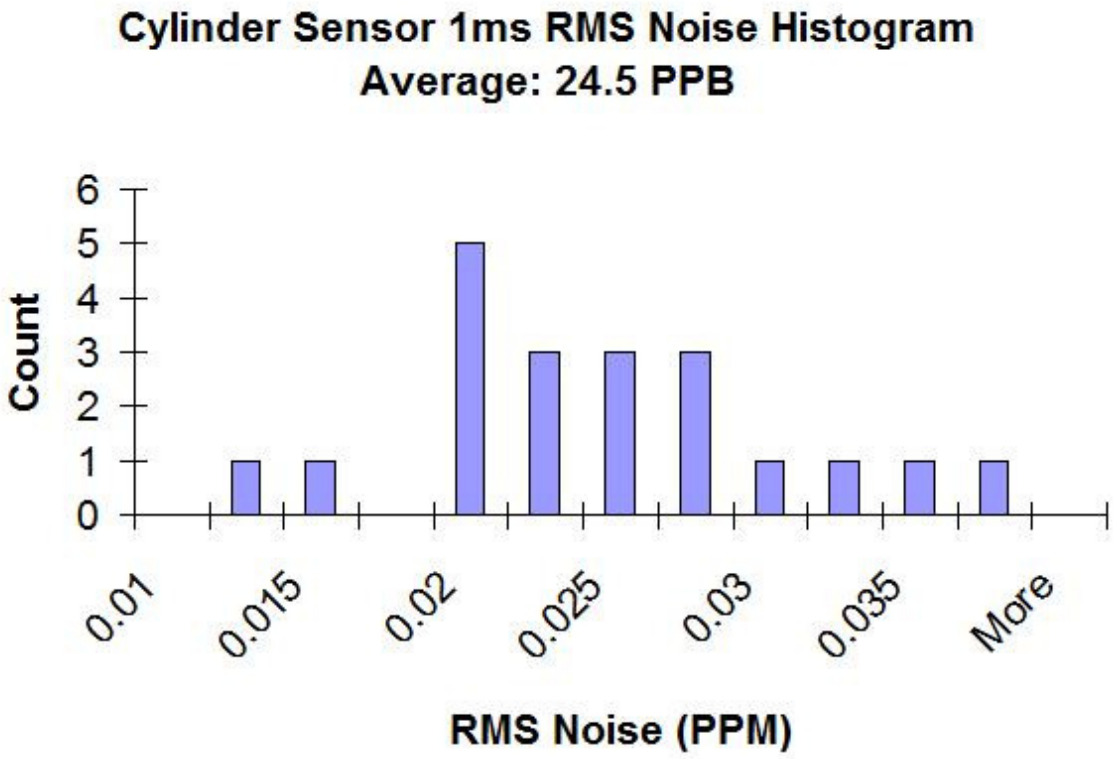

Figure 4.15 Cylinder Sensor 160Hz Bandwidth RMS Noise Histogram

Similarly, the noise voltage and strain for 16Hz bandwidth are shown in figure 4.16 and 4.17 below. From the voltage plot, I can see that the noise is simply random Gaussian noise. The noise signal is stable with only a slight thermal drift. The strain plot shows the same fact since the relationship between the voltage and strain output is linear.

Based on the strain noise plot, I can obtain the RMS noise of the 10ms time constant case using the same calculation procedure. The cylinder sensor 10ms time constant RMS noise is shown in figure 4.18

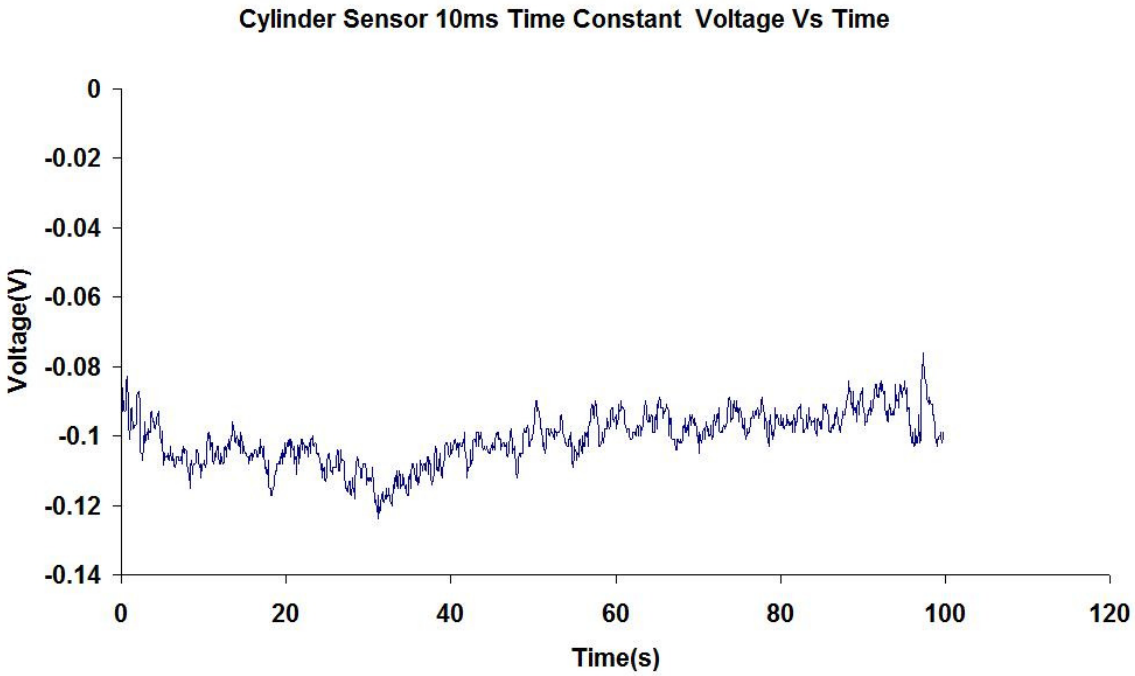

Figure 4.16 Cylinder Sensor 16Hz Bandwidth Noise Voltage vs Time

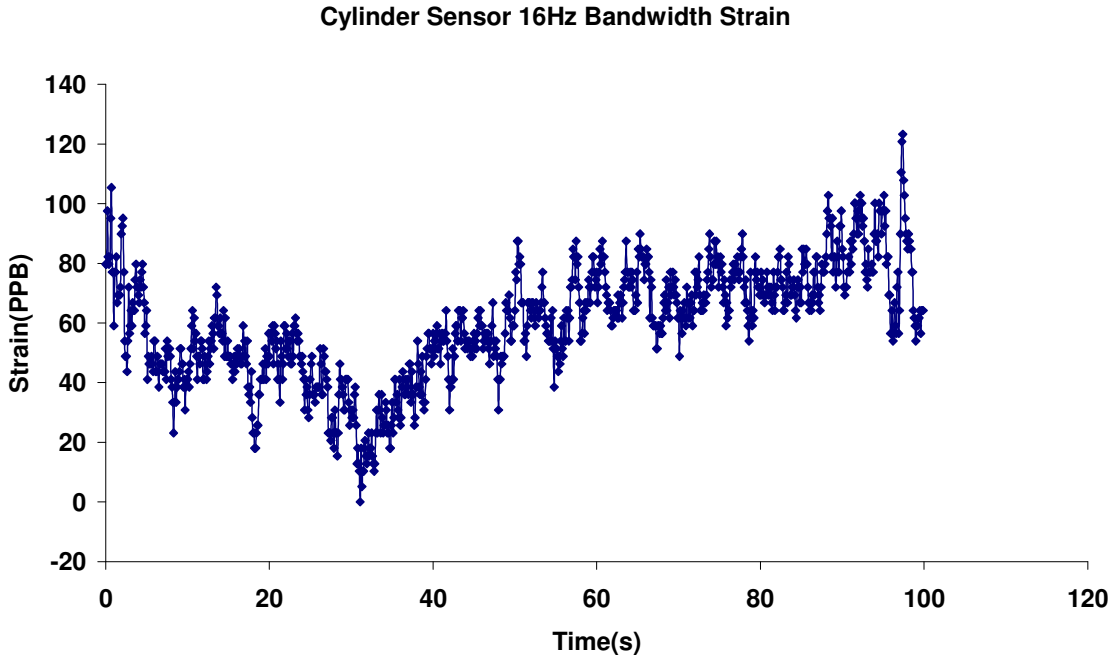

Figure 4.17 Cylinder Sensor 16Hz Bandwidth Noise Strain vs Time

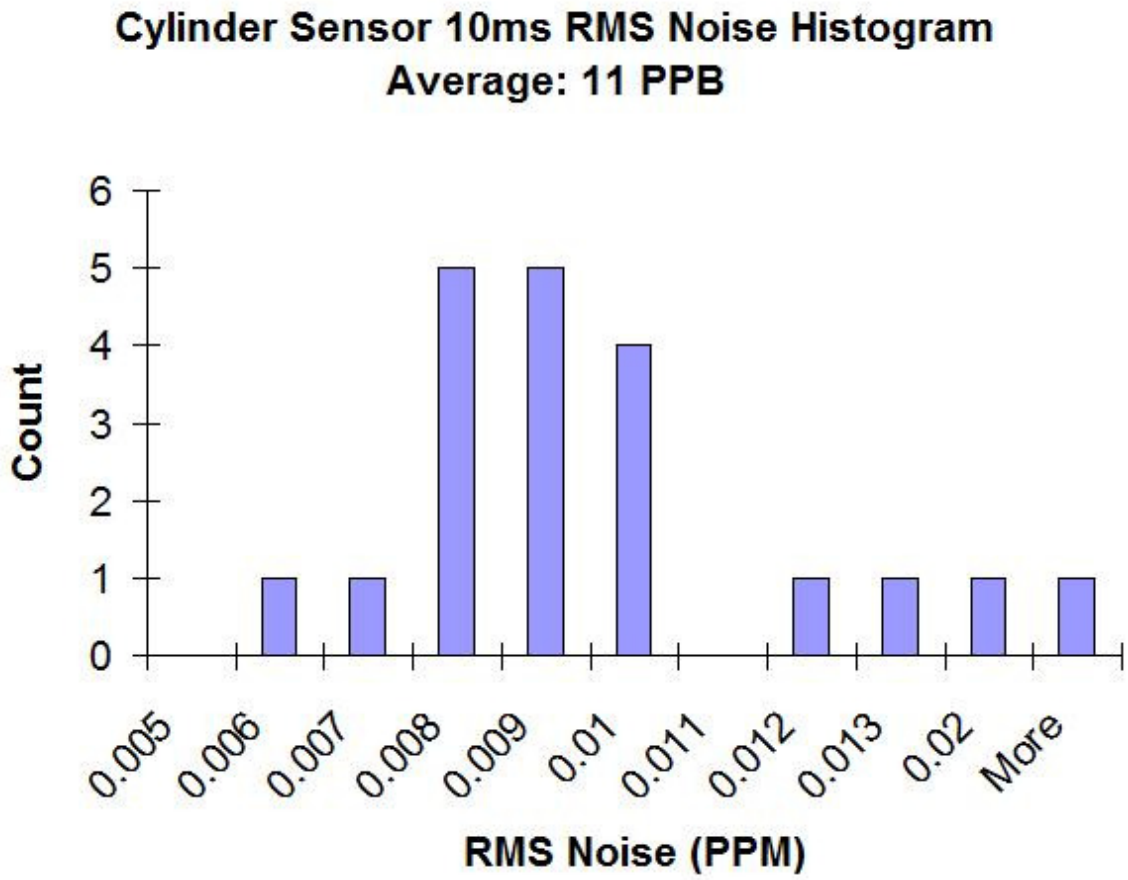

Figure 4.18 Cylinder Sensor 16Hz Bandwidth RMS Noise Histogram

Figure 4.18 shows that the maximum RMS noise is around 17 nanostrain and the minimum RMS noise strain is around 8 nanostrain. The average RMS noise for the 100 second period of time is 11.0 nanostrain. I can see that as the bandwidth decreases from 160Hz to 16 Hz, the RMS noise is reduced from 24.5 nanostrain to 11 nanostrain. In the discussion above, I mentioned that the bandwidth decreasing by a factor of 10 will cause the Strain variation to decrease by a factor of √10. In our case, the strain noise is indeed reduced. However, the strain noise is reduced by a factor of 2 rather than a factor of √10. The reason is that the noise is not purely random Gaussian noise. Instead, the noise is a

combination of the Gaussian noise, perhaps acoustic soures of noise and the thermal drift. In the design, I made an insulation box to keep the sensor temperature unchanged. However, in the real world, the insulation can only keep the temperature relatively stable not absolutely stable. The thermal drift caused by the sensor temperature change will have some effect on the output strain noise.

Very similar to the above two cases, the 1.6Hz bandwidth case is shown in figure 4.19, 4.20 and 4.21.

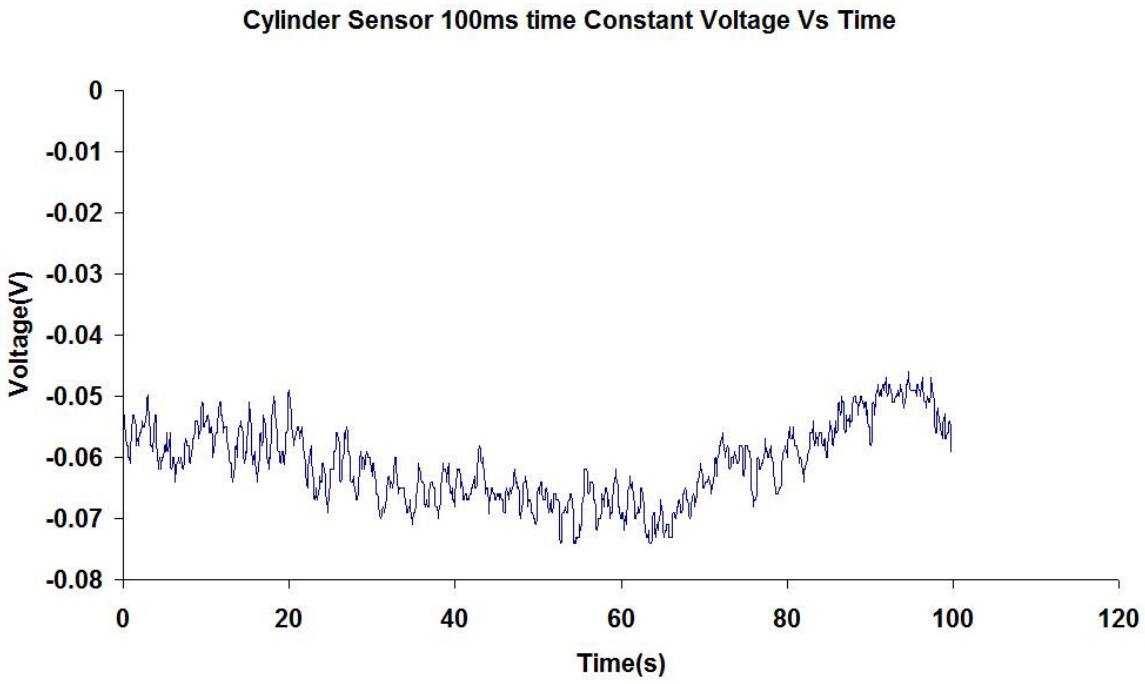

Figure 4.19 Cylinder Sensor 1.6Hz Bandwidth Noise Voltage vs Time

From figure 4.19, I see that the noise is simply Gaussian random noise with a combination of some thermal drift. Figure 4.20 shows the noise strain vs time for the 1.6Hz bandwidth case. The strain noise is also Gaussian. Figure 4.21 shows

the RMS noise for a 100s time period. The maximum RMS noise is around 11 nanostrain and the minimum RMS noise is around 6 nanostrain. The average RMS noise for this period of time is 7.88 nanostrain.

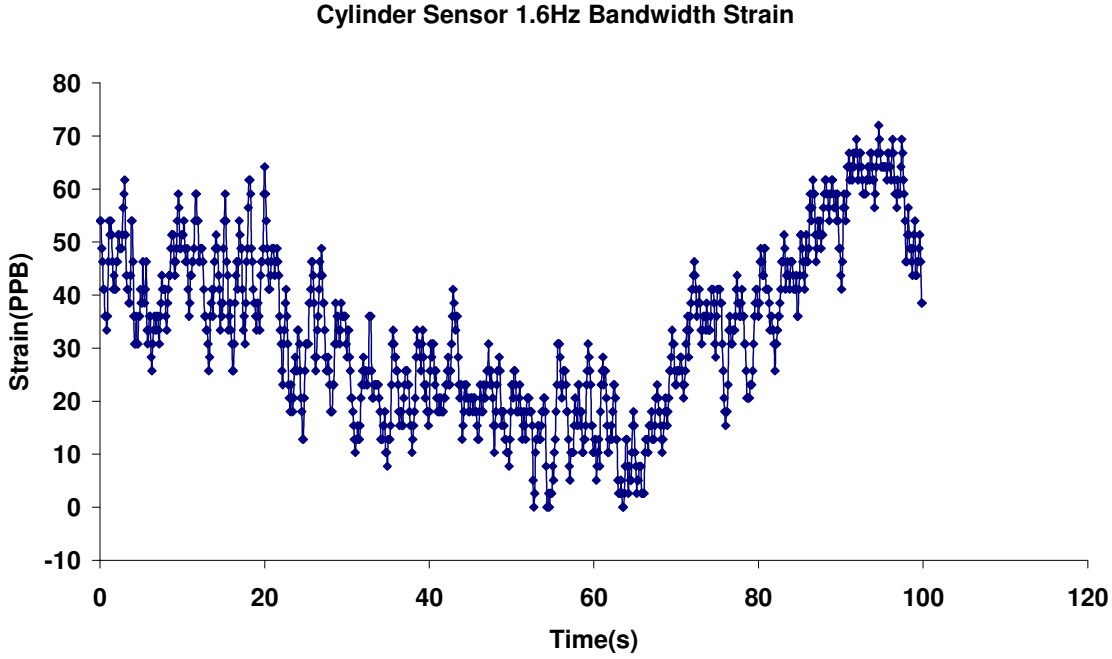

Figure 4.20 Cylinder Sensor 1.6Hz Bandwidth Noise Strain vs Time

The average RMS noise is 7.88 nanostrain, which is smaller than those of the 1ms time constant case and the 10ms time constant case. This is as expected because the time constant has increased. The value 7.88 is not exactly a factor of √10 from the 10ms time constant case. This is because the noise is not purely Gaussian. Instead, it is a combination of the Gaussian noise and other sources such as acoustic of low frequency electronic noise and the thermal drift.

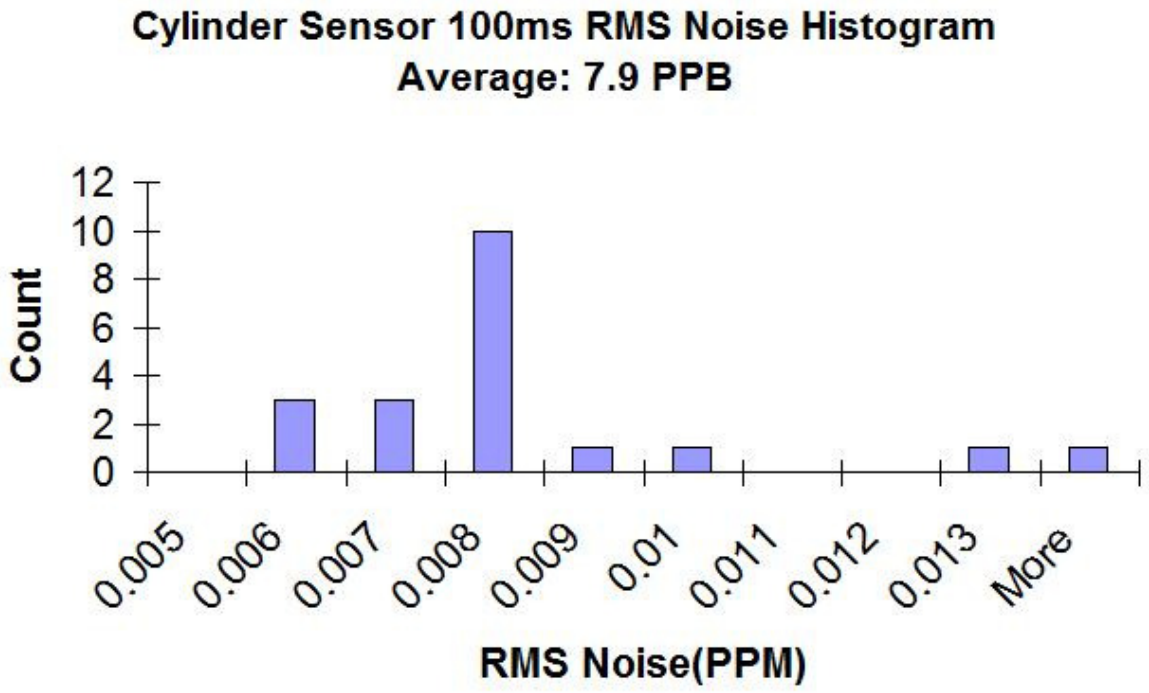

Figure 4.21 Cylinder Sensor 1.6Hz Bandwidth RMS Noise Histogram

I want to make sure the calibration and noise measurement for the cylinder sensor is correct. I did the calibration and the noise measurement again for this sensor for the second trial. The method for calibration is still the same as before and the results for the noise measurements are shown in table 4.1.

Table 4.1 Cylinder Sensor Average RMS Noise for Different Bandwidth

Bandwidth	160Hz	16Hz	1.6Hz
Average RMS Noise Strain	15.34PPB	12.85PPB	14.26PPB

I can see the results are relatively in good agreement with the one I obtained before. I have more confident in our measurement and design for the cylinder sensor case.

4.4 Testing of Diaphragm Sensor Strain on a Model Structure

I used the thermal scaling technique to do the calibration for the cylinder sensor. This same technique could be applied to the diaphragm sensor in order to get the relationship between the output voltage and the strain. In the testing, I chose to use another method to get the calibration for the diaphragm sensor, which is the strain Gauge method.

Figure 4.22 shows the structural lab strain testing setup in the McQuade Structures Laboratory at the University of Manitoba. I attached our diaphragm sensor to a steel bar using two C-clamps. Two strain gauges Ire attached to one side of the steel bar as a means of calibrating the sensor. The load frame in the laboratory is able to apply force to the bar and hence induce strain to the steel bar. Since the sensor and the strain gauges are attached to the steel bar, the strain applied to the bar will result in the same strain in the sensor. There is a magnification factor of the sensor rod. The rod has a length of a few centimetres. As the strain in the rebar changes 1 microstrain, the effect of the strain on the rod is magnified because the physical length of the rod. However, we have both the strain reading and the voltage reading and so this should not be a problem.

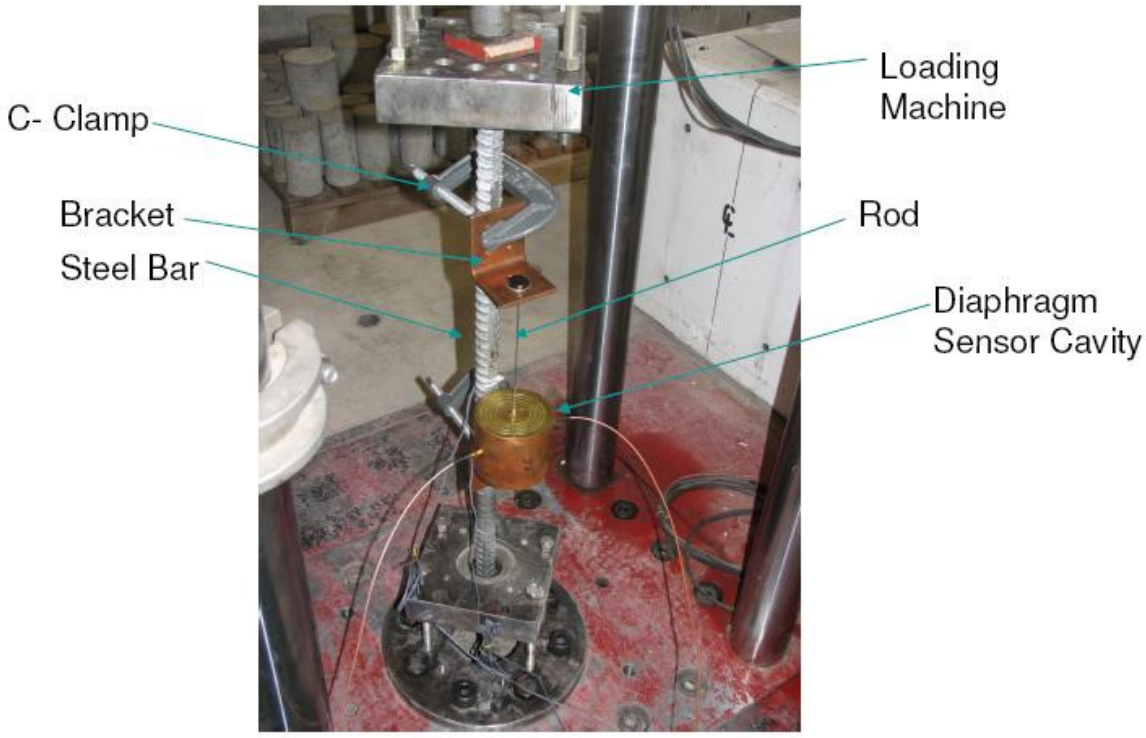

Figure 4.22 Structures Laboratory Strain Test Setup

Using our designed system, I obtained the results from our sensor cavity as a comparison to the strain gauge results.

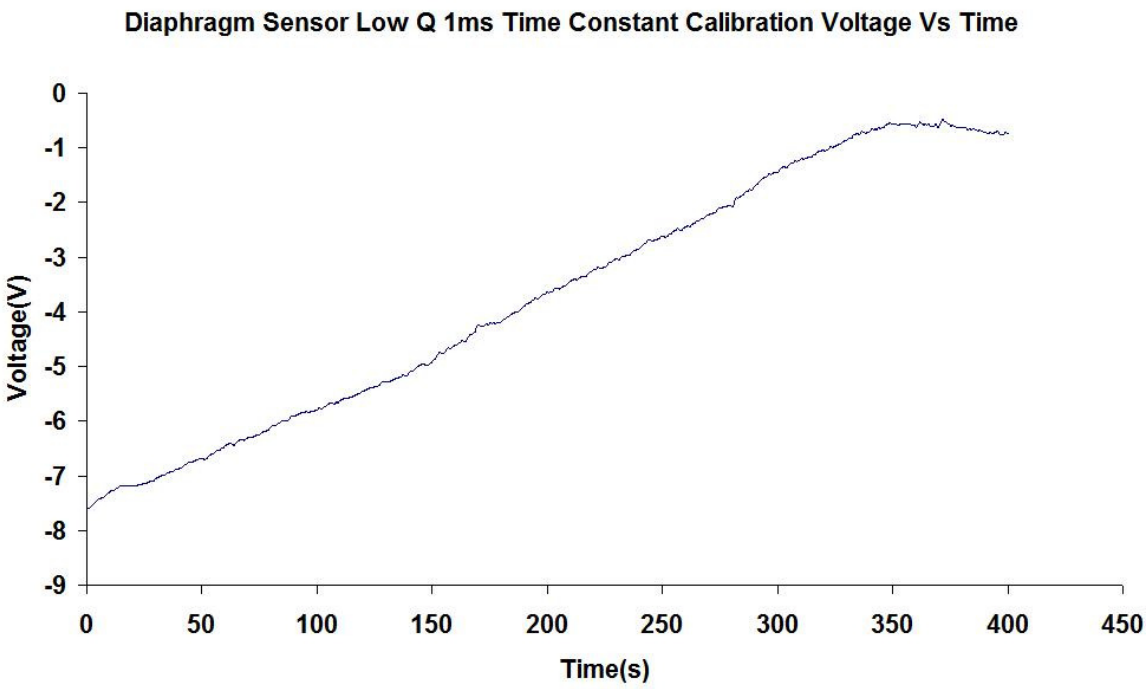

Figure 4.23 Diaphragm Sensor Low Q 1ms Time Constant Voltage vs Time

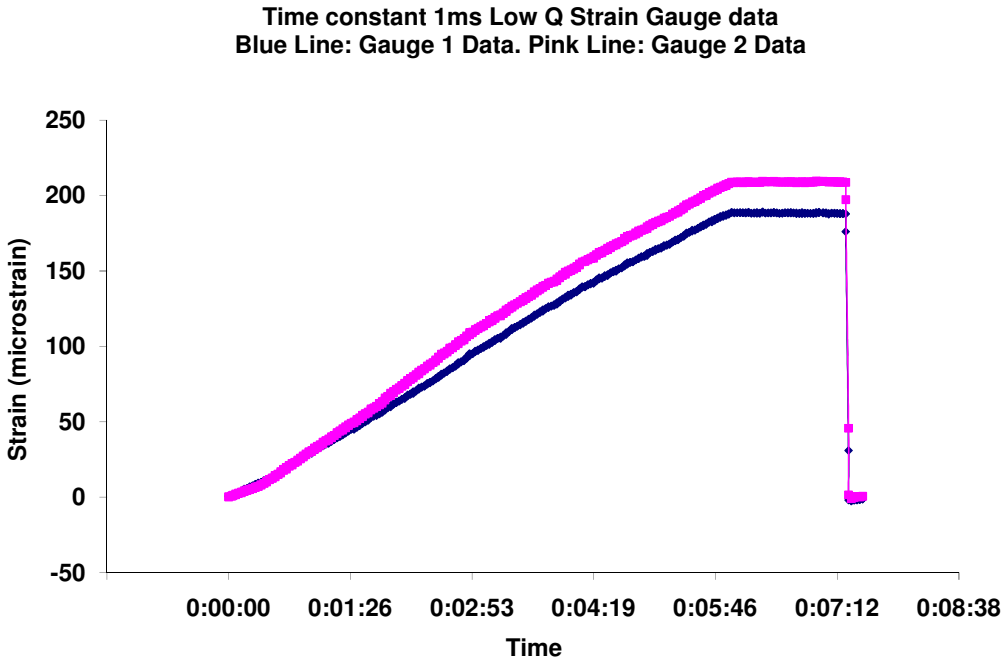

Figure 4.24 Strain Gauge Result for Low Q 1ms Time Constant Case

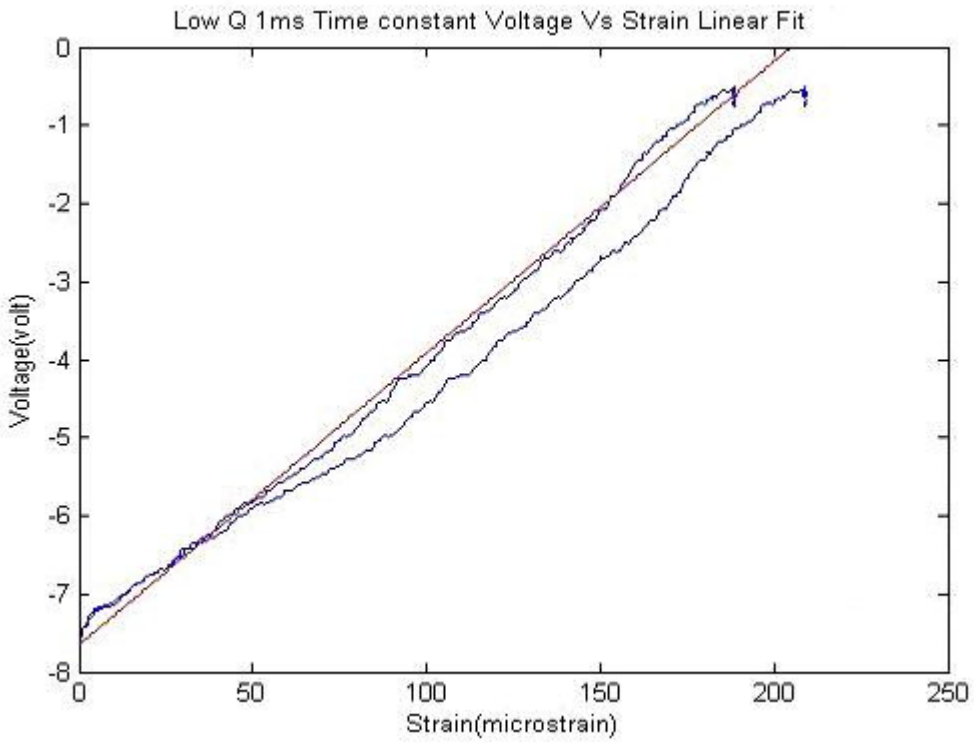

Figure 4.25 Diaphragm Sensor System Output Voltage vs Strain Linear Fit for Low Q 1ms Time Constant Case

Figure 4.23 shows the output voltage from our designed system. I applied a strain from approximately 10 to 200 microstrain and then stopped the load and reduced the strain to zero. Figure 4.24 shows the results obtained by the two strain gauges over the 400 second period. The blue line and the pink line represent the first strain gauge and second strain gauge respectively. It is obvious that the data taken from the two strain gauges are very close to each other. The maximum difference between the two is around 10 microstrain when 200 microstrain load is applied, which is a 5 percent error. Therefore, the strain gauge results are good representations of the real strain that applied to the system.

Based on the results from the two strain gauges and the data collected from the designed sensor system, I can obtain the relationship between strain and the system output voltage. Figure 4.25 shows this relationship. In addition, using MATLAB programming, I can use a linear fit of the system output voltage and the two strain gauge results. I recorded the RF sensor output voltage and the civil technician Chad recorded the strain from the electronic strain gauges. There was a delay in time for the two recordings as I start the RF sensor first then Chad started his strain gauges. The time difference is carefully considered and I made the adjustment when plotting strain vs voltage. The delay varies from case to case and has to be adjusted differently in each case. Figure 4.25 shows a general example of the delay in time.

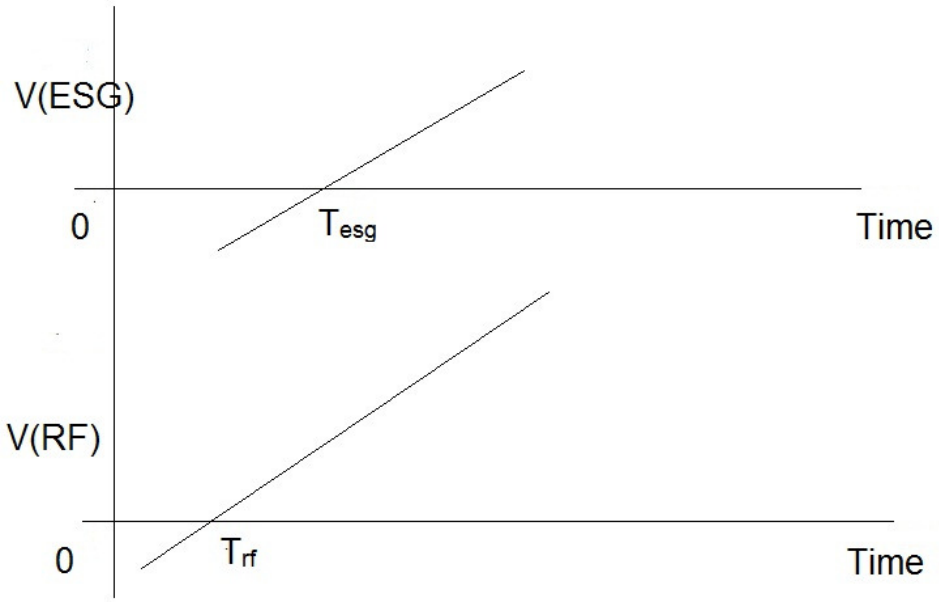

Figure 4.26 Time Delay in Diaphragm Sensor Calibration

From figure 4.25 I calculate the ratio of system output voltage to strain. The maximum voltage is 0V, and the minimum voltage is -7.583V. The strain ranges from 0 to 204 microstrain. The lock-in amplifier in this case is set to be 500μV, which is already the standard sensitivity and does not need to be adjusted. The relationship between the output voltage and the strain is given by

$$\frac{0-(-7.583)}{204-0} = 0.037 \, {}^{V}\!/_{\mu\varepsilon}$$

Similarly, I obtained the strain gauge results and system output voltage for the other cases. The following figures and calculations show the relationship between voltage and strain for the other cases.

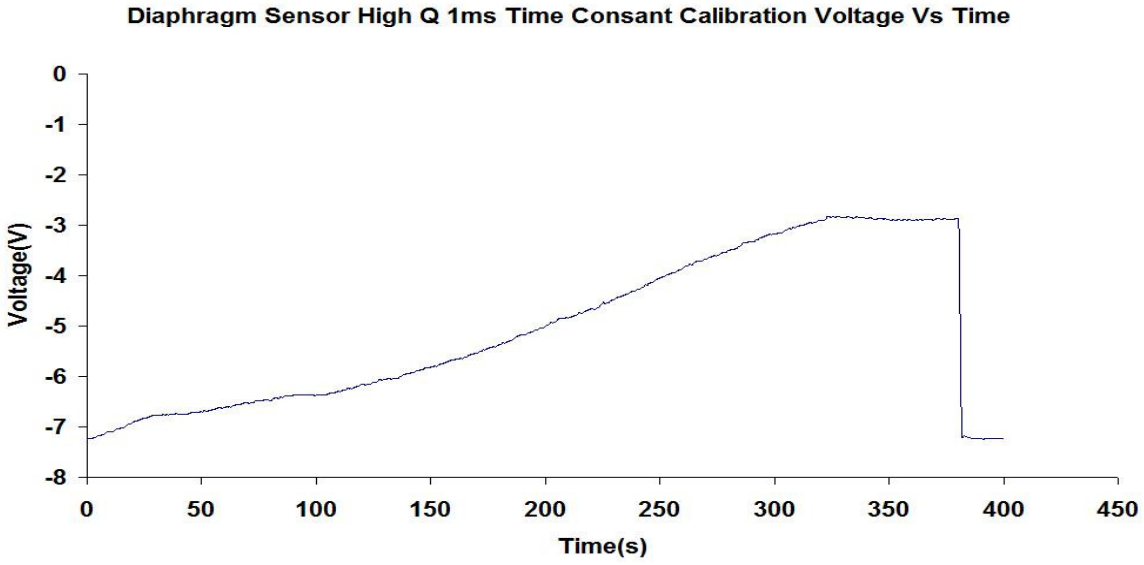

Figure 4.27 Diaphragm Sensor High Q 1ms Time Constant Voltage vs Time

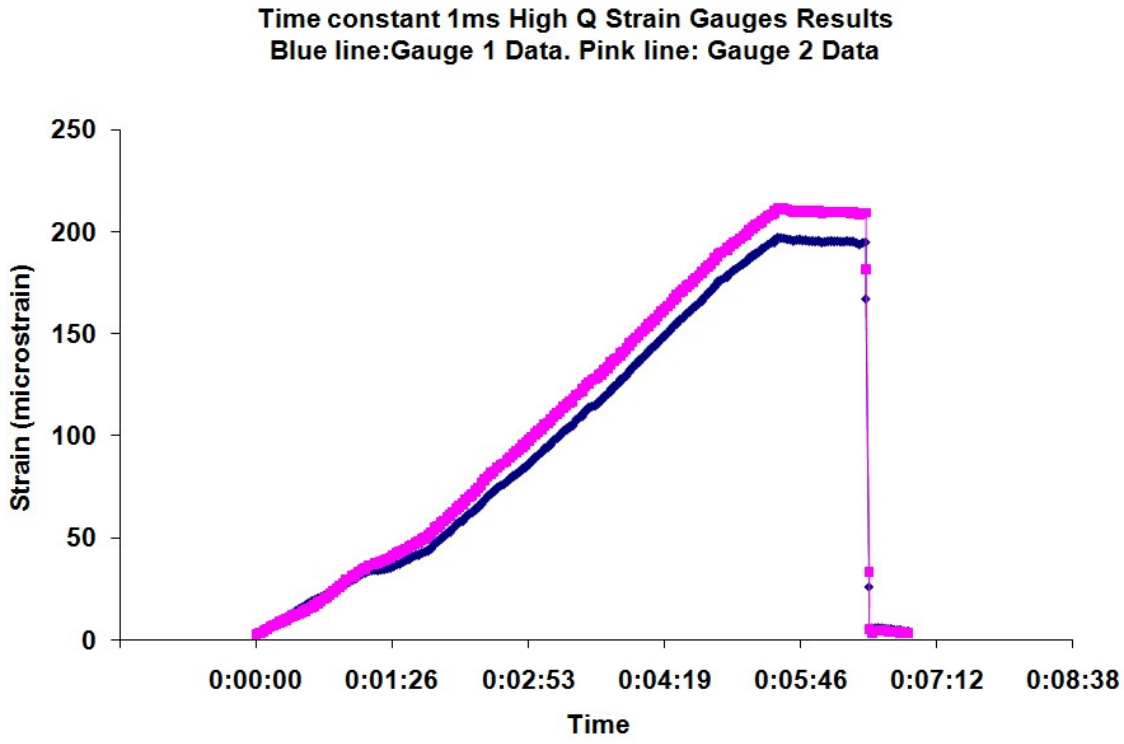

Figure 4.28 Strain Gauge Result for High Q 1ms Time Constant Case

Figure 4.27 shows the output voltage obtained from our designed system for the High Q 1ms case. Figure 4.28 shows the results obtained from the strain gauges for the same case.

I mentioned in Chapter 2 that the Lock-in Amplifier sensitivity is significant to the output value. I need to make the LIA sensitivity the same for all the measurements. However, in the structure lab test, I did not use the same scale for clarity purpose. Therefore, I need to make some adjustments in the calculation. For the high Q 1ms time constant case, I chose the sensitivity to be 1mV. For consistency, I set the sensitivity to be 500μV as the standard for all the

calculation. Therefore, for the high Q 1ms time constant case, I need to adjust the voltage by 1mV / 500μV = 2. The relationship between the output voltage and the strain for the high Q 1ms time constant is given by

$$\frac{-1.714-7.375}{250-0}\times 2 = 0.045 \, {}^{V}\!/_{\mu\varepsilon}$$

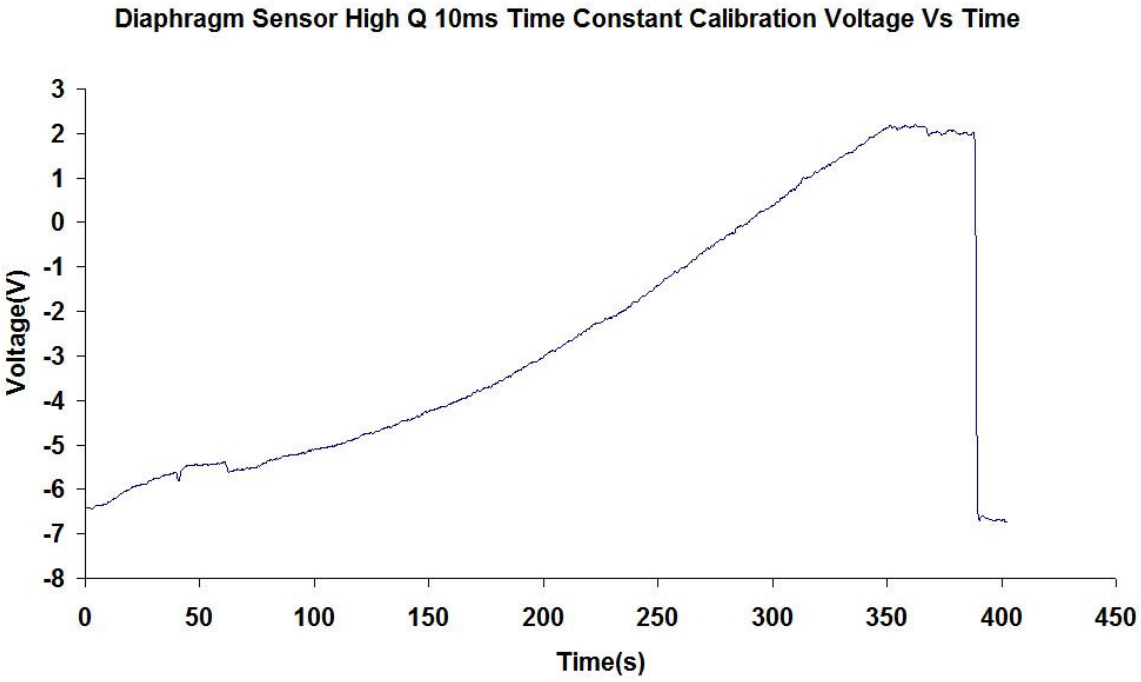

Figure 4.29 Diaphragm Sensor High Q 10ms Time Constant Voltage vs Time

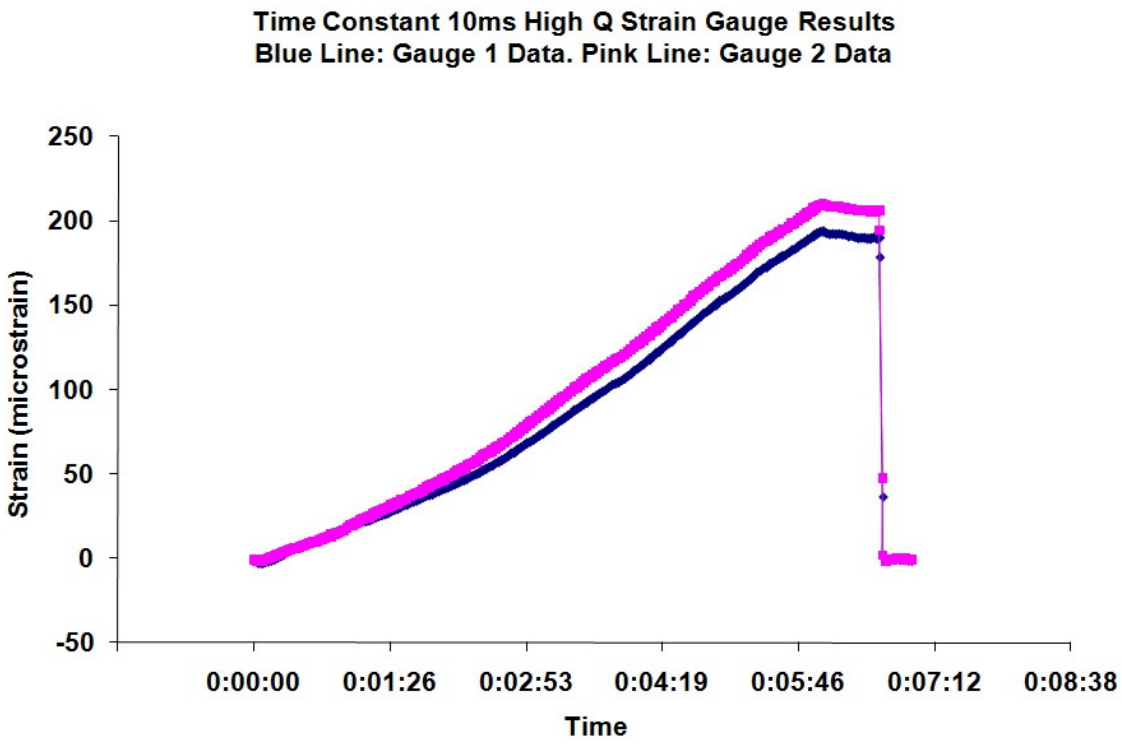

Figure 4.30 Strain Gauge Result for High Q 10ms Time Constant Case

Figure 4.29 shows the output voltage obtained from the diaphragm sensor system for the high Q 10ms case. Figure 4.30 shows the results obtained from the strain gauges for the same case. The lock-in amplifier in this case is set to be 500μV, which is already the standard sensitivity and does not need to be adjusted. The relationship between the output voltage and the strain is given by

$$\frac{3-(-7)}{216.67-(-7.14)} = 0.045 \, {}^{V}\!/_{\mu\varepsilon}$$

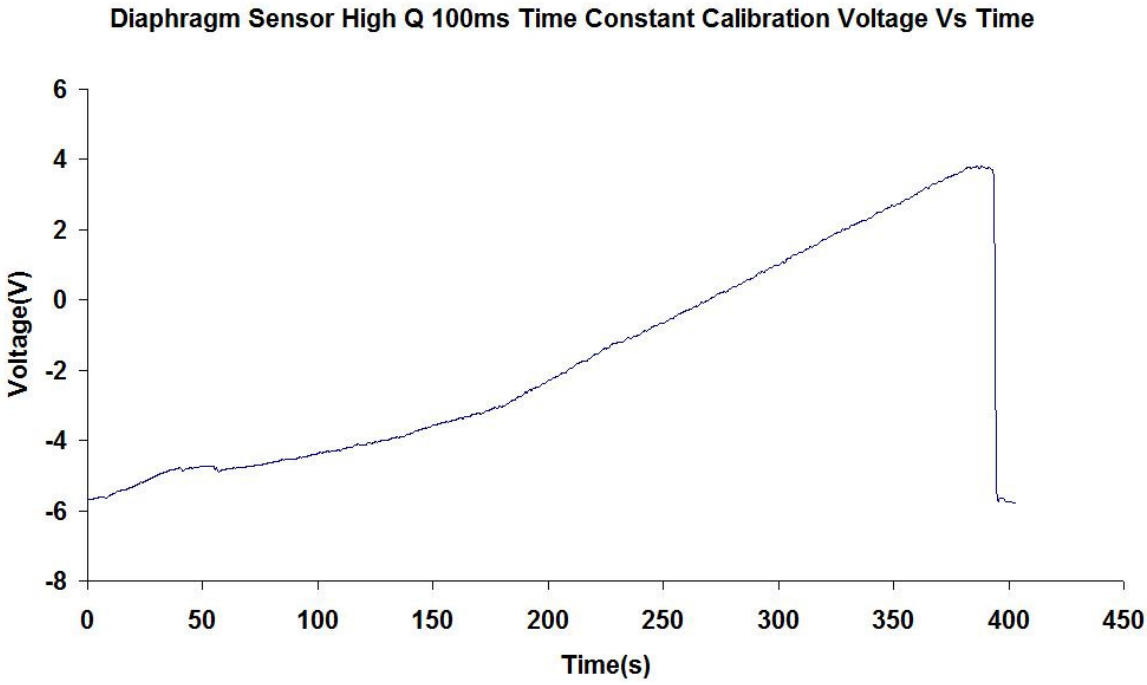

Figure 4.31Diaphragm Sensor High Q 100ms Time Constant Voltage vs Time

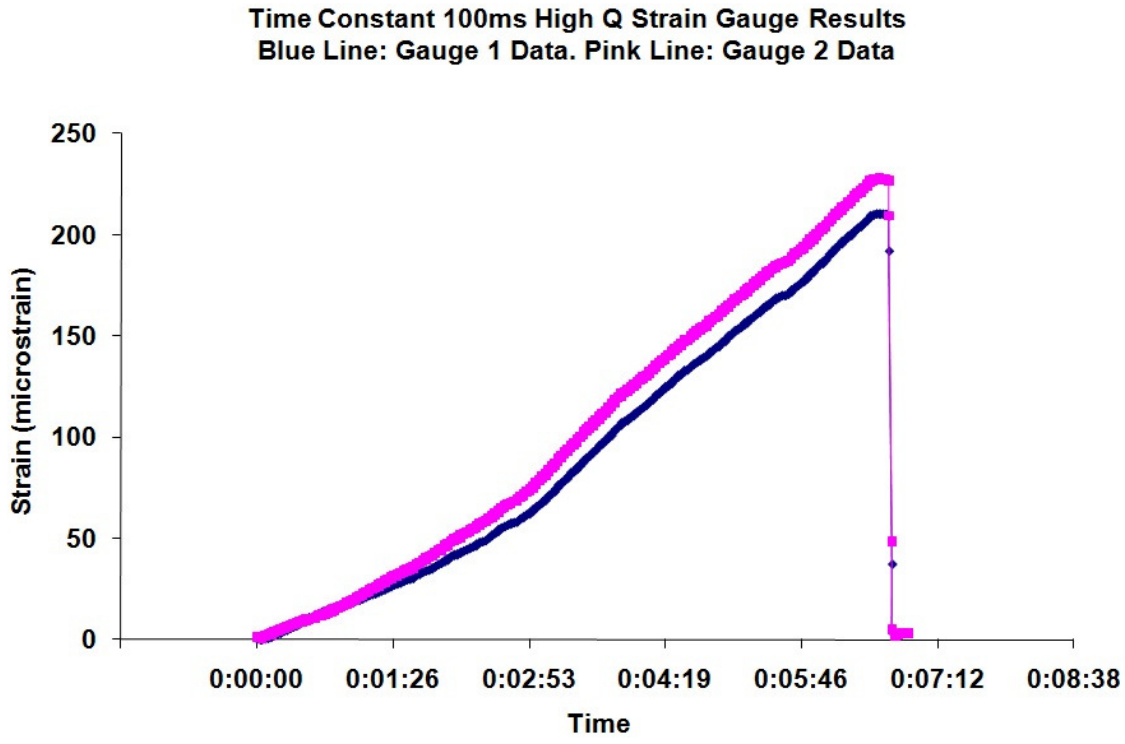

Figure 4.32 Strain Gauge Result for High Q 100ms Time Constant Case

Figure 4.31 shows the output voltage obtained from our designed system for the high Q 100ms case. Figure 4.32 shows the results obtained from the strain gauges for the same case. The lock-in amplifier in this case is set to be 500μV, which is already the standard sensitivity and does not need to be adjusted. The relationship between the output voltage and the strain is given by

$$\frac{3-(-5.9)}{220-0} = 0.045 \, V/\mu\varepsilon$$

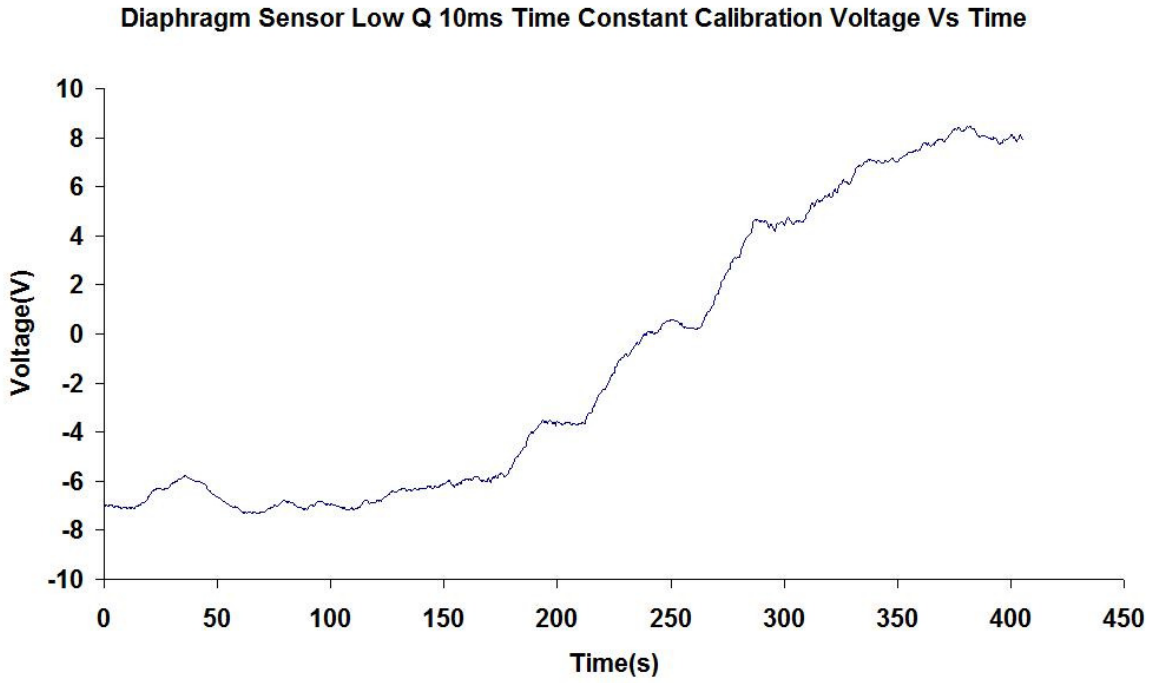

Figure 4.33 Diaphragm Sensor Low Q 10ms Time Constant Voltage vs Time

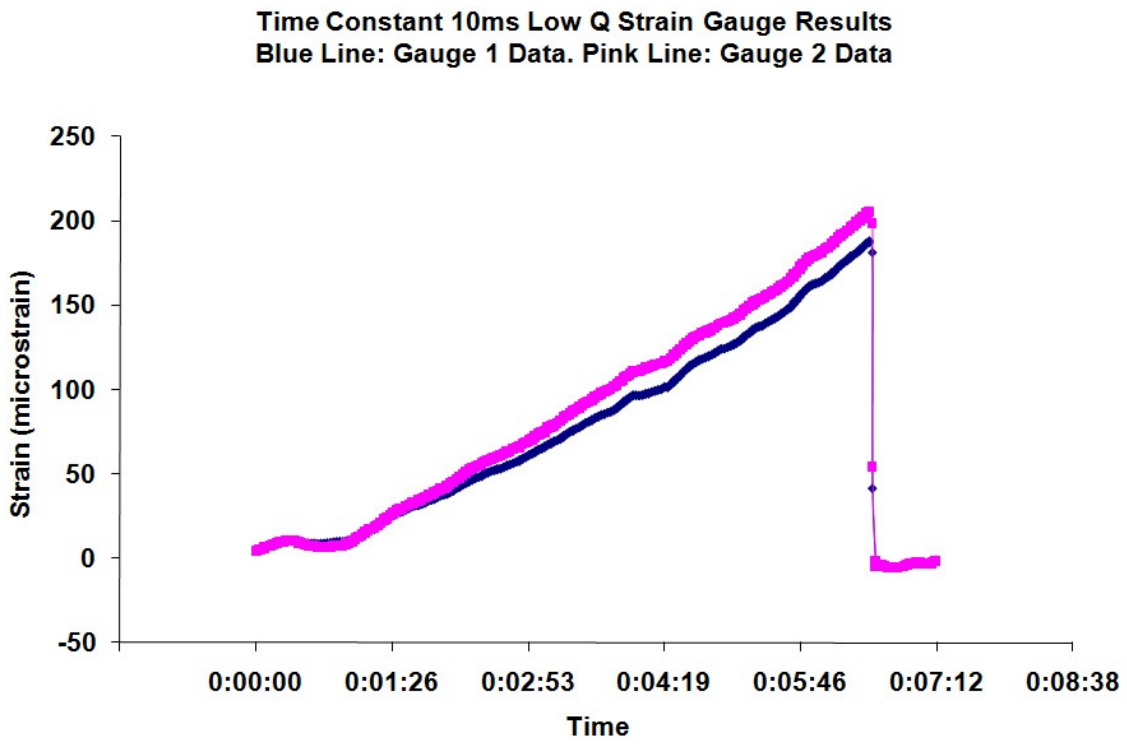

Figure 4.34 Strain Gauge Result for Low Q 10ms Time Constant Case

Figure 4.33 shows the output voltage obtained from our designed system for the Low Q 10ms case. Figure 4.34 shows the results obtained from the strain gauges for the same case. The lock-in amplifier in this case is set to be 200μV. I need to adjust the voltage output by 200 / 500 = 1 / 2.5. The relationship between the output voltage and the strain is given by

$$\frac{15-1.5}{2.5\times(187.5-0)} = 0.043 \, V/\mu\varepsilon$$

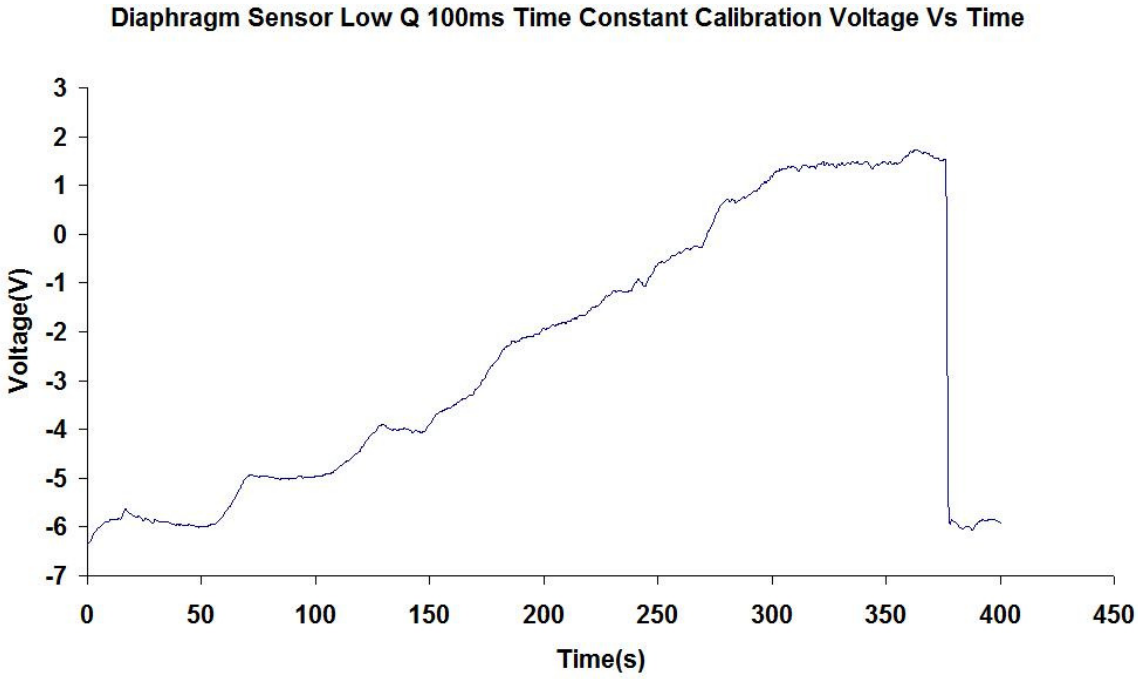

Figure 4.35 Diaphragm Sensor Low Q 100ms Time Constant Voltage vs Time

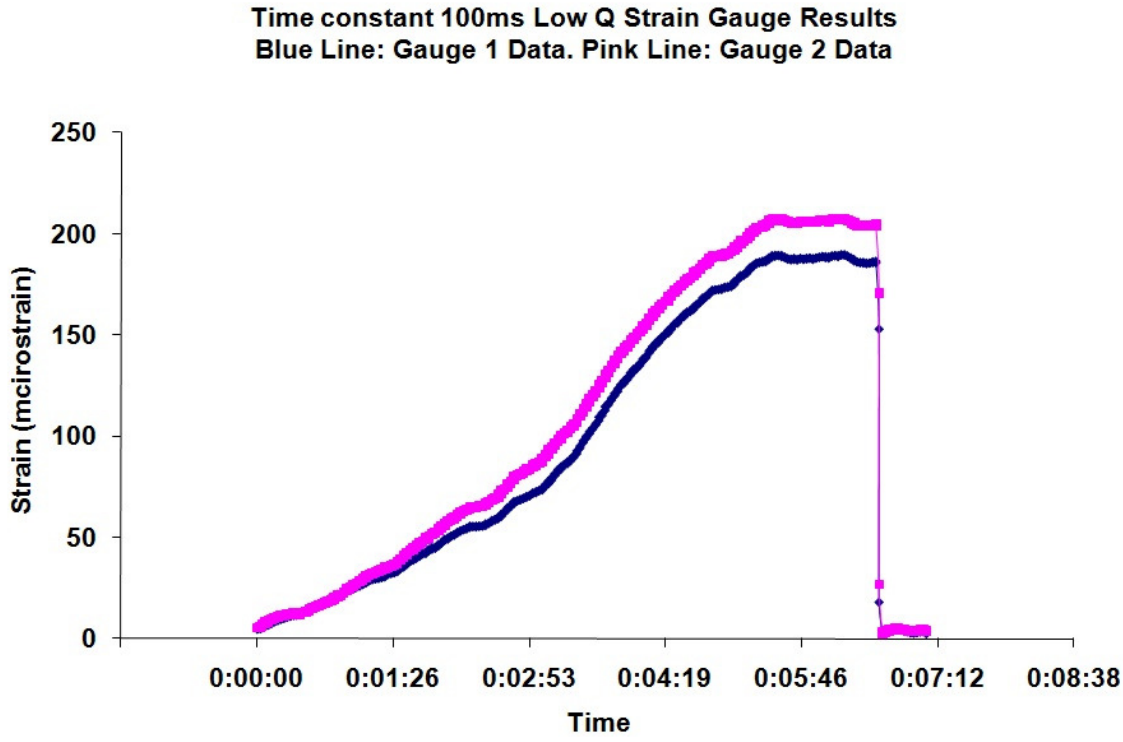

Figure 4.36 Strain Gauge Result for Low Q 100ms Time Constant Case

Figure 4.35 shows the output voltage obtained from our designed system for the Low Q 100ms case. Figure 4.36 shows the results obtained from the strain gauges for the same case. The lock-in amplifier in this case is set to be 500μV, which is already the standard sensitivity and does not need to be adjusted. The relationship between the output voltage and the strain is given by

$$\frac{2-(-6.364)}{212-0} = 0.039 \, V/\mu\varepsilon$$

4.5 Diaphragm Sensor Noise for High Q Condition

In the lab, I put the diaphragm sensor into a cardboard box with a Styrofoam insulation layer in the middle. I turned on the system for a 400 seconds period of time and measured the noise coming out of the system. I recorded the system output voltage using the oscilloscope the same way as I did for the cylinder sensor.

Based on the values obtained from the above calculation, I can get the diaphragm sensor noise for both the high Q and low Q conditions. Figure 4.37 shows the diaphragm sensor high Q 1ms time constant noise strain vs time.

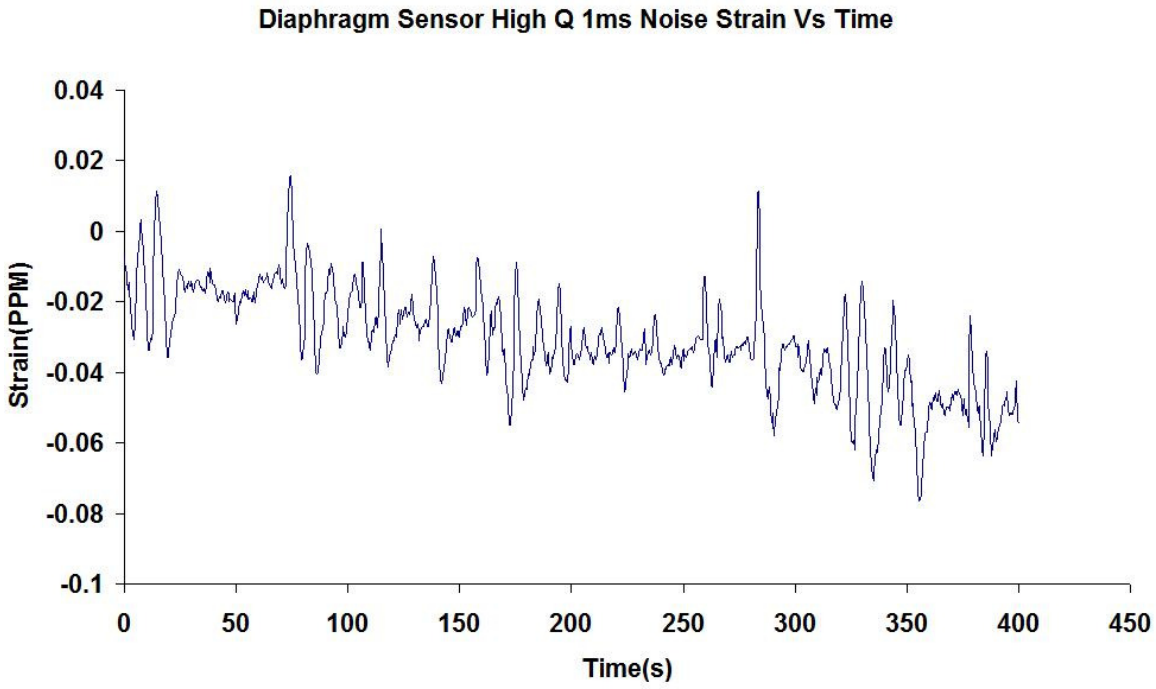

Figure 4.37 Diaphragm Sensor High Q 1ms Time Constant Noise Strain vs Time

From Figure 4.37, it is easy to see that the noise contains random Gaussian Noise with a combination of thermal drift and some quasiperiodic noise. The thermal drift is due to the effect of the ambient temperature on the sensor temperature. Also, the ambient acoustic noise can be picked up by the diaphragm and cause some noise in measurement. Perhaps acoustic noise could account for the quasiperiodic noise. To reduce the acoustic vibration, I put a Styrofoam board underneath the insulated box, and this reduced the noise significantly.

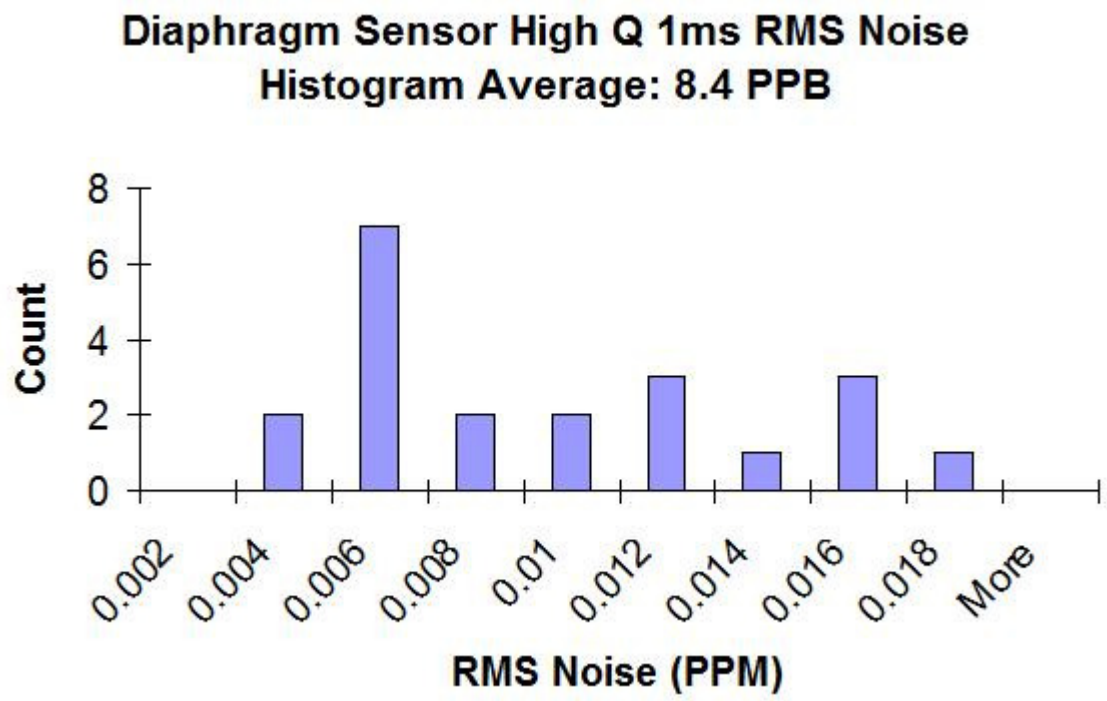

Figure 4.38 Diaphragm Sensor High Q 1ms Time Constant RMS Noise Histogram

Figure 4.38 shows the diaphragm sensor high Q 1ms time constant RMS noise. I took a measure for a period of 400 seconds. I then divided the 400 seconds into 10 samples, and each sample has a time period of 20 seconds. Using MATLAB programming, I can calculate the RMS noise for each sample. All the calculated sample RMS noise for high Q 1ms time constant case were shown in Figure 4.42 above. The maximum RMS noise is around 17 nanostrain and the minimum RMS noise for this case is around 2 nanostrain. The average RMS noise for this 400 time period is around 8.4 nanostrain.

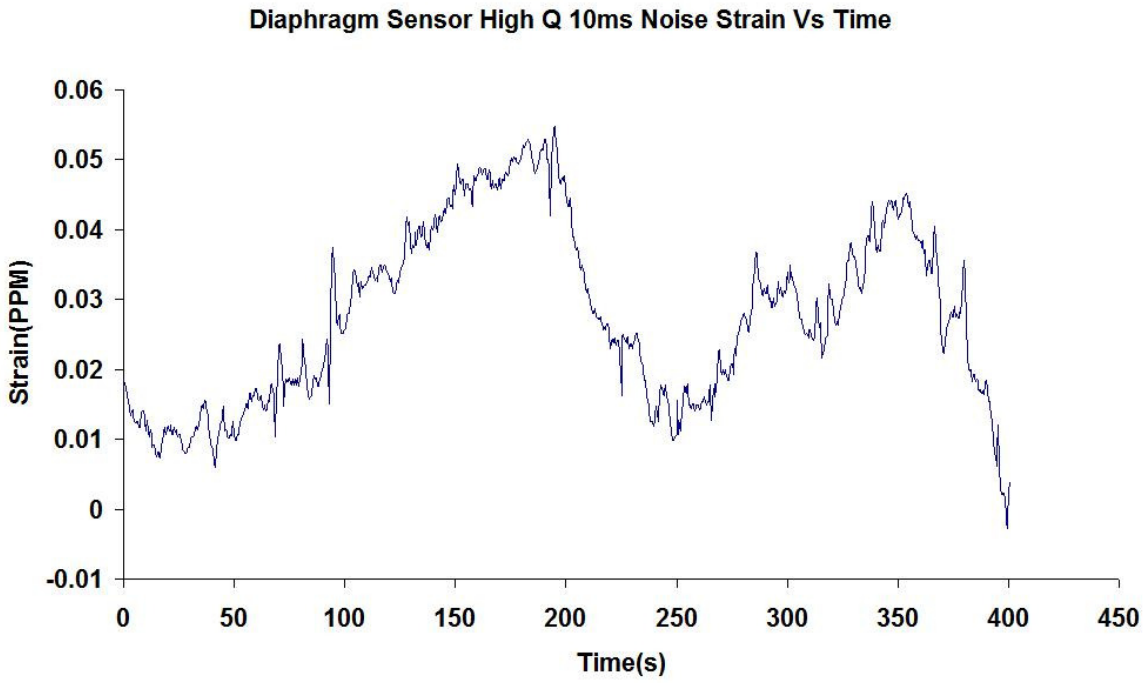

Figure 4.39 Diaphragm Sensor High Q 10ms Time Constant Noise

Figure 4.39 shows the diaphragm sensor high Q 10ms time constant noise strain vs time. This plot is obtained the same way as the 1ms time constant case. The noise contains random Gaussian noise with a combination of some thermal drift and perhaps some quasiperiodic noise. The reason for the drift is the same as in the 1ms time constant case.

Figure 4.40 shows the diaphragm sensor high Q 10ms time constant RMS noise. Similar to the 1ms time constant case, the RMS noise for each 20s sample is calculated by MATLAB programming. The maximum RMS noise is around 8 nanostrain and the minimum RMS noise is around 1 nanostrain. The average RMS noise for the 400 time period is around 3.51 nanostrain.

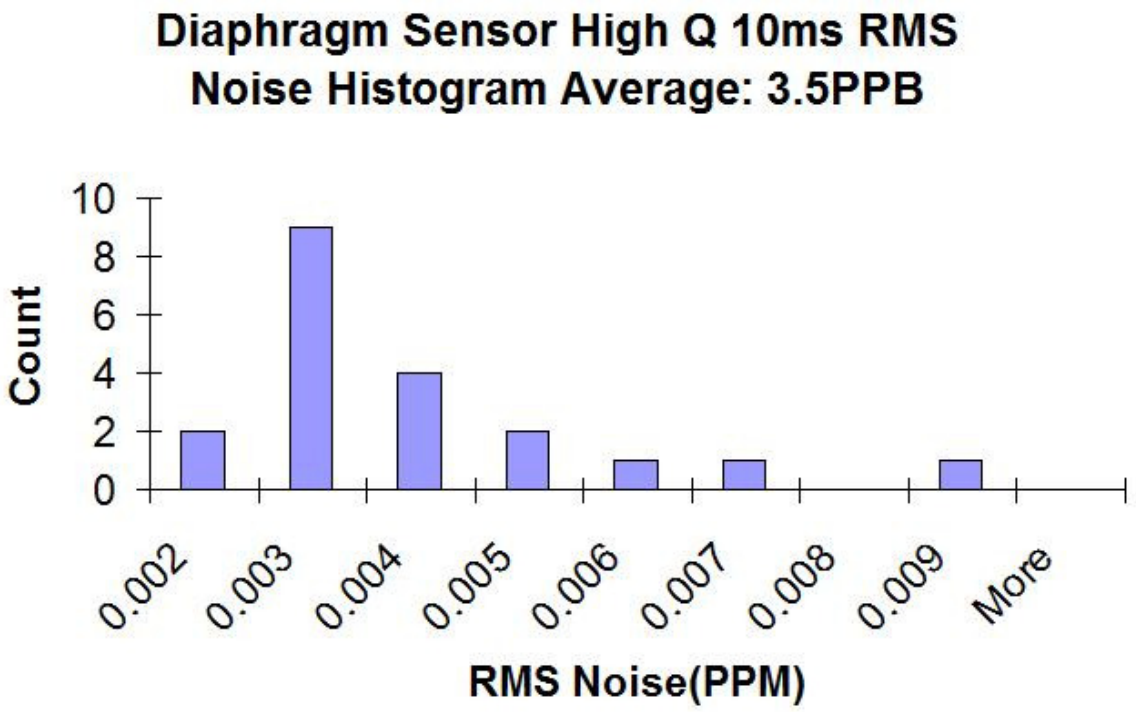

Figure 4.40 Diaphragm Sensor High Q 10ms Time Constant RMS Noise Histogram

The average RMS noise for the 10ms time constant case is smaller than that of the 1ms time constant case. This is as expected. The reason for that is shown in Chapter 3. I also explained this in the cylinder sensor noise section. When the time constant becomes 10 times larger, the bandwidth of the system will be 10 times smaller. Theoretically, the thermal noise will be 10 times smaller and this will result in the strain variation reducing by a factor of 10. In our lab measurement, I found that the strain noise is reduced from 8.4 to 3.5. However, this is not by a factor of 10. The reason is that the noise is not simply Gaussian noise but also some thermal drift and acoustic vibration has been involved in this case.

Similarly, the strain noise versus time and the RMS noise for the high Q 100ms time constant case is shown in figure 4.41 and 4.42 respectively.

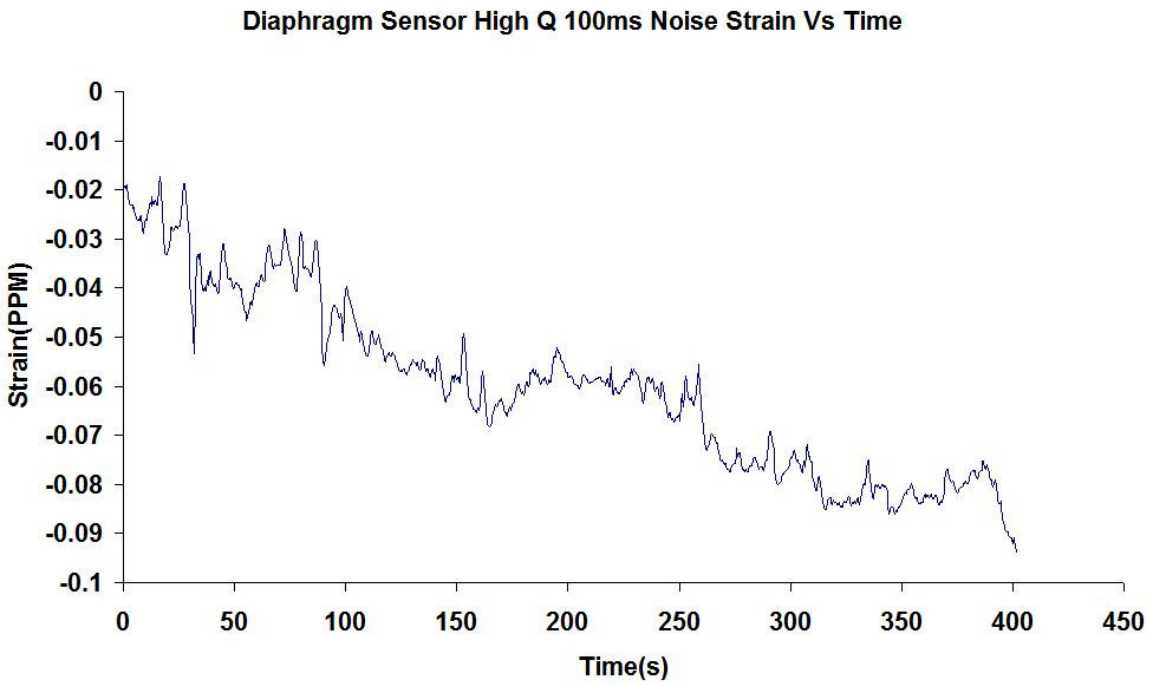

Figure 4.41 Diaphragm Sensor High Q 100ms Time Constant Noise

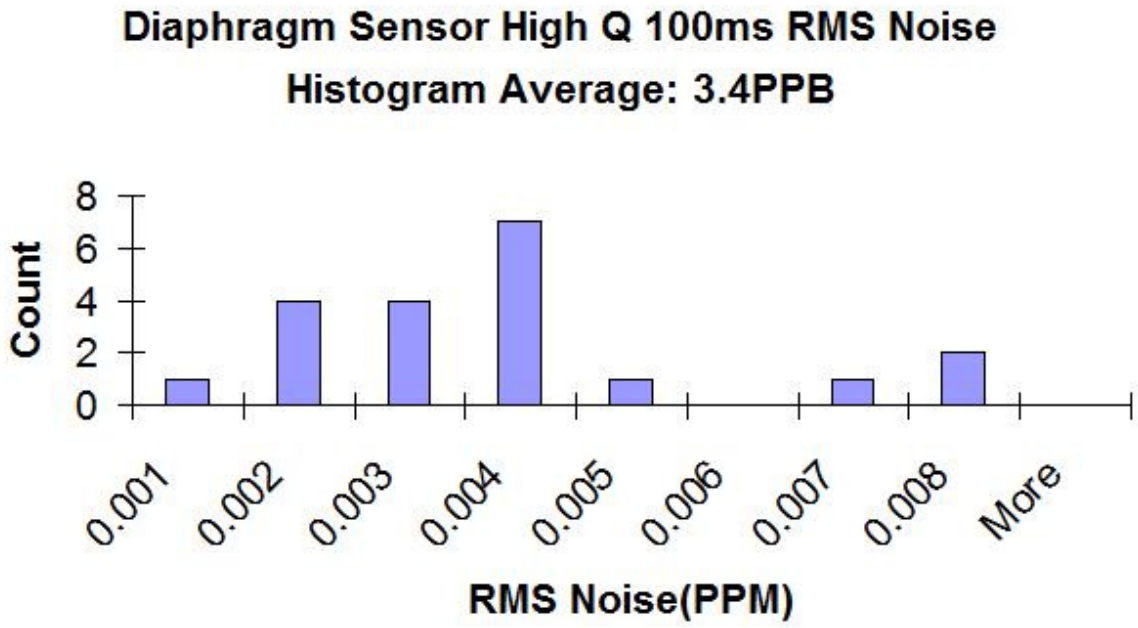

Figure 4.42 Diaphragm Sensor High Q 100ms Time Constant RMS Noise Histogram

4.6 Diaphragm Sensor Noise for Low Q Condition

The strain noise and RMS noise for the diaphragm sensor low Q condition is shown in this section. I have the same test setup as for the high Q condition. To switch the conditions from high Q to low Q, I simply adjust the resonant frequency on the signal generator from 2445.9MHz to 2433.9MHz and adjust the phase shifter to make the original phase to be zero. The three different cases for 1ms, 10ms and 100ms time constant are shown below.

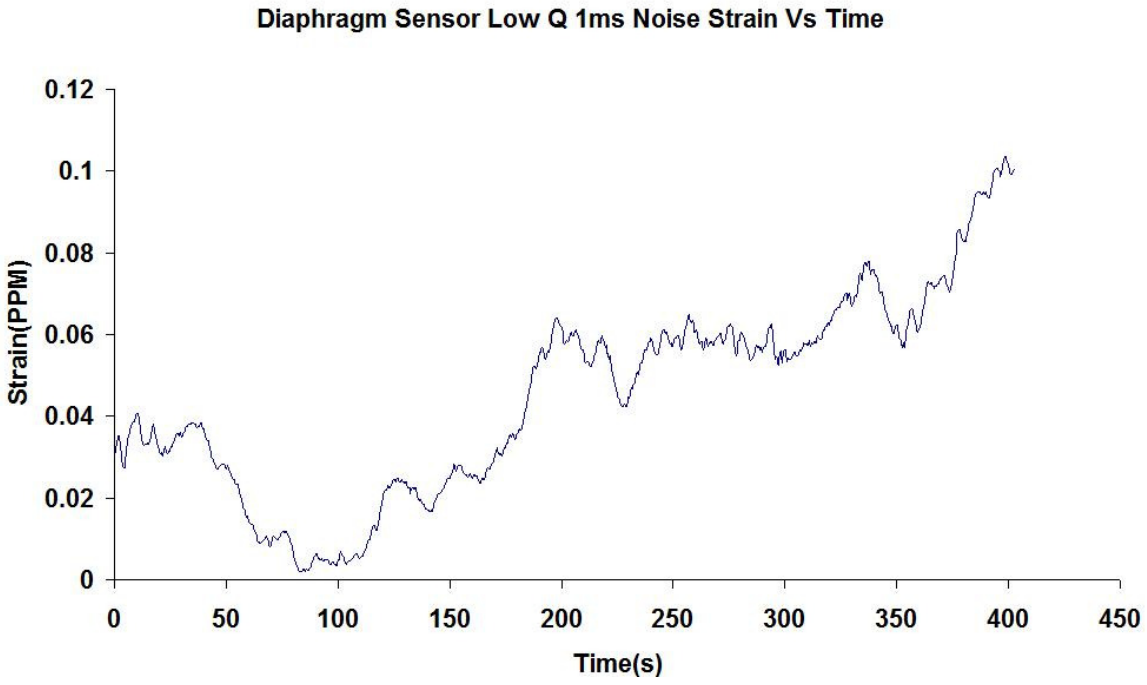

Figure 4.43 Diaphragm Sensor Low Q 1ms Time Constant Noise

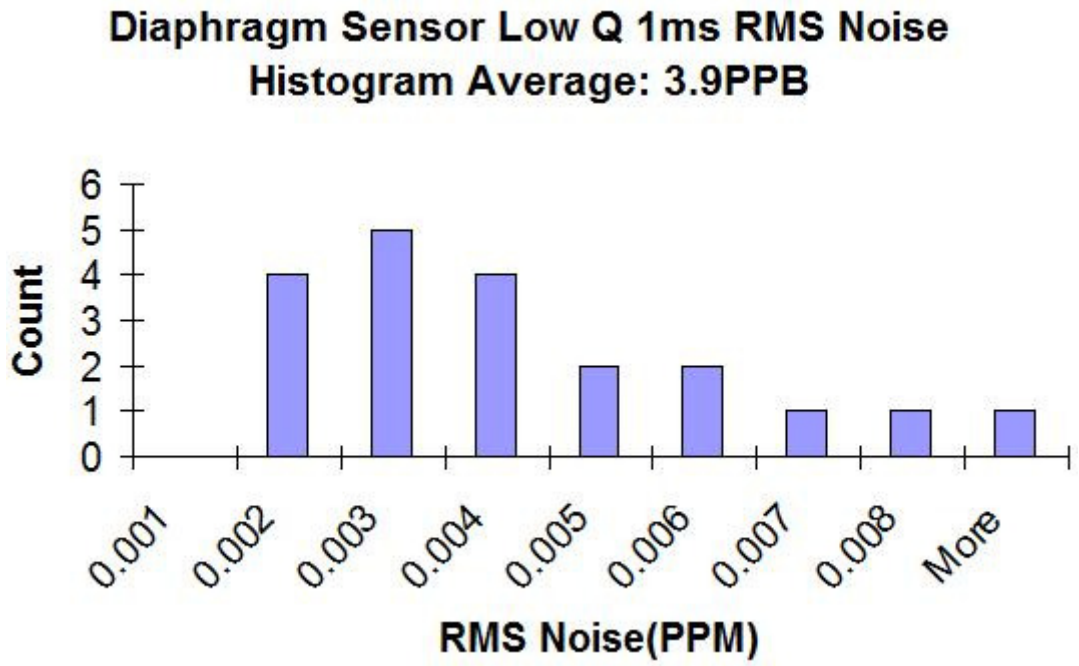

Figure 4.44 Diaphragm Sensor Low Q 1ms Time Constant RMS Noise Histogram

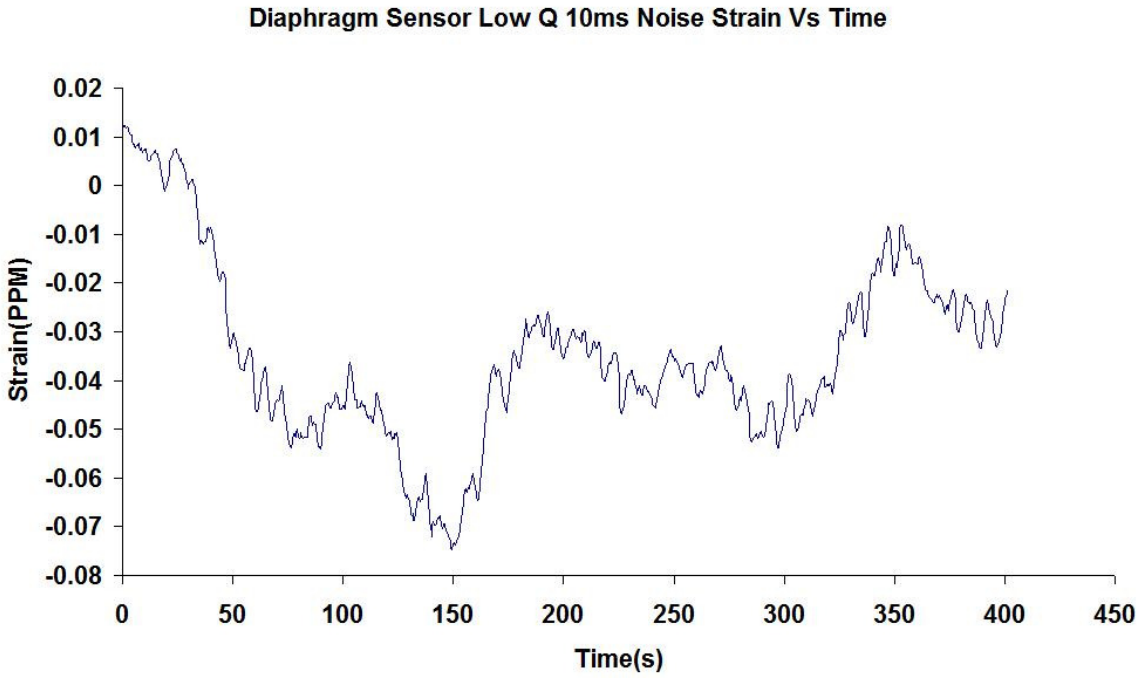

Figure 4.45 Diaphragm Sensor Low Q 10ms Time Constant Noise

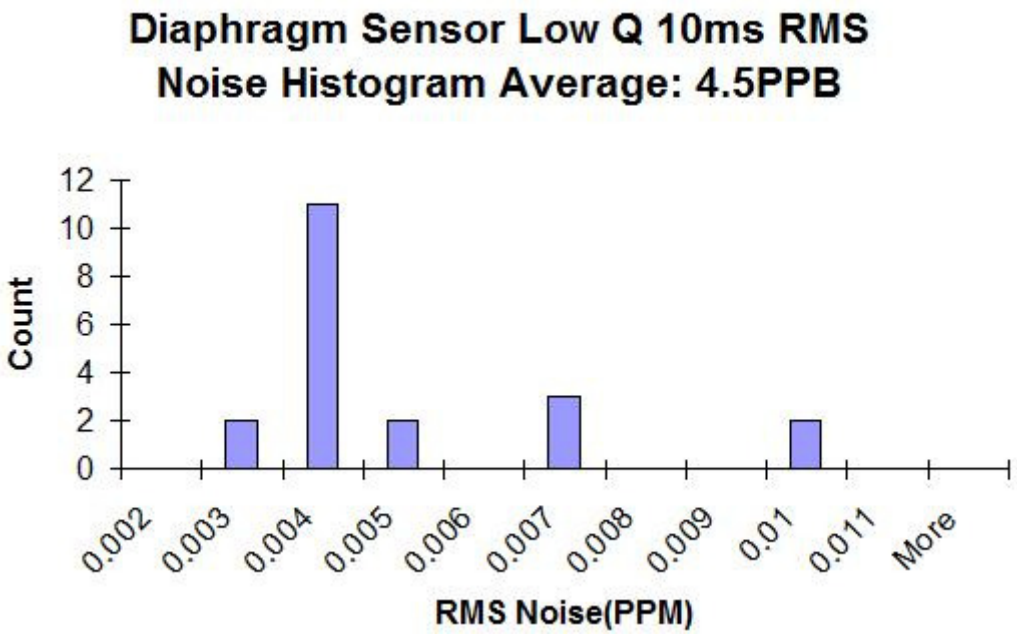

Figure 4.46 Diaphragm Sensor Low Q 10ms Time Constant RMS Noise Histogram

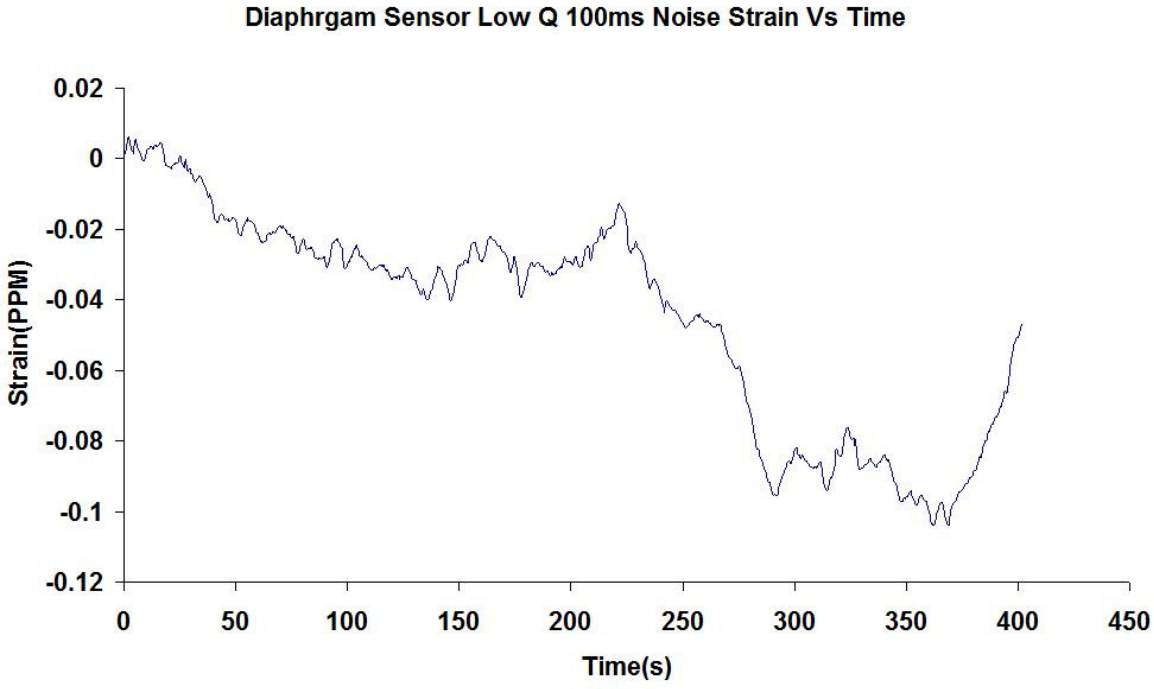

Figure 4.47 Diaphragm Sensor Low Q 100ms Time Constant Noise

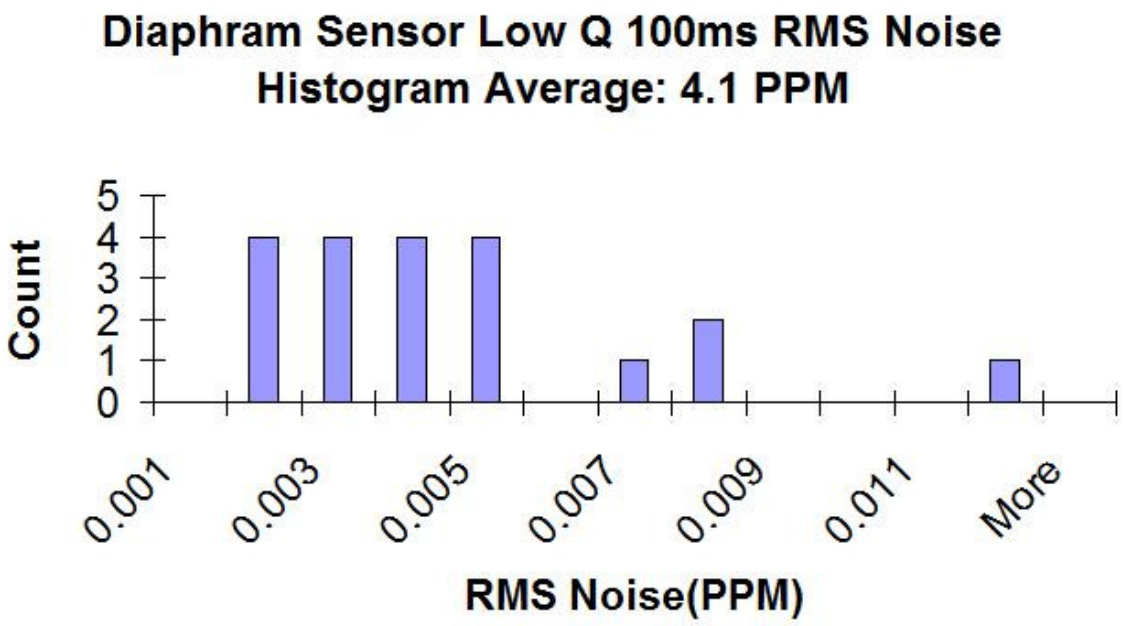

Figure 4.48 Diaphragm Sensor Low Q 100ms Time Constant RMS Noise Histogram

Based on the data from the cylinder sensor noise and the diaphragm sensor noise high Q and low Q conditions, I can make a table to summarize these data.

Table 4.2 Sensor (6dB attenuator) Average RMS Noise Summary

Time Constant / Sensor Type	160Hz	16Hz	1.6Hz
Cylinder Sensor	25 PPB	11 PPB	8 PPB
Diaphragm Low Q	4 PPB	5 PPB	4 PPB
Diaphragm High Q	8 PPB	4 PPB	3 PPB
Cylinder Theory	1.2 PPB	0.4 PPB	0.1 PPB
High Q Theory	0.6 PPB	0.2 PPB	0.1 PPB
Low Q Theory	5 PPB	1.6 PPB	0.5 PPB

4.7 Diaphragm Sensor Calibration Using Differential Micrometer

I did calibration for the diaphragm sensor in Structures laboratory and I obtained the relationship between the strain and system output voltage. I want to make sure the calibration is correct and to verify this I did another calibration for the diaphragm sensor in our laboratory within the Electrical and Computer Engineering (ECE) Department.

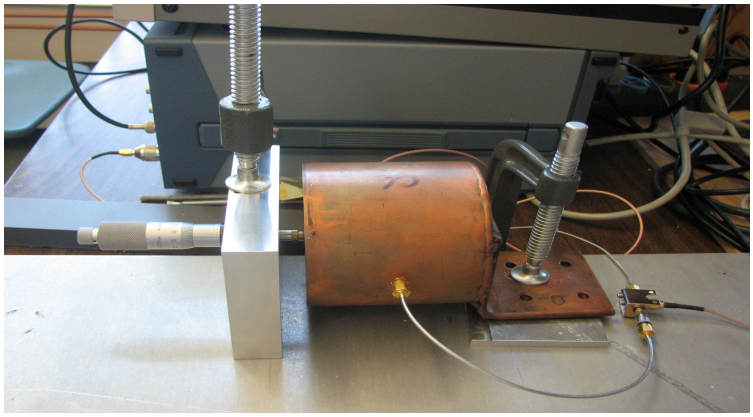

Figure 4.49 Diaphragm Sensor Calibration

As shown in figure 4.49, I used a differential micrometer and C clamps to do the calibration. The center of the micrometer is levelled with the center of the diaphragm. The diaphragm is pushed in to a certain distance when I turn the micrometer. I can measure the actual distance by reading the micrometer and get the system voltage output from the lock-in amplifier. In the high Q condition test, I turned the micrometer from 0 μm to 10 μm and took 10 readings from the lock-in amplifier. I did the test twice for both the high Q and the low Q conditions.

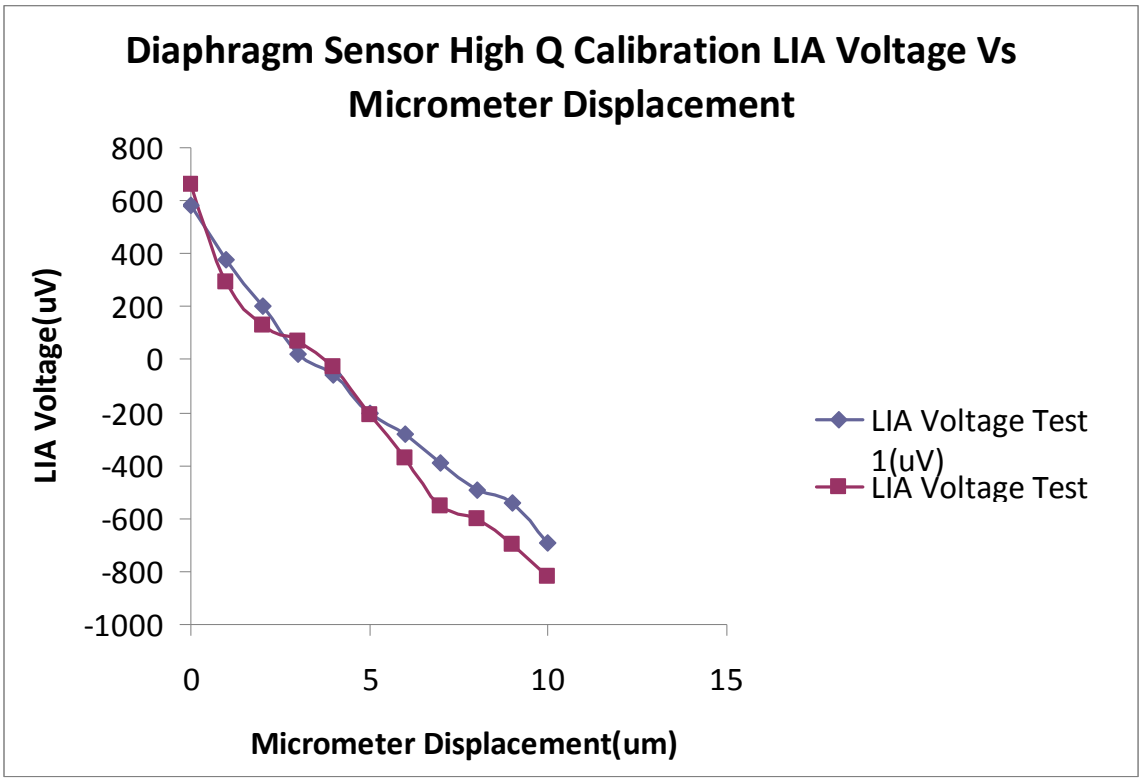

Figure 4.50 Diaphragm Sensor High Q Calibration LIA Voltage vs Displacement

I obtained the Voltage-to-Displacement Ratio for the high Q condition.

$$V/D = (610 - (-700)) \div 10 = 131V/\mu m$$

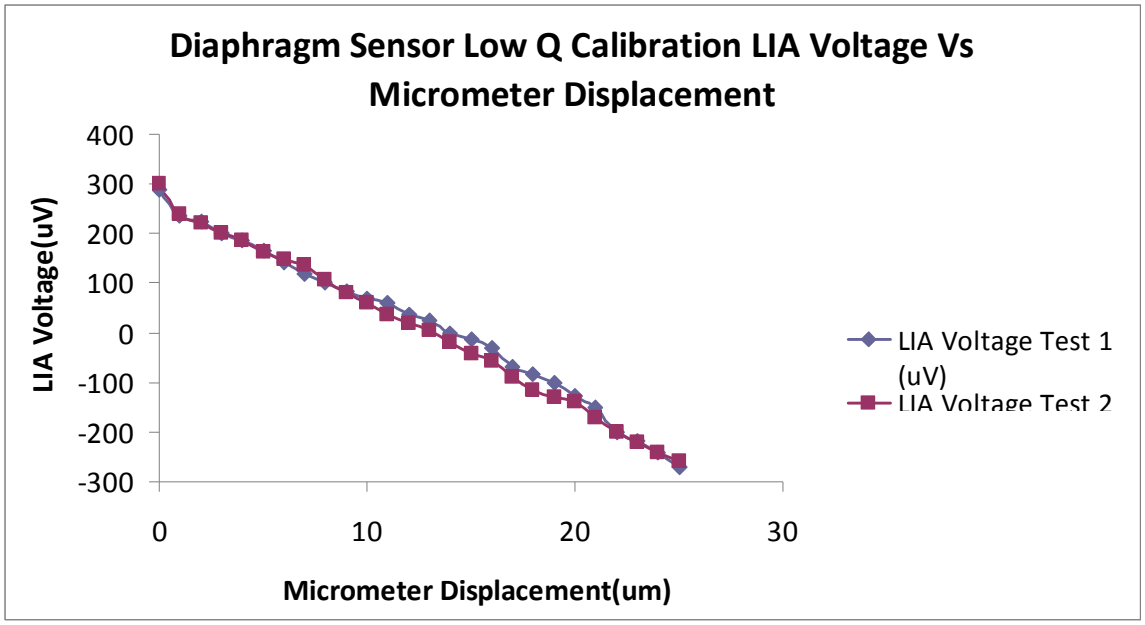

Figure 4.51 Diaphragm Sensor Low Q Calibration LIA Voltage vs Displacement

I also obtained the Voltage-to-Displacement Ratio for the low Q condition.

$$V/D = (300 - (-280)) \div 25 = 23.2V/\mu m$$

4.8 Diaphragm Sensor Noise Measurement Using New Calibration Setup

I measured the noise for the diaphragm sensor again in the ECE lab. The test equipments and environment are the same as before. I already know the voltage-to-displacement ratio and I measured the diaphragm sensor length which is 9cm. Therefore 1µm is equal to 1µm / 9cm = 11.1 PPM. The relationship between strain and voltage is given by

$$Strain = Voltage \div 10V \times 500\mu V \div (131V/\mu m \div 11.1PPM)$$

In the equation above, I multiplied 10V by 500μV. 500μV is the lock-in amplifier sensitivity.

Using this equation I obtained the strain noise for both high Q and low Q conditions for 1ms, 10ms, and 100ms time constant.

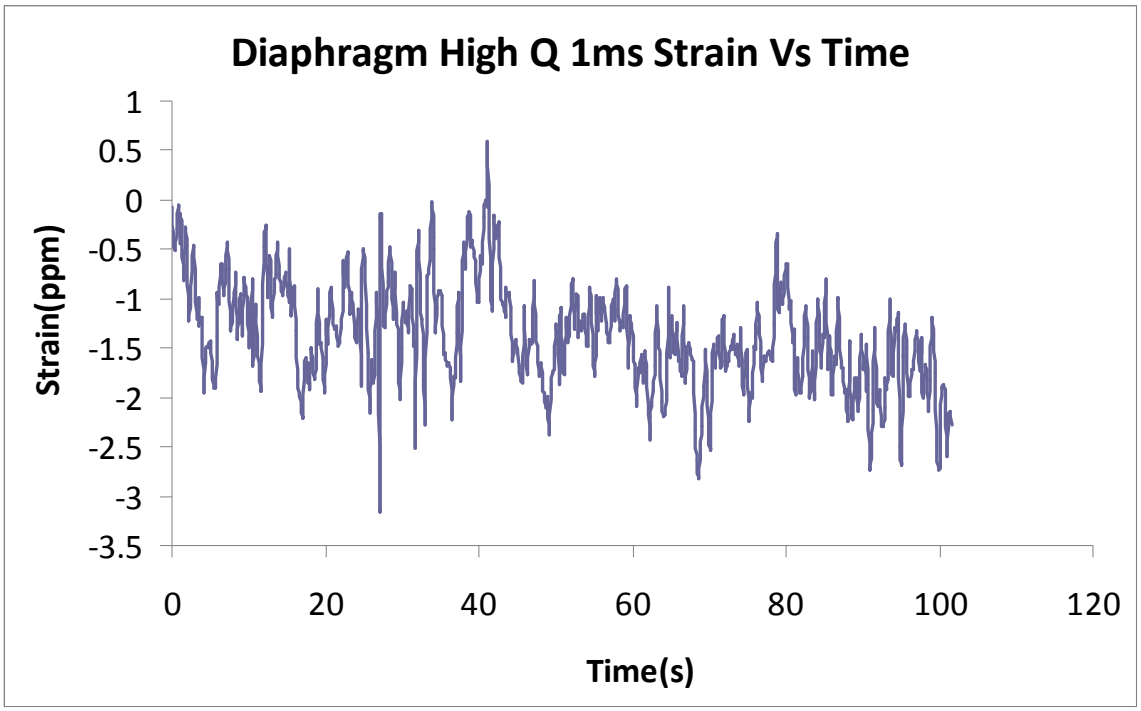

Figure 4.52 Diaphragm Sensor High Q 1ms Strain vs Time

I divided the 100s period into 20 divisions, and each division is 5s long in time. I calculated the average RMS noise for the high Q 1ms time constant case, which is 415.7 nanostrain. The noise is fairly large. In fact, the noises for all the cases are fairly large this time.

5. Chapter V Structures Lab Dynamic Test

A test of the sensor was carried out on a model bridge deck. The civil engineering group was doing bridge deck testing in the McQuade Structures laboratory. They used hydraulic actuators to apply a periodic load to the bridge deck continuously. The machine was programmed to move up and down in a sinusoidal pattern, so the load on the deck is sinusoidal. We believed this would be a good opportunity to test our sensor in a dynamic manner.

Figure 5.1 Bridge Deck Test Loading System

I mounted the diaphragm sensor to the bridge girder using C-clamps. The sinusoidal loading will result in a strain change on the girder which can be measured using our sensor. I also mounted a traditional strain gauge to the girder. I glued the strain gauge to the girder at the mid-point location of the

diaphragm sensor rod. I use the strain gauge as a comparison to our sensor to do the calibration.

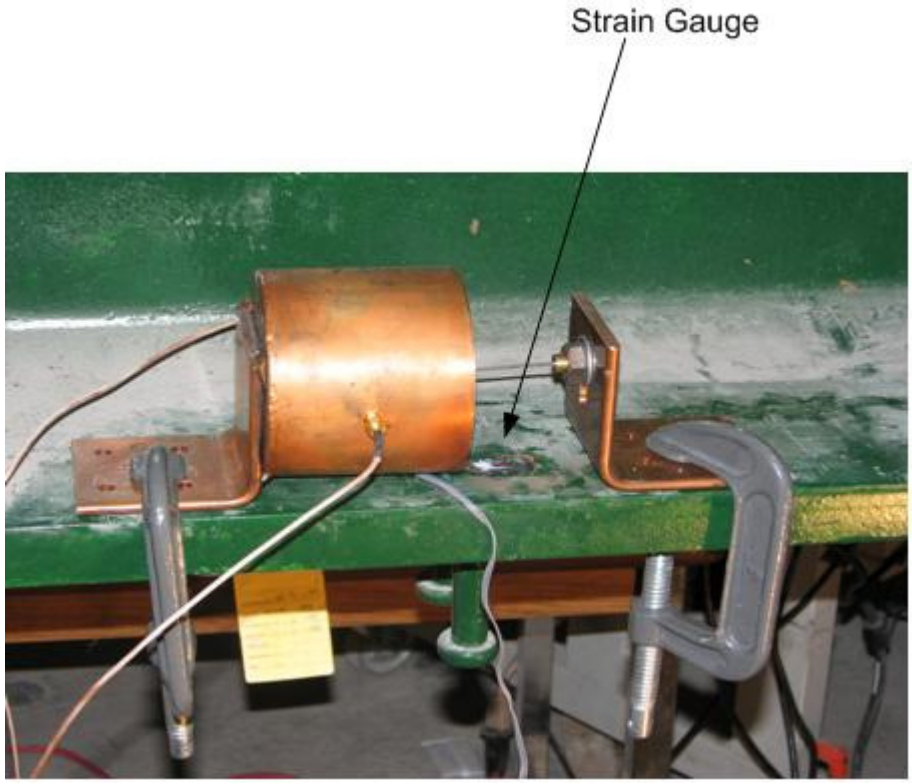

Figure 5.2 Diaphragm Sensor Mounted on the Bridge Girder

Figure 5.1 shows the mechanical loading system and figure 5.2 shows the diaphragm sensor being installed on the bridge girder. I did the dynamic test for both the low Q and high Q conditions.

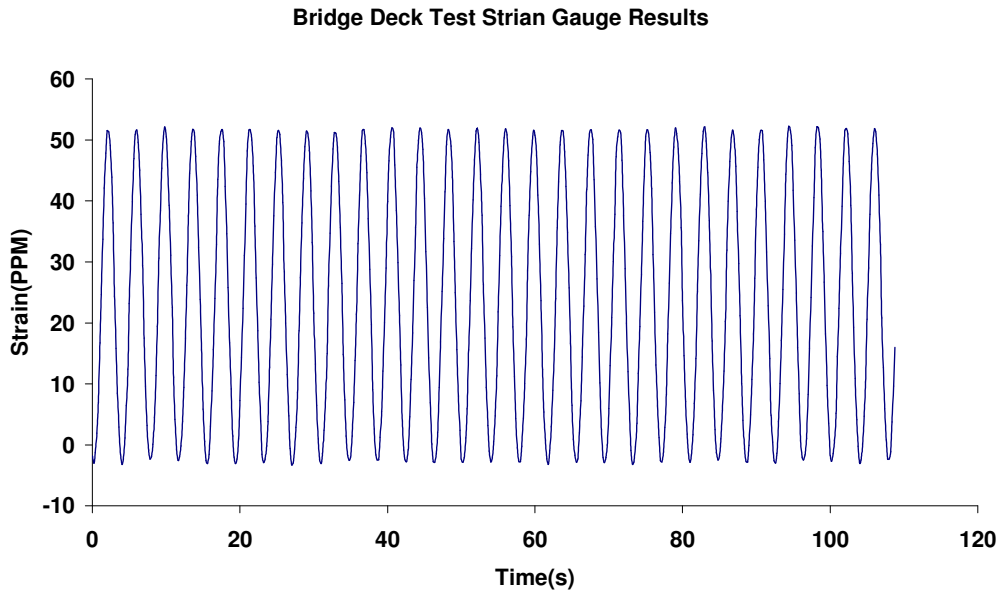

Figure 5.3 Bridge Deck Test Electronic Strain Gauge Results Strain vs Time

Figure 5.3 shows the electronic strain gauge results. I can see from the plot that the strain on the girder changes periodically in a sinusoidal pattern and it ranges from 0 to 50 microstrain.

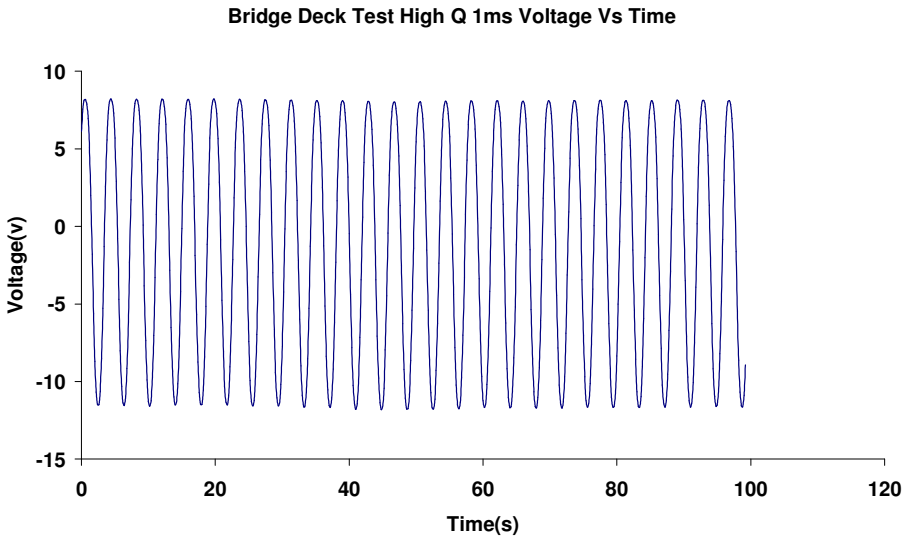

Figure 5.4 Bridge Deck Test High Q 1ms Voltage vs Time

Figure 5.4 shows the voltage vs time for high Q condition 1ms time constant case. The voltage has the same pattern as the strain gauge result which is sinusoidal. The voltage ranges from -12V to 8V. I can use the electronic strain gauge data to do the calibration. The strain ranges from 0 to 50 PPM and the voltage ranges from -12 to 8 V. The ratio between strain and voltage is $\frac{50-0}{8-(-12)} = 2.5PPM/V$.

If I apply the calibration by using the differential micrometer method, I can calculate the strain change over a 100s time period. The strain change is sinusoidal and ranges from -200 microstrain to 150 microstrain. This result is not consistent with the one I obtained from the strain gauge. The reason is that the calibration using the differential micrometer involves some errors due to mechanical configurations such as connections and diaphragm deformation. The voltage and strain plots for the high Q condition 10ms and 100ms time constant cases are very similar to the one I just showed above. They have the sinusoidal pattern which is as expected but the strain value is not matching the strain gauge results.

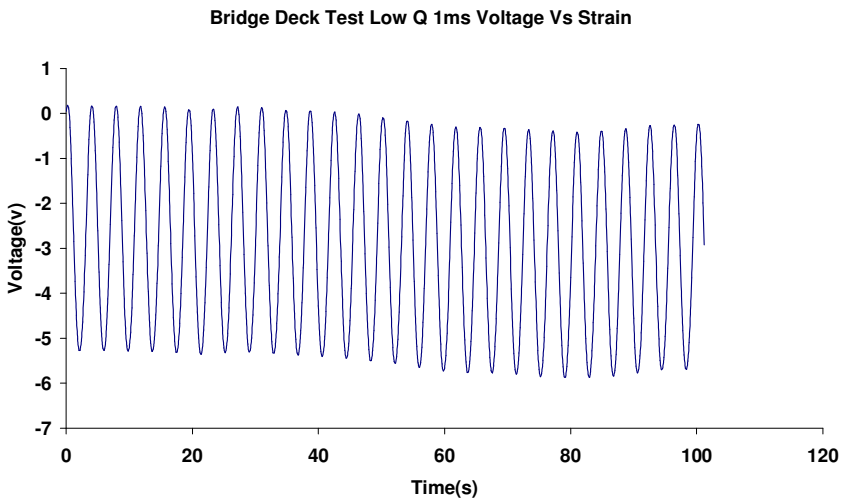

Figure 5.5 Bridge Deck Test Low Q 1ms Voltage vs Time

Figure 5.5 is voltage plot for the low Q condition 1ms time constant case. The voltage and the strain are sinusoidal which is as expected. I notice that the peak values are no longer at the same level. This is because the thermal drift happened during the test. Again, the strain values from our calculation based on the micrometer calibration are not matching those ones obtained from the strain gauge data. This once again tells us the micrometer calibration is not ideal. The 10ms and 100ms time constant cases are very similar to what I showed above.

We performed the voltage and strain measurement over a 100s time period. We also took some measurements for a short period of time (5 second) to monitor just one cycle of signal. Figure 5.6 and 5.7 are voltage plots for just one cycle.

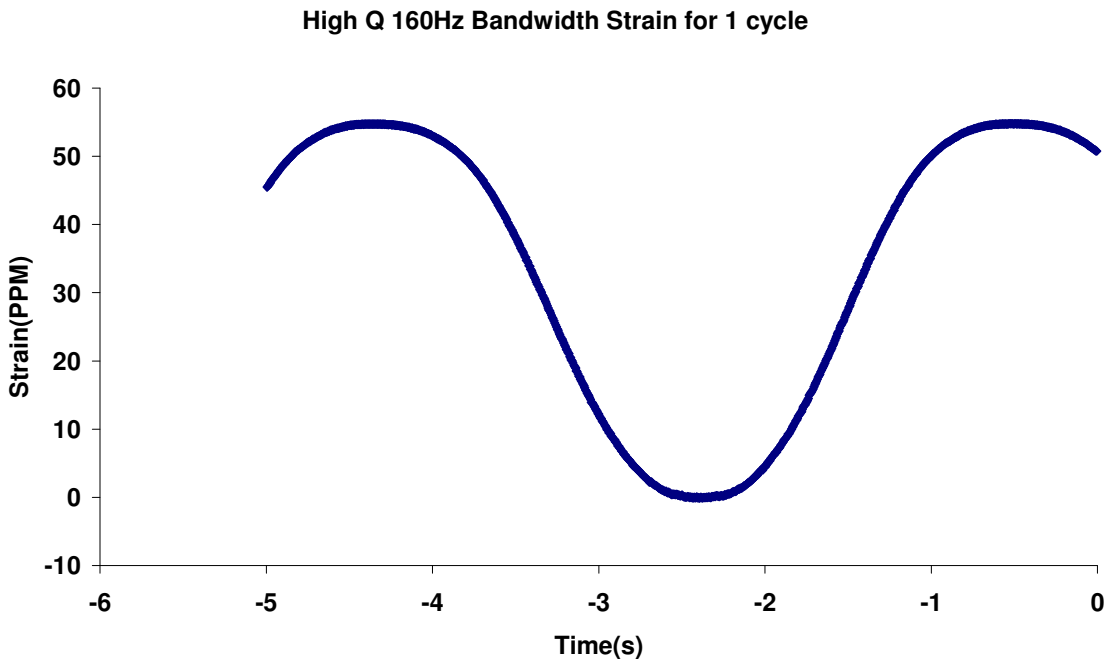

Figure 5.6 Bridge Deck Test High Q 160 Hz Single Cycle Strain vs Time

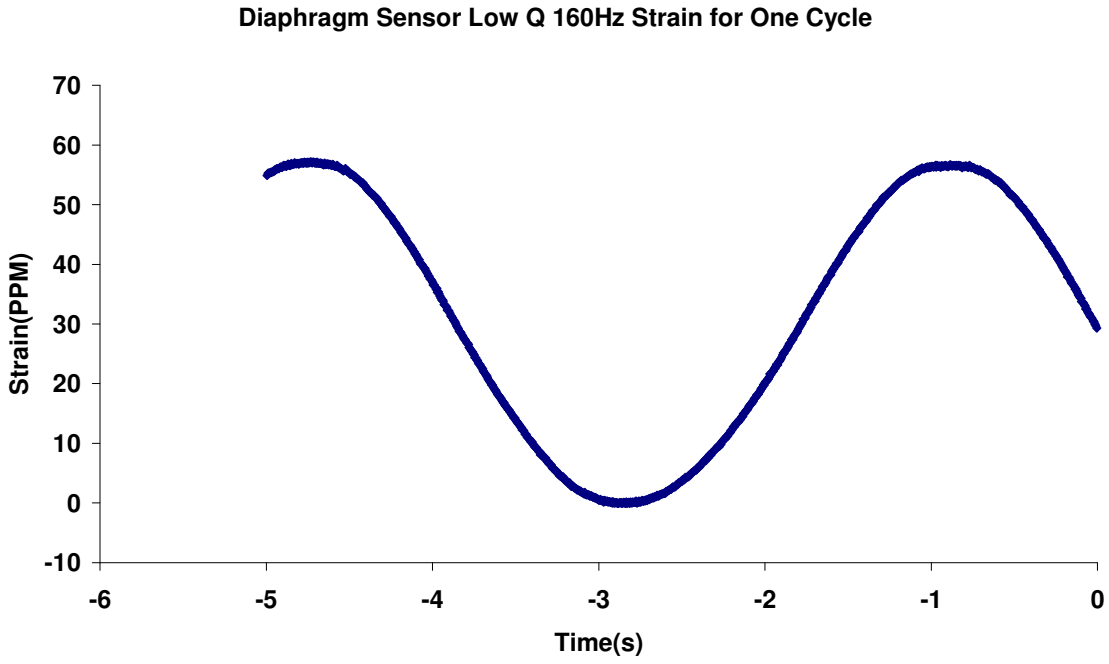

Figure 5.7 Bridge Deck Test Low Q 160Hz Single Cycle Strain vs Time

If I zoom in on figure 5.6 and 5.7 and take a look at the voltage around the peak, I will see the voltage noise very clearly.

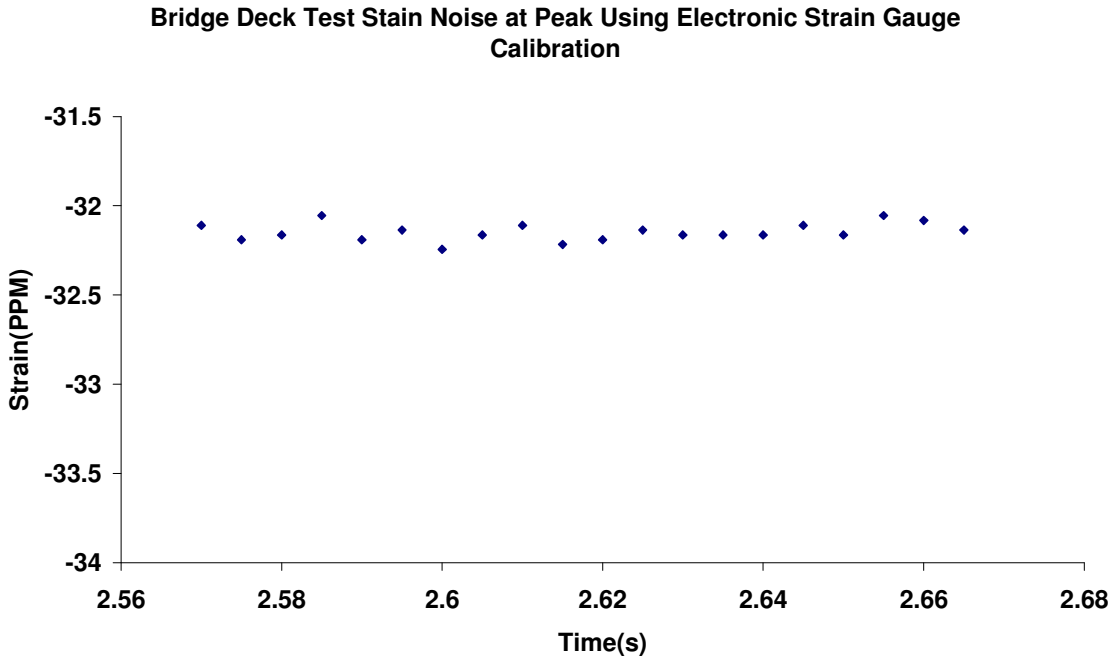

Figure 5.8 Bridge Deck Test Strain Noise at Peak High Q 160 Hz Bandwidth

I obtained 10 samples for each case of the single cycle test. Figure 5.8 shows strain noise at peaks for different samples. I calculated the RMS strain noise of the single cycle test using data similar to what is shown in figure 5.8. The histograms shown in the following figures are the RMS strain noise at the peak for each case of the single cycle test.

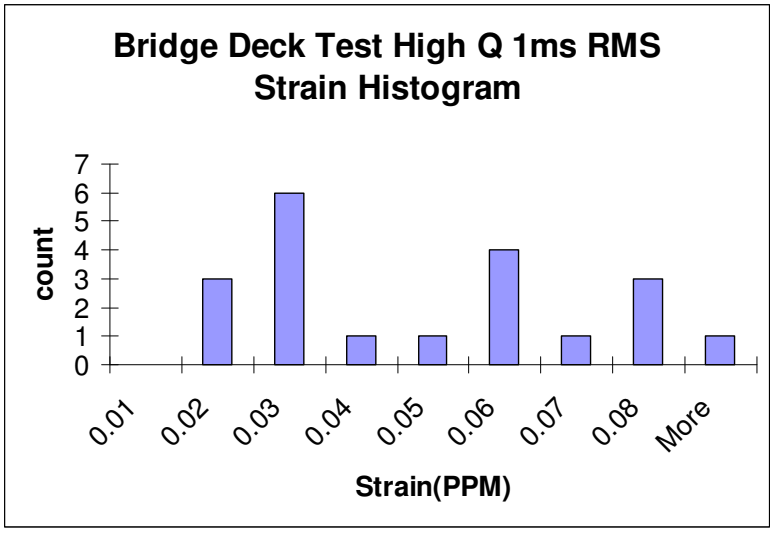

Figure 5.9 Bridge Deck Test High Q 1ms RMS Strain Histogram

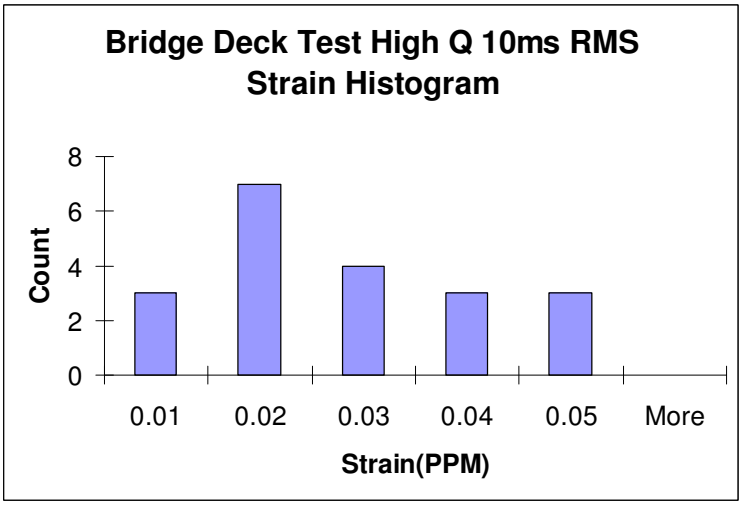

Figure 5.10 Bridge Deck Test High Q 10ms RMS Strain Histogram

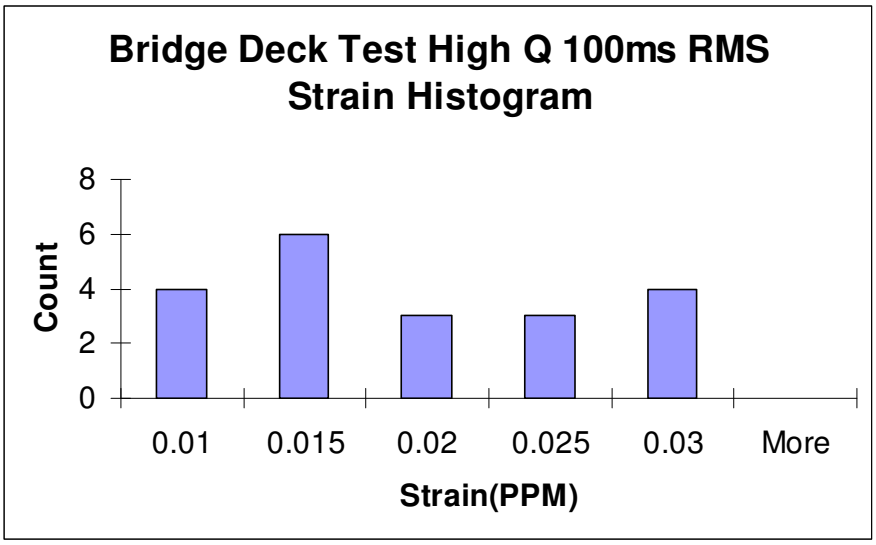

Figure 5.11 Bridge Deck Test High Q 100ms RMS Strain Histogram

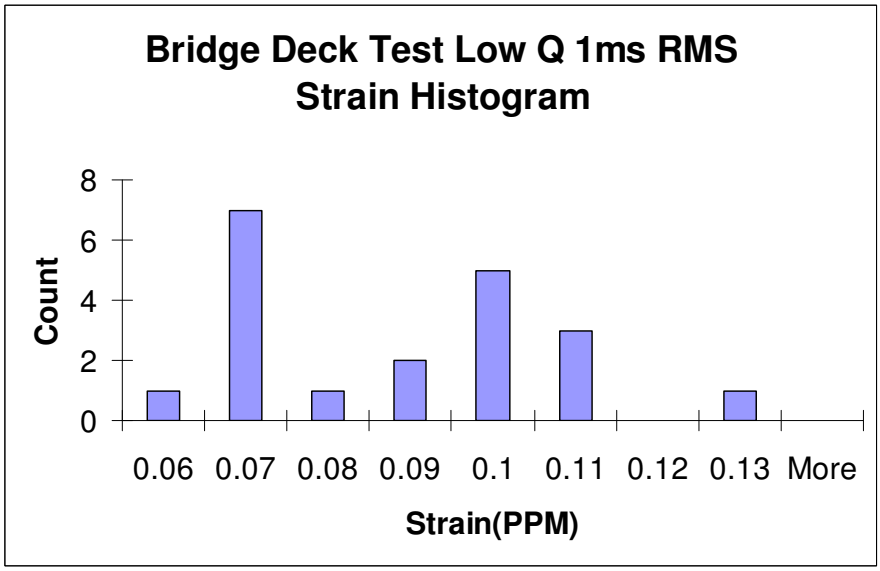

Figure 5.12 Bridge Deck Test Low Q 1ms RMS Strain Histogram

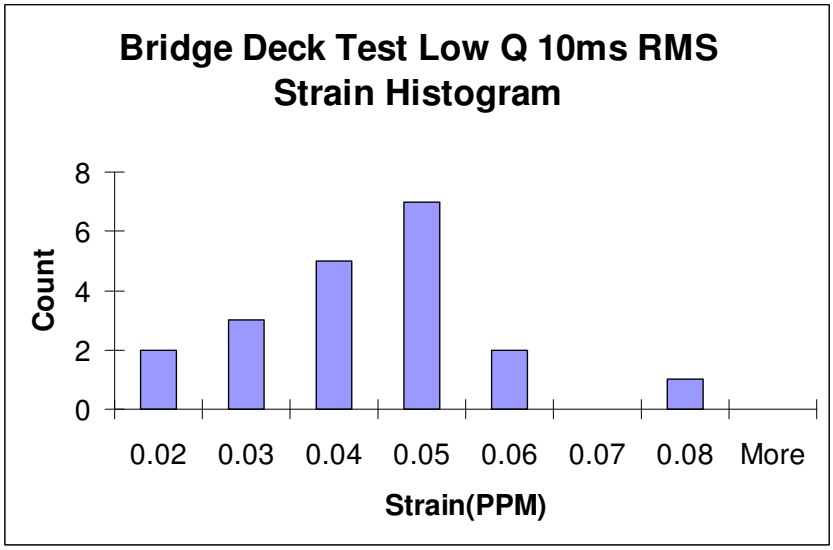

Figure 5.13 Bridge Deck Test Low Q 10ms RMS Strain Histogram

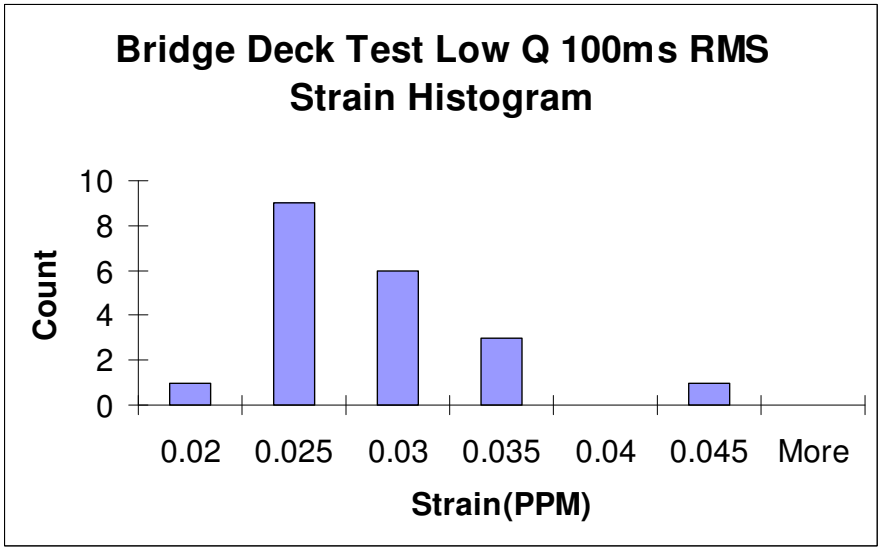

Figure 5.14 Bridge Deck Test Low Q 100ms RMS Strain Histogram

I can use the bridge deck test as the calibration to calculate the strain of the diaphragm sensor noise in the ECE laboratory where the sensor is without any external force on it. Using Matlab programming, I obtained the RMS strain noise

of these measurements of hundreds of nanostrains. In other words, the RMS noise at the peak of the bridge deck test is much smaller than the RMS noise of the ECE laboratory test. The reason for this is that the bridge deck test is only 5 seconds for each cycle while the ECE laboratory test is 100s long which has more thermal drift and acoustic noise.

6. Chapter VI Conclusion

In this thesis, the design of a RF nanostrain resonator for Structural Health Monitoring applications has been presented. The RF sensor as an alternative to the existing strain sensor technologies such as foil strain gauge and fibre optical sensors has advantages of a low cost, easy interrogation system and higher resolution.

The power level of the RF supply, the signal going into the mixer, the signal out the mixer and signal out of the Lock-in amplifier have been measured using a power meter. The measured values are in good agreement with the estimated value. The equations for the strain noise for the system using different sensor cavities have been derived. The strain resolution for the cylinder sensor is calculated to be 1.2 nanostrain for the 160Hz bandwidth case. The calculated strain resolutions for the diaphragm sensor high Q and low Q conditions are 0.11 and 0.9 nanostrain for 160Hz bandwidth respectively.

It has been shown that the amplitude of the mixer output voltage reaches its peak when the output voltage is in phase or 180 out of phase of the RF supply voltage. Also, the mixer output voltage reaches it minimum when the voltage is 90 degree out of phase of the RF supply voltage. I adjust the phase shifter continuously and measure the DC average voltage of the mixer output voltage. The DC average voltage vs phase is sinusoidal which is as expected.

The strain noise of the cylinder sensor was measured in our Electrical and Computer Engineering laboratory using the thermal induced strain calibration

technique. The cylinder sensor strain noises are approximately 25PPB, 11PPB and 8PPB for the 160, 16 and 1.6Hz bandwidth cases respectively.

Calibration for the diaphragm sensor was carried out in a civil structures laboratory using comparison to electronic strain gauge. I use two strain gauges as comparison for our sensor and I can relate the voltage output to the strain obtained by the strain gauges. This calibration method gives much more reliable data than the results I obtained using other type of calibration such as the micrometer calibration technique. The diaphragm sensor noise strains are less than 10 PPB for all the time constant cases for both high Q and low Q conditions.

Dynamic test on a model structure in the civil structures laboratory was carried out. I measured the strain for just one cycle for 10 times for each case. The RMS strain noise for high Q condition 1ms, 10ms and 100ms cases are approximately 44PPB, 22PPB, and 17PPB respectively. The RMS strain noise for low Q condition 1ms, 10ms and 100ms time constant cases are approximately 82PPB, 39PPB and 27PPB respectively.

The RF strain sensor has been designed and tested. It will find its application where high resolution dynamic strain is to be measured such as the strain change on the bridge caused by traffic loading. It might also have use in weight-in-motion. It can reach the strain resolution in nanostrain range which is perfect for SHM applications.

Appendix A: Datasheets

A1: Attenuator Datasheet

Coaxial

Precision Fixed Attenuator

BW-S6W2+

50Ω 2W 6dB DC to 18000 MHz

CASE STYLE: FF658

Connectors	Model	Price	Qty.
SMA Female-SMA Male	BW-S6W2+	29.95 ea.	(1-49)

+ RoHS compliant in accordance with EU Directive (2002/95/EC)

The +Suffix has been added in order to identify RoHS Compliance. See our web site for RoHS Compliance methodologies and qualifications.

Maximum Ratings

Operating Temperature	-55°C to 100°C
Storage Temperature	-55°C to 100°C**

**With mated connectors. Unmated, 85°C max.

Permanent damage may occur if any of these limits are exceeded.

Features

- DC to 18000 MHz
- precise attenuation
- excellent VSWR, 1.20 typ.
- stainless steel SMA male and female connectors

Applications

- matching
- instrumentation
- test set-ups

Outline Drawing

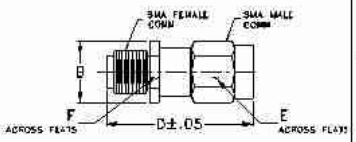

Outline Dimensions (inch / mm)

B	D	E	F	wt
.36	.85	.312	.312	grams
9.14	21.59	7.92	7.92	4.3

Electrical Specifications

FREQ. RANGE (MHz)	ATTENUATION[1] (dB)		VSWR[2] (:1)			MAX. INPUT POWER[3] (W)
			DC-4 GHz	4-8 GHz	8-12.4 GHz	
f -f	Nom.	ACCURACY	Max.	Max.	Max.	
DC-18000	6	±0.40	1.20	1.25	1.30	2

1. At 25°C, accuracy includes frequency and power variations. Temperature coefficient of attenuation: .0004dB/dB/°C typ.
2. VSWR from 12.4 to 18 GHz, 1.40 typ.
3. Average power at 25°C ambient, derate linearly to 0.5W at 100°C. Peak Power 125W max. Specified pulse width, 100 Hz PRF

Typical Performance Data

Frequency (MHz)	Attenuation (dB)	VSWR (:1)
1.00	5.73	1.02
100.00	5.75	1.03
1000.00	5.82	1.04
1999.90	5.86	1.05
5000.00	5.94	1.07
7999.90	5.99	1.08
9999.90	6.01	1.14
12400.10	6.03	1.20
15000.00	6.06	1.17
18000.00	6.16	1.39

Electrical Schematic

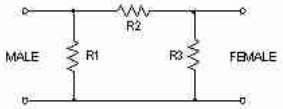

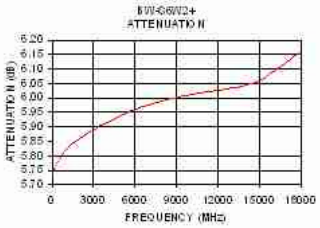

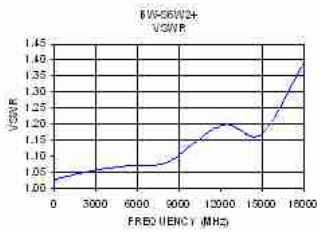

Mini-Circuits®
ISO 9001 ISO 14001 AS9100 CERTIFIED

For detailed performance specs & shopping online see web site

P.O. Box 350166, Brooklyn, New York 11235-0003 (718) 934-4500 Fax (718) 332-4661 The Design Engineers Search Engine Provides ACTUAL Data Instantly at minicircuits.com

RF/IF MICROWAVE COMPONENTS

Notes: 1. Performance and quality attributes and conditions not expressly stated in this specification sheet are intended to be excluded and do not form a part of this specification sheet. 2. Electrical specifications and performance data contained herein are based on Mini-Circuits applicable established test performance criteria and measurement instructions. 3. The parts covered by this specification sheet are subject to Mini-Circuits standard limited warranty and terms and conditions (collectively, "Standard Terms"); Purchasers of this part are entitled to the rights and benefits contained therein. For a full statement of the Standard Terms and the exclusive rights and remedies thereunder, please visit Mini-Circuits' website at www.minicircuits.com/MCLStore/terms.jsp

REV. D
M96896
EB-7120
BW-S6W2
070329
Page 1 of 1

A2: Mixer Datasheet

Mini-Circuits

ZX05

NEW!

electrical specifications at 25°C

MODEL NO.	LO LEVEL (dBm)	RF @1dB Comp. Typ. (dBm)	FREQUENCY MHz LO/RF f_L-f_U	IF	CONVERSION LOSS dB $\bar{x}$	σ	Max.	Total Range Max.	LO-RF ISOLATION dB L Typ.	L Min.	M Typ.	M Min.	U Typ.	U Min.	LO-IF ISOLATION dB L Typ.	L Min.	M Typ.	M Min.	U Typ.	U Min.	IP3@ center band Typ. (dBm)	E factor	CASE STYLE	CONNECTION	PRICE $ Qty. (10-49)
ZX05-1LHW	+10	+5	2-750	DC-750	5.3	0.1	6.8	8.5	66	50	52	35	46	27	64	40	50	27	40	20	15	0.5	FL905	ad	38.95
• ZX05-C24LH	+10	+5	300-2400	DC-700	6.5	0.1	8.9	—			40 (typ.)		25 (min.)				30 (typ.)		15 (min.)		13	0.3	FL905	ad	38.95
ZX05-C42LH	+10	+5	1000-4200	DC-1500	6.0	0.1	8.9	—			38 (typ.)		23 (min.)				20 (typ.)		11 (min.)		12	0.2	FL905	ad	38.95
• ZX05-C60LH	+10	+5	1600-4400	DC-2000	6.3	0.1	7.9	—			35 (typ.)		23 (min.)				17 (typ.)		—		13	0.3	FL905	ad	38.95
			4400-6000	DC-2000	6.0	0.1	8.3	—			27 (typ.)		20 (min.)				21 (typ.)		—		11	0.1	FL905	ad	38.95
†• ZX05-1MHW	+13	+9	0.5-600	DC-600	5.2	0.1	6.9	8.0	63	50	53	32	43	20	56	40	44	25	30	20	17	0.4	FL905	ad	39.95
ZX05-12MH	+13	+9	10-1200	DC-1200	6.3	0.1	8.0	9.3	62	45	45	32	40	26	68	40	42	27	30	20	22	0.9	FL905	ad	39.95
• ZX05-C24MH	+13	+9	300-2400	DC-700	6.1	0.1	8.6	—			40 (typ.)		20 (min.)				25 (typ.)		14 (min.)		13	0	FL905	ad	39.95
ZX05-25MH	+13	+9	5-2500	5-1500	6.9	0.1	8.8	9.8	47	28	34	23	34	23	34	23	32	18	23	17	18	0.5	FL905	ad	39.95
ZX05-42MH	+13	+9	5-4200	5-3500	7.5	0.2	9.8	11.8	47	28	29	20	30	15	34	23	26	17	23	17	19	0.6	FL905	ad	39.95
ZX05-C42MH	+13	+9	1000-4200	DC-1500	6.2	0.1	8.9	—			35 (typ.)		15 (min.)				20 (typ.)		10 (min.)		16	0.3	FL905	ad	39.95
• ZX05-C60MH	+13	+9	1600-4400	DC-2000	6.9	0.1	8.5	—			32 (typ.)		25 (min.)				17 (typ.)		—		15	0.2	FL905	ad	39.95
			4400-6000	DC-2000	6.0	0.1	8.5	—			22 (typ.)		18 (min.)				15 (typ.)		—		15	0.2	FL905	ad	39.95
ZX05-1HW	+17	+14	5-750	DC-750	6.0	0.1	8.6	9.0	64	45	48	35	42	28	50	35	40	30	30	20	26	0.9	FL905	ad	41.95
†• ZX05-10H	+17	+14	10-1000	DC-800	7.0	0.1	8.5	9.5	68	52	55	38	47	25	46	30	32	20	26	13	22	0.5	FL905	ad	41.95
ZX05-17H	+17	+14	100-1700	50-1500	7.2	0.1	8.5	9.5	32	20	—	—	36	22	32	20	—	—	37	22	25	0.8	FL905	ad	41.95
ZX05-20H	+17	+14	1500-2000	DC-300	5.2	0.2	7.8	—			31 (typ.)		22 (min.)				34 (typ.)		20 (min.)		22	0.5	FL905	ad	41.95

E= [IP3(dBm)-LO Power(dBm)]/10

L = low range [f_L to 10 f_L] M = mid range [10 f_L to f_U/2] U = upper range [f_U/2 to f_U]

m = mid band [2f_L to f_U/2]

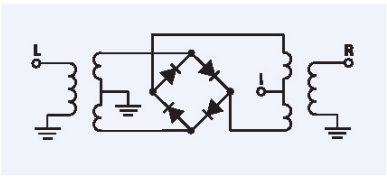

coaxial connections

see case style outline drawing for pin locations

PORT	ad
LO	1
RF	2
IF	3

030430

A2: Mixer Datasheet Continued

FREQUENCY MIXERS

SMA Coaxial

RUGGED, BROAD BAND 0.5 to 6000 MHz

ZX05

NEW!

electrical specifications at 25°C

MODEL NO.	LO LEVEL (dBm)	RF @1dB Comp. Typ. (dBm)	FREQUENCY MHz LO/RF f_L-f_U	FREQUENCY MHz IF	CONVERSION LOSS dB $\bar{x}$	CONVERSION LOSS dB σ	CONVERSION LOSS dB Max.	CONVERSION LOSS dB Total Range Max.	LO-RF ISOLATION dB L Typ.	LO-RF ISOLATION dB L Min.	LO-RF ISOLATION dB M Typ.	LO-RF ISOLATION dB M Min.	LO-RF ISOLATION dB U Typ.	LO-RF ISOLATION dB U Min.	LO-IF ISOLATION dB L Typ.	LO-IF ISOLATION dB L Min.	LO-IF ISOLATION dB M Typ.	LO-IF ISOLATION dB M Min.	LO-IF ISOLATION dB U Typ.	LO-IF ISOLATION dB U Min.	IP3@ center band Typ. (dBm)	E factor	CASE STYLE	CONNECTION	PRICE $ Qty. (10-49)
ZX05-1L	+3	0	2-500	DC-500	5.2	0.1	7.2	8.0	68	50	55	30	44	30	55	40	45	30	35	25	16	1.3	FL905	ad	37.95
†• ZX05-10L	+4	+1	10-1000	DC-800	7.2	0.1	8.2	8.8	70	55	60	40	47	37	40	26	37	20	24	13	16	1.2	FL905	ad	37.95
ZX05-1	+7	+1	0.5-500	DC-500	5.0	0.1	6.5	7.8	70	50	55	35	45	30	65	45	40	25	30	20	15	0.8	FL905	ad	37.95
†• ZX05-2	+7	+1	5-1000	DC-1000	6.67	0.26	8.0	9.5	65	50	47	25	35	22	62	35	45	25	32	20	20	1.3	FL905	ad	37.95
ZX05-10	+7	+1	10-1000	DC-800	6.8	0.1	7.8	8.3	80	50	60	40	47	37	40	26	33	20	24	13	16	0.9	FL905	ad	37.95
†• ZX05-5	+7	+1	5-1500	DC-1000	6.6	0.1	7.5	9.3	50	40	40	25	33	23	50	40	30	20	20	10	15	0.8	FL905	ad	37.95
ZX05-11X	+7	+1	10-2000	5-1000	7.1	0.1	8.2	9.8	62	45	36	20	27	18	60	45	37	20	38	20	9	0.2	FL905	ad	37.95
• ZX05-C24	+7	+1	300-2400	DC-700	6.1	0.1	8.9	—	40 (typ.)		25 (min.)				25 (typ.)		15 (min.)				10	0.3	FL905	ad	37.95
ZX05-30W	+7	+1	300-4000	DC-950	6.8	0.2	9.0	9.8	35 (typ.)		17 (min.)				16 (typ.)		7 (min.)				12	0.5	FL905	ad	37.95
ZX05-C42	+7	+1	1000-4200	DC-1500	6.1	0.1	8.9	—	35 (typ.)		23 (min.)				20 (typ.)		12 (min.)				10	0.3	FL905	ad	37.95
• ZX05-C60	+7	+1	1600-4400	DC-2000	6.3	0.2	8.3	—	32 (typ.)		20 (min.)				17 (typ.)		—				9	0.2	FL905	ad	37.95
			4400-6000	DC-2000	6.2	0.3	8.5	—	23 (typ.)		17 (min.)				18 (typ.)		—				8	0.1	FL905	ad	37.95

E= [IP3(dBm)-LO Power(dBm)]/10

L = low range [f_L to 10 f_L] M = mid range [10 f_L to f_U/2] U = upper range [f_U/2 to f_U]

m = mid band [2f_L to f_U/2]

features

- rugged construction
- small size
- low conversion loss
- high L-R isolation
- multiple patents pending

applications

- cellular
- PCS
- instrumentation
- satellite communication

NOTES:

$\bar{x}$ Average of conversion loss at center of mid-band frequency (f_L+f_U/4)
σ Standard deviation
† Models noted have positive phase detection. Phase detection negative for all other models.
• Conversion loss specification at 30 MHz IF. For performance vs. IF see our website.
A. General Quality Control Procedures, Environmental Specifications, HI-Rel and MIL description are given in section 0, see "Mini-Circuits Guarantees Quality" article.
B. Connector types and case mounted options, case finishes are given in section 0, see "Case Styles & Outline Drawings".
C. Prices and Specifications subject to change without notice.
1. Absolute maximum power, voltage and current ratings:
1a. RF power, 50 mW, 200 mW (for LO+13, +17)
1b. Peak IF current, 40 mA
2. Operating Temperature, -40°C to 85°C

030425

Mini-Circuits®
INTERNET http://www.minicircuits.com
P.O. Box 350166, Brooklyn, New York 11235-0003 (718) 934-4500 Fax (718) 332-4661
Distribution Centers NORTH AMERICA 800-654-7949 • 417-335-5935 • Fax 417-335-5945 • EUROPE 44-1252-832600 • Fax 44-1252-837010
ISO 9001 CERTIFIED

Apendix B: MATLAB Codes

B1: Code for RMS Noise Calculation

```
close all; clear all; clc;

n = [0.0368648
0.0468528
......
......
0.0029056
-0.0049032];

RMS = zeros(20,1);
sum = 0;
for i = 1:500
   sum = sum + (n(i)-mean(n))^2;
end
%RMS = sqrt(sum/500);
sqrt(sum/500)
% mean(n)
%1-5 sec
sum = 0;
sum_a = 0;
for i = 1:25
   sum_a = sum_a + n(i);
end
avg = sum_a / 25;
for i = 1:25
   sum = sum + (n(i)-avg)^2;
end

RMS(1,1) = sqrt(sum/25);

%6-10 sec
sum = 0;
sum_a = 0;
for i = 26:50
   sum_a = sum_a + n(i);
end
avg = sum_a / 25;
for i = 26:50
   sum = sum + (n(i)-avg)^2;
end
```

```
RMS(2,1) = sqrt(sum/25);

%11- 15sec
sum = 0;
sum_a = 0;
for i = 51:75
   sum_a = sum_a + n(i);
end
avg = sum_a / 25;
for i = 51:75
   sum = sum + (n(i)-avg)^2;
end

RMS(3,1) = sqrt(sum/25);

%16-20 sec
sum = 0;
sum_a = 0;
for i = 76:100
   sum_a = sum_a + n(i);
end
avg = sum_a / 25;
for i = 76:100
   sum = sum + (n(i)-avg)^2;
end

RMS(4,1) = sqrt(sum/25);
%21-25 sec
sum = 0;
sum_a = 0;
for i = 101:125
   sum_a = sum_a + n(i);
end
avg = sum_a / 25;
for i = 101:125
   sum = sum + (n(i)-avg)^2;
end

RMS(5,1) = sqrt(sum/25);
%26-30 sec
sum = 0;
sum_a = 0;
for i = 126:150
   sum_a = sum_a + n(i);
end
```

```
avg = sum_a / 25;
for i = 126:150
   sum = sum + (n(i)-avg)^2;
end

RMS(6,1) = sqrt(sum/25);
%31-35 sec
sum = 0;
sum_a = 0;
for i = 151:175
   sum_a = sum_a + n(i);
end
avg = sum_a / 25;
for i = 151:175
   sum = sum + (n(i)-avg)^2;
end

RMS(7,1) = sqrt(sum/25);
%36-40 sec
sum = 0;
sum_a = 0;
for i = 176:200
   sum_a = sum_a + n(i);
end
avg = sum_a / 25;
for i = 176:200
   sum = sum + (n(i)-avg)^2;
end

RMS(8,1) = sqrt(sum/25);
%41-45 sec
sum = 0;
sum_a = 0;
for i = 201:225
   sum_a = sum_a + n(i);
end
avg = sum_a / 25;
for i = 201:225
   sum = sum + (n(i)-avg)^2;
end

RMS(9,1) = sqrt(sum/25);
%46-50 sec
sum = 0;
sum_a = 0;
for i = 226:250
```

```
   sum_a = sum_a + n(i);
end
avg = sum_a / 25;
for i = 226:250
   sum = sum + (n(i)-avg)^2;
end

RMS(10,1) = sqrt(sum/25);

%51-55 sec
sum = 0;
sum_a = 0;
for i = 251:275
   sum_a = sum_a + n(i);
end
avg = sum_a / 25;
for i = 251:275
   sum = sum + (n(i)-avg)^2;
end

RMS(11,1) = sqrt(sum/25);

%56-60 sec
sum = 0;
sum_a = 0;
for i = 276:300
   sum_a = sum_a + n(i);
end
avg = sum_a / 25;
for i = 276:300
   sum = sum + (n(i)-avg)^2;
end

RMS(12,1) = sqrt(sum/25);

%61- 65sec
sum = 0;
sum_a = 0;
for i = 301:325
   sum_a = sum_a + n(i);
end
avg = sum_a / 25;
for i = 301:325
   sum = sum + (n(i)-avg)^2;
end
```

```
RMS(13,1) = sqrt(sum/25);

%66-70 sec
sum = 0;
sum_a = 0;
for i = 326:350
   sum_a = sum_a + n(i);
end
avg = sum_a / 25;
for i = 326:350
   sum = sum + (n(i)-avg)^2;
end

RMS(14,1) = sqrt(sum/25);
%71-75 sec
sum = 0;
sum_a = 0;
for i = 351:375
   sum_a = sum_a + n(i);
end
avg = sum_a / 25;
for i = 351:375
   sum = sum + (n(i)-avg)^2;
end

RMS(15,1) = sqrt(sum/25);
%76-80 sec
sum = 0;
sum_a = 0;
for i = 376:400
   sum_a = sum_a + n(i);
end
avg = sum_a / 25;
for i = 376:400
   sum = sum + (n(i)-avg)^2;
end

RMS(16,1) = sqrt(sum/25);
%81-85 sec
sum = 0;
sum_a = 0;
for i = 401:425
   sum_a = sum_a + n(i);
end
avg = sum_a / 25;
for i = 401:425
```

```
   sum = sum + (n(i)-avg)^2;
end

RMS(17,1) = sqrt(sum/25);
%86-90 sec
sum = 0;
sum_a = 0;
for i = 426:450
   sum_a = sum_a + n(i);
end
avg = sum_a / 25;
for i = 426:450
   sum = sum + (n(i)-avg)^2;
end

RMS(18,1) = sqrt(sum/25);
%91-95 sec
sum = 0;
sum_a = 0;
for i = 451:475
   sum_a = sum_a + n(i);
end
avg = sum_a / 25;
for i = 451:475
   sum = sum + (n(i)-avg)^2;
end

RMS(19,1) = sqrt(sum/25);
%96-100 sec
sum = 0;
sum_a = 0;
for i = 476:500
   sum_a = sum_a + n(i);
end
avg = sum_a / 25;
for i = 476:500
   sum = sum + (n(i)-avg)^2;
end

RMS(20,1) = sqrt(sum/25);
```

B2: Code for Diaphragm Sensor Structure Lab test Linear fit

```
close all; clear all; clc;

ESG_a_1 = [5.435923
......
4.57222];

ESG_a_2 = [5.541199
6.167399
......
-7.22];


plot(ESG_a_1, V_a)
hold on
plot(ESG_a_2, V_a)
title('High Q 1ms Time constant Voltage vs Strain Linear Fitting')
xlabel('Strain(microstrain)')
ylabel('Voltage(volt)')

ESG_b_1 = [-1.981156
-1.678858
......
-1.031077];

ESG_b_2 = [-0.052901
......
-0.463141];

V_b = [-6.42
......
-6.72];

figure
plot(ESG_b_1, V_b)
hold on
plot(ESG_b_2, V_b)
title('High Q 10ms Time constant Voltage vs Strain Linear Fitting')
xlabel('Strain(microstrain)')
ylabel('Voltage(volt)')
```

References:

[1] Charles R. Farrar et al. An introduction to structural health monitoring. *Phil. Trans. R. Soc*. A (2007) 365, 303–315 Published online 12 December 2006

[2] Richard M. Whit., A sensor classification scheme. *IEEE transaction on Ultrasonic, Ferroelectrics and Frequency Control*, VOL uppc-34, No. 2, March 1987

[3] Aftab Mufti. *Guidelines for Structure Health Monitoring design manual No.2*, Winnipeg, MB, ISIS Canada Corporation, September 2001, pp.A1-A20

[4] Automatic Control Lab of Mechanical Engineering Department of DEU. "The Strain Gauge". Internet: http://web.deu.edu.tr/mechatronics/TUR/strain_gauge.htm, July 23, 2009

[5] Campbell Scientific Inc. "AVW 200 a new vibrating-wire interface". Internet: http://www.campbellsci.com/vibrating-wire, July 24, 2009

[6] Byoungho Lee. Review of present status of fiber optical sensors. *Optical fiber technology 9*, (2003) 57-79

[7] M. Majumder et al. Fiber Bragg gratings in structural health monitoring – presents status and applications. *Sensors and Actuators A* 147 (2008) 150 – 164

[8] B. Lee, Y. Jeong. Interrogation techniques for fiber grating sensors and the theory of fiber gratings. *F.T.S. Yu, S. Yin (Eds.), Fiber Optic Sensors.* Dekker, New York, 2002, Chap. 7, pp. 295–381

[9] Minho Song et al. Fiber bragg grating strain sensor demodulation with quadrature sampling of a Mach-Zehnder interferometer. *APPLIED OPTICS* Vol. 39, No. 7, 1 March 2000

[10] D. Gatti et al. Fiber strain sensor based on a p-phase-shifted Bragg grating and the Pound-Drever-Hall technique. *OPTICS EXPRESS 1945*. Vol. 16, No. 3, 4 February 2008

[11] Jong H Chow et al. Phase-Sensitive Interrogation of Fiber Bragg Grating Resonators for Sensing Applications. *JOURNAL OF LIGHTWAVE TECHNOLOGY*, VOL. 23, NO. 5, MAY 2005

[12] A. D. Kersey et al. Fiber grating sensors, *J. Lightw. Technol*., vol. 15, no. 8, pp. 1442–1463, Aug. 1997.

[13] K. Lau et al. Strain monitoring in FRP laminates and concrete beams using FBG sensors. *Comp. Struct*. 51 (2001) 9–20

[14] Impil Kang et al. A carbon nanotube strain sensor for structural health monitoring. *SMART MATERIALS AND STRUCTURES*. 15 (2006) 737–748

[15] Jun Zhou et al. Flexible Piezotronic Strain Sensor. *Nano Letters*, 2008 VOL. 8, NO. 9, pp 3025-3040

[16] B.B. Carter et al, Measurement of displacement and strain by capacitance methods. *Proc. Inst. Mech. Eng.* 5 (1945) 215–221

[17] I. W. Hornby, The Vibrating Wire Strain Gauge, *Strain Gauge Technology*, Elsevier, 1982, pp. 325–340 reprint 1989

[18] Jayant Sirohi and Inderjit Chopra, Fundamental Understanding of Piezoelectric Strain Sensors, *Journal of Intelligent Material Systems and Structures* 2000; 11; 246

[19] David. M. Pozar, mixers, *Microwave and RF Wireless System*, John Wiley & Sons, Inc, 2001, pp. 226

[20] Stanford Research System, “SR510 and SR530 Analog Lock-in Amplifiers Datasheet”.

Internet: http://www.thinksrs.com/downloads/PDFs/Catalog/SR510530c.pdf

[21] D.J. Thomson, D. Card and G.E. Bridges, RF cavity passive wireless sensors with time domain gating based interrogation for SHM of civil structures

[22] Wikipedia, “Coefficient of thermal expansion”.

Internet: http://en.wikipedia.org/wiki/Coefficient_of_thermal_expansion